https://doi.org/10.3847/1538-4357/ab14e6

Do *Kepler* Superflare Stars Really Include Slowly Rotating Sun-like Stars?—Results Using APO 3.5 m Telescope Spectroscopic Observations and *Gaia*-DR2 Data

Yuta Notsu[1,2,3,10,11] , Hiroyuki Maehara[4,5] , Satoshi Honda[6], Suzanne L. Hawley[7] , James R. A. Davenport[7] ,
Kosuke Namekata[3,12] , Shota Notsu[3,8,10,11] , Kai Ikuta[3], Daisaku Nogami[3], and Kazunari Shibata[9]

[1] Laboratory for Atmospheric and Space Physics, University of Colorado Boulder, 3665 Discovery Drive, Boulder, CO 80303, USA; ynotsu@kwasan.kyoto-u.ac.jp
[2] National Solar Observatory, 3665 Discovery Drive, Boulder, CO 80303, USA
[3] Department of Astronomy, Kyoto University, Sakyo, Kyoto 606-8502, Japan
[4] Okayama Branch Office, Subaru Telescope, National Astronomical Observatory of Japan, NINS, Kamogata, Asakuchi, Okayama 719-0232, Japan
[5] Okayama Observatory, Kyoto University, Kamogata, Asakuchi, Okayama 719-0232, Japan
[6] Nishi-Harima Astronomical Observatory, Center for Astronomy, University of Hyogo, Sayo, Hyogo 679-5313, Japan
[7] Department of Astronomy, University of Washington, Seattle, WA 98195, USA
[8] Leiden Observatory, Leiden University, P.O. Box 9513, 2300 RA Leiden, The Netherlands
[9] Astronomical Observatory, Kyoto University, Sakyo, Kyoto 606-8502, Japan

Abstract

We report the latest view of *Kepler* solar-type (G-type main-sequence) superflare stars, including recent updates with Apache Point Observatory (APO) 3.5 m telescope spectroscopic observations and *Gaia*-DR2 data. First, we newly conducted APO 3.5 m spectroscopic observations of 18 superflare stars found from *Kepler* 1-minute time-cadence data. More than half (43 stars) are confirmed to be "single" stars, among 64 superflare stars in total that have been spectroscopically investigated so far in this APO 3.5 m and our previous Subaru/HDS observations. The measurements of $v \sin i$ (projected rotational velocity) and chromospheric lines (Ca II H and K and Ca II $\lambda 8542$) support that the brightness variation of superflare stars is caused by the rotation of a star with large starspots. We then investigated the statistical properties of *Kepler* solar-type superflare stars by incorporating *Gaia*-DR2 stellar radius estimates. As a result, the maximum superflare energy continuously decreases as the rotation period $P_{\rm rot}$ increases. Superflares with energies $\lesssim 5 \times 10^{34}$ erg occur on old, slowly rotating Sun-like stars ($P_{\rm rot} \sim 25$ days) approximately once every 2000–3000 yr, while young, rapidly rotating stars with $P_{\rm rot} \sim$ a few days have superflares up to 10^{36} erg. The maximum starspot area does not depend on the rotation period when the star is young, but as the rotation slows down, it starts to steeply decrease at $P_{\rm rot} \gtrsim 12$ days for Sun-like stars. These two decreasing trends are consistent since the magnetic energy stored around starspots explains the flare energy, but other factors like spot magnetic structure should also be considered.

Key words: stars: abundances – stars: activity – stars: flare – starspots – stars: rotation – stars: solar-type

1. Introduction

Flares are energetic explosions in the stellar atmosphere and are thought to occur by intense releases of magnetic energy stored around starspots (e.g., Shibata & Magara 2011). Not only the Sun but also many stars are known to show stellar magnetic activity, including flares. In particular, young, rapidly rotating stars, close binary stars, and dMe stars tend to show high magnetic activity levels, and magnetic fields of a few kG are considered to be distributed in large regions on the stellar surface (e.g., Gershberg 2005; Reid & Hawley 2005; Benz & Güdel 2010; Kowalski et al. 2010; Osten et al. 2016). They frequently have "superflares," which have a total bolometric energy 10–10^6 times more energetic ($\sim 10^{33}$–10^{38} erg; Schaefer et al. 2000) than the largest solar flares ($\sim 10^{32}$ erg; Emslie et al. 2012). In contrast, the Sun rotates slowly ($P_{\rm rot} \sim 25$ days), and the mean magnetic field is weak (a few gauss). Thus, it has been thought that slowly rotating Sun-like stars basically do not have high magnetic activity events like superflares.

Recently, however, many superflares on solar-type (G-type main-sequence) stars have been reported (Maehara et al. 2012, 2015; Shibayama et al. 2013; Candelaresi et al. 2014; Balona 2015; Wu et al. 2015; Davenport 2016; Van Doorsselaere et al. 2017) by using the high-precision photometric data of the *Kepler* space telescope (Koch et al. 2010).[13,14] The analyses of *Kepler* data enabled us to discuss statistical properties of superflares since a large number of flare events were discovered. The frequency–energy distribution of superflares on solar-type stars shows a power-law distribution $dN/dE \approx E^{\alpha}$ with the index $\alpha = (-1.5) - (-1.9)$, and this distribution is consistent with that of solar flares (Maehara et al. 2012, 2015; Shibayama et al. 2013). Many superflare stars show quasi-periodic brightness variations with a typical period of from 1 day to a few tens of days and a typical amplitude of 0.1%–10%. They are assumed to be explained by the rotation of the star with fairly large starspots (Notsu et al. 2013b), and the starspot size $A_{\rm spot}$ and rotation period $P_{\rm rot}$ values can be estimated from these brightness variations.

Using these $A_{\rm spot}$ values, we confirmed that the superflare energy is related to the total coverage of the starspots and that the superflare energy can be explained by the magnetic energy

---

[13] We note here for reference that superflares on solar-type stars have been recently reported not only with *Kepler* but also with X-ray space telescope observations (e.g., Pye et al. 2015) and ground-based photometric observations (e.g., Jackman et al. 2018), though currently the number of observed events are much smaller than the *Kepler* results.

[14] We also note here that now there are many flare studies using *Kepler* (and *K2*) data not only for solar-type stars discussed in this study but also for the other spectral-type stars, such as K and M dwarfs (e.g., Walkowicz et al. 2011; Candelaresi et al. 2014; Hawley et al. 2014; Ramsay & Doyle 2015; Davenport 2016; Van Doorsselaere et al. 2017; Yang et al. 2017; Chang et al. 2018) and brown dwarfs (e.g., Gizis et al. 2013; Paudel et al. 2018).

stored around these large starspots (Notsu et al. 2013b; Shibata et al. 2013). We then found that energetic superflares with energy up to 10^{35} erg could occur on stars rotating as slowly as the Sun ($P_{rot} \sim 25$ days), even though the frequency is low (once in a few thousand years), compared with rapidly rotating stars (Notsu et al. 2013b). We also investigated statistical properties of starspots in relation to superflare studies and suggested that superflare events are well characterized by the existence of large starspots and the occurrence frequency of large starspots is also consistent with that of sunspots (Maehara et al. 2017). In addition, we suggested that the Sun can generate a large magnetic flux that is sufficient for causing superflares on the basis of theoretical estimates (Shibata et al. 2013). It is becoming important to find out the maximum size of starspots and superflares that can be generated on Sun-like stars, not only in solar and stellar physics (e.g., Aulanier et al. 2013; Shibata et al. 2013; Toriumi et al. 2017; Katsova et al. 2018; Schmieder 2018) but also in solar-terrestrial physics and even exoplanet studies, for example, extreme space weather events and their effects on our society (Royal Academy of Engineering 2013; Tsurutani & Lakhina 2014; Hudson 2015; Schrijver 2015; Takahashi et al. 2016; Eastwood et al. 2017; Riley et al. 2018), a history of solar activity over $\sim$1000 yr (e.g., Miyake et al. 2012, 2013; Hayakawa et al. 2017a, 2017b; Usoskin 2017), and the potential habitability of various planets (e.g., Segura et al. 2010; Airapetian et al. 2016; Atri 2017; Lingam & Loeb 2017).

The results of *Kepler* described here are now also supported by spectroscopic studies. We have observed 50 solar-type superflare stars using Subaru/HDS (Notsu et al. 2013a, 2015a, 2015b; Nogami et al. 2014; Honda et al. 2015). We found that more than half (34 stars) of the 50 targets have no obvious evidence of being in a binary system, and the stellar atmospheric parameters (temperature, surface gravity, and metallicity) of these stars are in the range of those for ordinary solar-type stars (Notsu et al. 2015a). More importantly, Notsu et al. (2015b) supported the above interpretation that the quasi-periodic brightness variations of superflare stars are explained by the rotation of a star with large starspots, by measuring $v \sin i$ (projected rotational velocity) and the intensity of the Ca II λ8542 line. The existence of large starspots on superflare stars was further supported by Karoff et al. (2016) using Ca II H and K data from LAMOST telescope low-dispersion spectra. We also conducted lithium (Li) abundance analysis of these superflare stars (Honda et al. 2015). Li abundance is known to be a clue for investigating the stellar age (e.g., Skumanich 1972; Takeda et al. 2010). Many of the superflare stars tend to show high Li abundance, which is also consistent with Wichmann et al. (2014), but there are some objects that have low Li abundance and rotate slowly.

These results from our previous spectroscopic observations support that even old, slowly rotating stars similar to the Sun can have large starspots and superflares. However, more spectroscopic observations are still needed for the following reasons: Among $\sim$300 solar-type superflare stars found from *Kepler* data, only 34 stars ($\sim$10%) have been confirmed to be single solar-type stars. This means that as for the remaining $\sim$90% of the 300 solar-type stars, the statistical studies on superflares using *Kepler* data are not established in a strict sense. In particular, the number of superflare stars rotating as slowly as the Sun ($P_{rot} \sim 25$ days) that were spectroscopically investigated is only a few in the above previous studies and is

not enough for considering whether the Sun can have superflares on the basis of spectroscopic data.

In this study, we have conducted new spectroscopic observations of solar-type superflare stars that were found from *Kepler* 1-minute cadence data (Maehara et al. 2015). In this new study, we used the Echelle Spectrograph of the Apache Point Observatory (APO) 3.5 m telescope. This spectrograph has a wavelength coverage of 3200–10000 Å, which enabled us to take both Ca II H and K ($\lambda\lambda$3968 and 3934) and Ca II λ8542 lines simultaneously. In the first half of this paper (Sections 2–4), we report the results of these new spectroscopic observations. We describe the selection of the target stars and the details of our observations in Section 2. In Section 3 (and Appendix A), we check the binarity of the targets and then estimate various stellar parameters on the basis of the spectroscopic data. In Section 4, we comment on the estimated stellar parameters, including Li abundances, and discuss rotational velocity and chromospheric activities, comparing with the quasi-periodic brightness variations of *Kepler* data.

The recent *Gaia*-DR2 stellar radius data (e.g., Berger et al. 2018) have suggested the possibility of severe contaminations of subgiant stars in the classification of *Kepler* solar-type (G-type main-sequence) stars used for the statistical studies of superflares described above. The classification of solar-type stars in our previous studies (Shibayama et al. 2013 and Maehara et al. 2015) was based on T_{eff} and $\log g$ values from the *Kepler* Input Catalog (KIC; Brown et al. 2011; Huber et al. 2014). However, most of those T_{eff} and $\log g$ values are based on photometric methods (see Brown et al. 2011 and Huber et al. 2014 for details), and there can be large differences between the real and catalog values. For example, Brown et al. (2011) reported that uncertainties of T_{eff} and $\log g$ in the initial KIC are $\pm$200 K and 0.4 dex, respectively. There can be a severe contamination of subgiant stars in the sample of solar-type superflare stars in our previous studies. In a strict sense, we cannot even deny an extreme possibility that all of the slowly rotating Sun-like superflare stars in our previous studies were the results of contaminations of subgiant stars. In addition, the *Kepler* solar-type superflare stars discussed in our previous studies can include some number of binary stars. This is a problem, especially for investigating whether even truly Sun-like single stars can have large superflares or not. On the basis of these current situations, in Section 5 we investigate the statistical properties of *Kepler* solar-type superflare stars originally described in our previous studies (Maehara et al. 2012, 2015, 2017; Notsu et al. 2013b; Shibayama et al. 2013), now incorporating *Gaia*-DR2 stellar radius estimates (reported in Berger et al. 2018) and the results of our new spectroscopic observations (Subaru and APO 3.5 m observations).

Finally in Sections 6.1–6.2, we summarize the latest view of superflares on solar-type stars found from our series of studies using *Kepler* data, by including the recent updates using APO 3.5 m telescope spectroscopic observations and *Gaia*-DR2 data. We also mention implications for future studies in Section 6.3.

2. APO 3.5 m Spectroscopic Observations and Data Reduction

As target stars of our new spectroscopic observations, we selected all 23 solar-type superflare stars reported in

Maehara et al. ([2015](#)) on the basis of *Kepler* 1-minute time-cadence data. The names of these 23 stars and their stellar parameters are listed in Table [1](#). Among these 23 stars, 18 are identified in Berger et al. ([2018](#)), which is the catalog combining parallaxes from *Gaia* Data Release 2 (*Gaia*-DR2) with those from the DR25 *Kepler* Stellar Properties Catalog (DR25-KSPC; Mathur et al. [2017](#)). We note that there are no slowly rotating stars with their rotation period $P_{\rm rot}$ longer than 20 days in these 23 target stars since no superflare stars with $P_{\rm rot} > 20$ days were reported in Maehara et al. ([2015](#)). That might be related to the fact that the fraction of slowly rotating stars is smaller in the *Kepler* 1-minute cadence data compared with the long-cadence data because of the initial target selection and observation time allocation of *Kepler* (see the second paragraph of page 5 of Maehara et al. [2015](#) for details).

Our new spectroscopic observations were carried out by using the ARC Echelle Spectrograph (ARCES; Wang et al. [2003](#)) attached to the ARC 3.5 m telescope at APO. The wavelength resolution ($R = \lambda/\Delta\lambda$) is ∼32,000, and the spectral coverage is 3200–10000 Å. Data reduction (bias subtraction, flat-fielding, aperture determination, scattered light subtraction, spectral extraction, wavelength calibration, normalization by the continuum, and heliocentric radial velocity [RV] correction)[15] was conducted using the ECHELLE package of the IRAF[16] and PyRAF[17] software.

For the process of wavelength calibration, we took exposures of a thorium–argon (Th–Ar) lamp at the start and end of each half night of observation. However, ARCES spectral data have some systematic drift on CCD over a few hours. This drift is most likely due to the thermal changes of the prisms with temperature, as described in Section 3.1 of Wang et al. ([2003](#)). This drift is a bit large in the early half night (∼2–3 km s^{-1}) compared with that in the later half night ($\lesssim$1–2 km s^{-1}). We remove this systematic drift by using the wavelength of ∼10 telluric absorption lines around 6890–6910 Å.

When we normalize the spectral orders around Ca II H and K lines ($\lambda\lambda3968$ and 3934), as also done in Morris et al. ([2017](#)), we fit the spectrum of an early-type standard star with a high-order polynomial to measure the blaze function, and we then divide the spectra of target stars by the polynomial fit to normalize each spectral order. We use this method since there are many absorption lines in the blue part of the spectra, and it is difficult to directly fit the continuum component of spectra of the target stars. When normalizing the red part of the spectra ($\gtrsim$5000 Å), which we use for the estimations of stellar parameters (except for Ca II H and K line analyses) in this study, we directly fit the target star spectra with a high-order polynomial to measure the blaze function. After that, we shifted the normalized spectra in wavelength into the rest-frame by removing their radial velocities. We remove the RV by maximizing the cross-correlation of our ARCES spectra with solar spectra in the wavelength range of 6212–6220 Å, where we conduct $v \sin i$ measurements in Appendix [A.4](#).

The observation date of each target superflare star and the obtained signal-to-noise ratio (S/N) are shown in Table [2](#). We selected 23 target superflare stars, and for the 18 brightest superflare stars, we obtained high enough S/N data for scientific discussions in this paper. However, the other five stars (KIC 6032920, KIC 10528093, KIC 10646889, KIC 9655134, and KIC 10745663) in the bottom of Table [1](#) are much fainter ($K_p \geqslant 13.5$ mag) compared with the other 18 relatively bright target stars ($K_p \leqslant 12.4$ mag). The data quality of our spectroscopic data for four of them (KIC 6032920, KIC 10528093, KIC 10646889, and KIC 9655134) is not high enough for detailed scientific discussions in this paper. As for KIC 10745663, we only took a slit viewer image, and we have no spectroscopic data since it is too faint ($K_p = 14.3$ mag).

In addition to the above 23 target superflare stars, we repeatedly observed 28 bright solar-type comparison stars as references of solar-type stars. The name and basic parameters of these 28 comparison stars, observation date, and S/N of each observation are listed in Table [3](#). (The original sources of these stars are in the footnotes of Table [3](#).) All of these 28 stars were also observed in the California Planet Search (CPS) program (Isaacson & Fischer [2010](#)), and we use these solar-type stars to calibrate Ca II H and K S-index in Appendix [A.6](#).

3. Analyses and Results of the APO 3.5 m Spectroscopic Observations

For the first step of our analysis we checked the binarity, as we have done in our previous studies (e.g., Notsu et al. [2015a](#), [2017](#)). The details of the analyses of binarity are described in Appendix [A.1](#). As a result, we regard five target stars as binary stars among the 18 superflare stars that we newly observed using the APO 3.5 m telescope in this study. These five stars are shown in the second column of Table [1](#). We treat the remaining 13 stars (among these 18 stars observed using APO 3.5 m) as single stars in this paper, since they do not show any evidence of binarity within the limits of our analyses. In the following, we conduct a detailed analysis for these 13 single stars.

We then estimated various stellar parameters of the target stars, using our spectroscopic data. The details of the analyses and results are described in Appendices [A.2](#)–[A.8](#) of this paper. We estimated stellar atmospheric parameters ($T_{\rm eff}$, $\log g$, and [Fe/H]) in Appendix [A.2](#), stellar radius (R_{Gaia} and $R_{\rm spec}$) in Appendix [A.3](#), and the projected rotational velocity ($v \sin i$) in Appendix [A.4](#). We show measurement results of the intensity of Ca II $\lambda8542$ and Hα lines in Appendix [A.5](#), Ca II H and K S-index in Appendix [A.6](#), and Ca II H and K flux values in Appendix [A.7](#). We also describe the analysis of lithium (Li) abundance of the target stars in Appendix [A.8](#). The resultant parameters are listed in Tables [4](#) and [5](#).

4. Discussions on the Results from our APO 3.5 m Spectroscopic Observations

4.1. Binarity

In Section [3](#) and Appendix [A.1](#), we summarize the results of our new APO 3.5 m spectroscopic observations of 18 superflare stars.

We reported that more than half (13 stars) among these 18 stars have no obvious evidence of being in a binary system. Combined with the results of the 50 stars that we observed with Subaru telescope in Notsu et al. ([2015a](#)), we have conducted spectroscopic observations of 64 superflare stars in total (Table [6](#)). Four stars (KIC 4742436, KIC 4831454, KIC

---

[15] An ARCES data reduction manual by J. Thorburn is available at http://astronomy.nmsu.edu:8000/apo-wiki/wiki/ARCES.

[16] IRAF is distributed by the National Optical Astronomy Observatories, which are operated by the Association of Universities for Research in Astronomy, Inc., under cooperate agreement with the National Science Foundation.

[17] PyRAF is part of the stsci_python package of astronomical data analysis tools and is a product of the Science Software Branch at the Space Telescope Science Institute.

Table 1
Basic Data of Our Target Superflare Stars

Star Name	Binarity[a]	$P_{\rm rot}$[b] (days)	$N_{\rm flare}$[b]	K_p[c] (mag)	$T_{\rm eff,DR25}$[c] (K)	$(\log g)_{\rm DR25}$[c] (cm s^{-2})	$[{\rm Fe/H}]_{\rm DR25}$[c]	$R_{\rm DR25}$[c] ($R_\odot$)	d_{Gaia}[d] (pc)	R_{Gaia}[d] ($R_\odot$)	EvoFlg[e]	BinFlg[e]
KIC 10532461	no	7.14	1	8.8	5689^{+189}_{-172}	$4.24^{+0.26}_{-0.19}$	$-0.28^{+0.30}_{-0.25}$	$1.15^{+0.37}_{-0.34}$	$45.8^{+0.1}_{-0.1}$	$0.78^{+0.06}_{-0.05}$	0	0
KIC 11652870	no	8.54	1	9.1	5516^{+149}_{-149}	$4.37^{+0.19}_{-0.20}$	$-0.16^{+0.27}_{-0.30}$	$0.98^{+0.13}_{-0.18}$	$51.6^{+0.1}_{-0.1}$	$0.78^{+0.06}_{-0.05}$	0	0
KIC 9139151	no	6.15	2	9.2	6299^{+62}_{-81}	$4.38^{+0.01}_{-0.01}$	$0.08^{+0.10}_{-0.15}$	$1.17^{+0.03}_{-0.04}$	$102.7^{+0.3}_{-0.3}$	$1.14^{+0.05}_{-0.05}$	0	0
KIC 4554830	no	7.73	1	10.3	5666^{+76}_{-76}	$4.16^{+0.01}_{-0.01}$	$0.36^{+0.10}_{-0.15}$	$1.43^{+0.07}_{-0.05}$	$173.4^{+0.7}_{-0.7}$	$1.44^{+0.06}_{-0.06}$	1	0
KIC 4742436[f,g]	no	2.34	1	10.6	5914^{+163}_{-133}	$4.11^{+0.33}_{-0.14}$	$-0.70^{+0.35}_{-0.20}$	$1.30^{+0.28}_{-0.42}$	$\cdots$	$\cdots$	$\cdots$	$\cdots$
KIC 4831454[f]	no	5.19	8	10.7	5479^{+146}_{-146}	$4.60^{+0.05}_{-0.11}$	$-0.46^{+0.30}_{-0.30}$	$0.74^{+0.13}_{-0.06}$	$123.8^{+0.4}_{-0.4}$	$0.91^{+0.07}_{-0.06}$	0	0
KIC 8656342	no	17.50	2	10.9	5959^{+80}_{-80}	$4.07^{+0.03}_{-0.03}$	$-0.02^{+0.20}_{-0.15}$	$1.59^{+0.10}_{-0.09}$	$299.8^{+2.4}_{-2.4}$	$1.70^{+0.07}_{-0.07}$	1	0
KIC 9652680[f]	no	1.47	7	11.2	5819^{+131}_{-160}	$4.57^{+0.03}_{-0.17}$	$-0.32^{+0.30}_{-0.30}$	$0.82^{+0.20}_{-0.07}$	$220.2^{+1.1}_{-1.1}$	$1.09^{+0.08}_{-0.07}$	0	0
KIC 6777146	no	7.21	1	11.3	6103^{+169}_{-169}	$4.34^{+0.15}_{-0.13}$	$-0.56^{+0.30}_{-0.30}$	$1.04^{+0.19}_{-0.19}$	$331.6^{+2.9}_{-2.9}$	$1.60^{+0.12}_{-0.11}$	1	0
KIC 8508009	no	2.95	1	11.5	6256^{+156}_{-188}	$4.37^{+0.09}_{-0.14}$	$-0.26^{+0.25}_{-0.15}$	$1.09^{+0.24}_{-0.15}$	$285.9^{+1.8}_{-1.8}$	$1.15^{+0.09}_{-0.08}$	0	0
KIC 11610797[f]	no	1.62	8	11.5	5868^{+78}_{-78}	$4.03^{+0.20}_{-0.09}$	$-0.02^{+0.15}_{-0.15}$	$1.67^{+0.27}_{-0.40}$	$277.1^{+1.6}_{-1.6}$	$1.17^{+0.05}_{-0.05}$	0	0
KIC 11253827	no	13.40	2	11.9	5593^{+111}_{-111}	$4.45^{+0.07}_{-0.10}$	$0.02^{+0.15}_{-0.15}$	$0.95^{+0.12}_{-0.08}$	$223.7^{+1.8}_{-1.8}$	$0.90^{+0.04}_{-0.04}$	0	0
KIC 6291837	no	14.30	1	12.4	6212^{+111}_{-136}	$4.31^{+0.10}_{-0.12}$	$-0.04^{+0.15}_{-0.15}$	$1.21^{+0.21}_{-0.14}$	$523.2^{+15.8}_{-14.9}$	$1.42^{+0.07}_{-0.07}$	0	0
KIC 11551430[g]	RV(+VB)	4.26	89	10.7	5648^{+113}_{-90}	$4.02^{+0.22}_{-0.11}$	$-0.08^{+0.15}_{-0.10}$	$1.61^{+0.30}_{-0.36}$	$\cdots$	$\cdots$	$\cdots$	$\cdots$
KIC 4543412	RV	2.16	13	11.2	5472^{+163}_{-147}	$4.44^{+0.14}_{-0.25}$	$-0.30^{+0.30}_{-0.30}$	$0.88^{+0.24}_{-0.14}$	$148.2^{+0.6}_{-0.6}$	$0.96^{+0.07}_{-0.06}$	0	0
KIC 11128041	SB2+RV	7.36	2	10.8	5913^{+133}_{-162}	$4.58^{+0.03}_{-0.14}$	$-0.50^{+0.25}_{-0.30}$	$0.80^{+0.16}_{-0.06}$	$196.5^{+0.8}_{-0.8}$	$1.21^{+0.09}_{-0.08}$	0	0
KIC 10338279[g]	SB2	6.53	4	12.0	5615^{+152}_{-152}	$4.48^{+0.10}_{-0.14}$	$-0.44^{+0.30}_{-0.30}$	$0.84^{+0.19}_{-0.10}$	$\cdots$	$\cdots$	$\cdots$	$\cdots$
KIC 7093428[g]	VB	0.51	19	11.0	6181^{+167}_{-223}	$2.77^{+0.54}_{-0.18}$	$0.07^{+0.25}_{-0.55}$	$12.27^{+1.29}_{-7.32}$	$\cdots$	$\cdots$	$\cdots$	$\cdots$
KIC 6032920[g]	$\cdots$	3.16	6	13.5	5862^{+141}_{-159}	$4.58^{+0.03}_{-0.18}$	$-0.52^{+0.30}_{-0.30}$	$0.79^{+0.21}_{-0.07}$	$\cdots$	$\cdots$	$\cdots$	$\cdots$
KIC 10528093	$\cdots$	12.20	2	13.6	5334^{+159}_{-143}	$4.54^{+0.10}_{-0.07}$	$-0.54^{+0.35}_{-0.30}$	$0.75^{+0.08}_{-0.08}$	$1497.0^{+37.3}_{-35.6}$	$3.34^{+0.26}_{-0.24}$	1	0
KIC 10646889	$\cdots$	4.70	8	13.6	5674^{+152}_{-152}	$4.44^{+0.13}_{-0.17}$	$-0.36^{+0.30}_{-0.30}$	$0.90^{+0.23}_{-0.12}$	$716.1^{+7.1}_{-7.0}$	$1.35^{+0.10}_{-0.09}$	0	0
KIC 9655134	$\cdots$	15.50	1	13.6	5397^{+160}_{-160}	$4.55^{+0.09}_{-0.07}$	$-0.66^{+0.35}_{-0.30}$	$0.73^{+0.09}_{-0.08}$	$457.6^{+4.3}_{-4.2}$	$0.93^{+0.07}_{-0.06}$	0	0
KIC 10745663	$\cdots$	3.13	7	14.3	6014^{+162}_{-198}	$4.49^{+0.05}_{-0.21}$	$-0.08^{+0.25}_{-0.35}$	$0.96^{+0.30}_{-0.10}$	$1480.6^{+38.0}_{-36.3}$	$1.82^{+0.14}_{-0.13}$	1	0

Notes.

[a] For details of this column, see Appendix A.1. "No" means that the star shows no evidence of being in a binary system. "SB2" corresponds to stars that have a double-lined profile. "RV" means that the star shows RV changes. "VB" means that the star has visual companion stars. The bottom five stars (KIC 6032920, KIC 10528093, KIC 10646889, KIC 9655134, and KIC 10745663) are much fainter compared with the other target stars. The data quality of our spectroscopic data for four of them (KIC 6032920, KIC 10528093, KIC 10646889, and KIC 9655134) is not high enough to judge whether they show any evidence of a binary system. As for the faintest, KIC 10745663, we have no spectroscopic data.

[b] Stellar rotation period ($P_{\rm rot}$) and number of superflares ($N_{\rm flare}$) reported in Maehara et al. (2015).

[c] *Kepler* band magnitude (K_p), effective temperature ($T_{\rm eff,DR25}$), surface gravity ($(\log g)_{\rm DR25}$), metallicity ($[{\rm Fe/H}]_{\rm DR25}$), and stellar radius ($R_{\rm DR25}$) in DR25-KSPC (Mathur et al. 2017).

[d] Stellar distance (d_{Gaia}) and stellar radius (R_{Gaia}) in Berger et al. (2018). They derived these values by combining parallaxes from *Gaia* Data Release 2 with the DR25-KSPC.

[e] Evolutionary Flag (EvoFlg) and Binary Flag (BinFlg) reported in Berger et al. (2018), on the basis of R_{Gaia} values. The evolutionary flags are as follows: 0 = main-sequence dwarf; 1 = subgiant. The binary flags are as follows: 0 = no indication of binary; 1 = binary candidate based on R_{Gaia} only; 2 = AO-detected binary only (Ziegler et al. 2018); 3 = binary candidate based on R_{Gaia} and AO-detected binary.

[f] As described in Appendix A.1, we have also conducted spectroscopic observations of these four stars (KIC 4742436, KIC 4831454, KIC 9652680, and KIC 11610797) using the Subaru telescope (Notsu et al. 2015a, 2015b; Honda et al. 2015).

[g] As for these five stars (KIC 4742436, KIC 11551430, KIC 10338279, KIC 7093428, and KIC 6032920), there are no d_{Gaia} and R_{Gaia} values reported in Berger et al. (2018).

Table 2
APO 3.5 m Telescope Observations of Target Superflare Stars

Star Name	Remarks[a]	Binarity[b]	Date (UT)[c]	Time (UT)[c]	RV[d] (km s^{-1})	S/N(8542)[e]	S/N(Hα)[e]	S/N(HK)[e]
KIC 10532461		no	2016 Aug 23	02:16:35.23	8.0	68	95	33
⋯		⋯	2017 Apr 10	08:11:00.28	8.3	68	97	22
⋯		⋯	2017 Sep 23	01:44:20.11	8.6	110	148	41
⋯		⋯	2017 Oct 31	02:01:19.03	8.5	27	36	9
⋯		⋯	comb	⋯		148	202	64
KIC 11652870		no	2016 Aug 21	04:53:17.80	−3.9	49	68	25
⋯		⋯	2017 Apr 10	08:33:38.85	−3.5	70	99	26
⋯		⋯	2017 Oct 15	01:34:58.94	−3.4	64	86	24
⋯		⋯	2017 Oct 29	03:47:57.35	−3.5	65	89	19
⋯		⋯	comb	⋯		124	172	54
KIC 9139151		no	2017 Apr 10	08:57:09.20	−28.4	68	100	33
⋯		⋯	2017 Jun 5	10:53:45.74	−28.2	67	99	43
⋯		⋯	2017 Oct 29	03:32:52.19	−28.5	71	104	28
⋯		⋯	comb	⋯	⋯	118	175	71
KIC 4554830		no	2017 Apr 10	09:24:50.91	−21.9	54	77	22
⋯		⋯	2017 Sep 23	02:11:54.20	−21.2	64	88	25
⋯		⋯	2017 Oct 3	05:32:26.76	−22.5	43	58	12
⋯		⋯	comb	⋯	⋯	93	130	38
KIC 4742436		no	2017 Apr 10	11:54:08.11	−54.6	34	49	20
⋯	(1)	⋯	2012 Aug 7	06:46:04.8	−54.5	140	210	⋯
⋯	(1)	⋯	2012 Aug 8	06:04:19.2	−54.6	140	190	⋯
⋯	(1)	⋯	2012 Aug 9	06:50:24.0	−54	100	160	⋯
KIC 4831454		no	2017 Apr 10	10:30:13.61	−27.4	45	63	21
⋯	(1)	⋯	2012 Aug 7	07:03:21.6	−26.4	150	220	⋯
⋯	(1)	⋯	2012 Aug 8	06:21:36.0	−26.6	140	190	⋯
⋯	(1)	⋯	2012 Aug 9	07:12:00.0	−27.2	110	170	⋯
KIC 8656342		no	2017 May 3	08:09:21.76	−4.1	49	70	21
⋯		⋯	2017 Sep 23	04:03:53.94	−4.6	25	34	11
⋯		⋯	2017 Oct 3	05:07:22.31	−4.3	45	62	19
⋯		⋯	comb	⋯	⋯	71	99	35
KIC 9652680		no	2017 May 3	10:01:13.48	−20.5	43	61	23
⋯	(1)	⋯	2012 Aug 7	07:19:12.0	−21.6	110	170	⋯
⋯	(1)	⋯	2012 Aug 8	06:41:45.6	−20.5	90	150	⋯
⋯	(1)	⋯	2012 Aug 9	06:25:55.2	−22.3	90	140	⋯
KIC 6777146		no	2017 May 3	10:34:00.37	−7.3	41	58	25
⋯		⋯	2017 Oct 3	01:51:57.37	−6.9	41	56	19
⋯		⋯	2017 Oct 29	03:07:44.74	−7.7	41	57	17
⋯		⋯	comb	⋯	⋯	71	99	42
KIC 8508009		no	2017 May 3	11:06:38.23	−28.8	36	52	22
⋯		⋯	2017 Oct 3	02:24:30.58	−28.8	37	51	18
⋯		⋯	2017 Oct 7	06:30:24.29	−28.8	27	38	8
⋯		⋯	comb	⋯	⋯	58	81	34
KIC 11610797		no	2017 Jun 5	07:42:39.45	−6.3	36	51	20
⋯	(1)	⋯	2012 Aug 7	08:32:38.4	−10.3	110	170	⋯
⋯	(1)	⋯	2012 Aug 8	07:17:45.6	−11.6	100	150	⋯
⋯	(1)	⋯	2012 Aug 9	07:58:04.8	−10.4	80	130	⋯
KIC 11253827		no	2017 Jun 5	08:15:13.95	−13.6	32	44	16
⋯		⋯	2017 Oct 3	02:57:04.29	−13.5	32	44	13
⋯		⋯	2017 Oct 7	05:57:49.26	−14.1	26	35	7
⋯		⋯	comb	⋯	⋯	52	71	24
KIC 6291837		no	2017 Jun 5	09:22:11.96	−34.5	34	50	23
⋯		⋯	2017 Oct 7	04:52:41.67	−36.7	22	31	8
⋯		⋯	comb	⋯	⋯	41	58	29
KIC 11551430A	(2)	RV(+VB)	2017 Apr 10	11:03:00.04	−14.9	43	60	20
⋯		⋯	2017 Sep 23	02:46:47.94	5.4	53	71	21
⋯		⋯	2017 Oct 3	04:34:48.04	−54.0	53	72	20
⋯		⋯	comb	⋯	⋯	86	116	41
KIC 11551430B	(2)	VB	2017 Apr 10	11:28:42.47	−25.5	11	16	4
KIC 4543412		RV	2017 May 3	09:28:39.20	27.3	45	61	20
⋯		⋯	2017 Sep 23	06:28:58.19	7.6	24	31	4
⋯		⋯	2017 Oct 3	04:02:13.73	6.4	45	60	15
⋯		⋯	2017 Oct 7	05:25:15.88	−24.4	38	51	8
⋯		⋯	comb	⋯	⋯	78	103	31

Table 2
(Continued)

Star Name	Remarks[a]	Binarity[b]	Date (UT)[c]	Time (UT)[c]	RV[d] (km s^{-1})	S/N(8542)[e]	S/N(Hα)[e]	S/N(HK)[e]
KIC 11128041		SB2+RV	2017 May 3	07:40:28.97	⋯	46	65	21
⋯		⋯	2017 Sep 23	03:19:21.25	⋯	42	57	18
⋯		⋯	2017 Oct 29	04:03:06.11	⋯	32	46	10
KIC 10338279		SB2	2017 Jun 5	08:49:33.49	⋯	42	58	20
KIC 7093428	(3)	VB	2017 May 3	08:56:03.72	−44.6	42	62	28
KIC 6032920		⋯	2017 Dec 10	02:30:50.58	−58.3	14	21	low S/N
KIC 10528093		⋯	2017 Dec 10	03:46:14.03	34.0	10	16	low S/N
KIC 10646889		⋯	2017 Dec 10	03:10:31.49	−45.1	10	16	low S/N
KIC 9655134		⋯	2017 Dec 10	04:20:18.10	−12.6	9	15	low S/N
KIC 10745663		⋯	No-spectra	No-spectra	No-spectra	No-spectra	No-spectra	No-spectra

Notes.

[a] (1) As described in Appendix A.1, we also conducted spectroscopic observations of these four stars (KIC 4742436, KIC 4831454, KIC 9652680, and KIC 11610797) using the Subaru telescope (Notsu et al. 2015a). RV values of these observations are included here for reference. (2) KIC 11551430 is found to be a visual binary (KIC 11551430A and KIC 1551430B), as described in Appendix A.1. We took spectra of each component of the visual binary separately and measured parameters of each of them. (3) As described in Appendix A.1, KIC 7093428 has two fainter companion stars, and pixel data analyses suggest that flares occur on these companion stars. Since companion stars are faint, here we only measure parameters of the main (brightest) star for reference, though we do not use these values in the main discussion of this paper.

[b] Same as in footnote a of Table 1. See also Appendix A.1.

[c] Observation date (Universal Time; format: YYYY-MM-DD) and middle time (Universal Time; format: hh:mm:ss) of each exposure. "Comb" corresponds to the co-added spectra that all APO spectra of each target star are combined into.

[d] Radial velocity (see Appendix A.1).

[e] S/N of the spectral data around Ca II λ8542 (S/N(8542)), Hα λ6563 (S/N(Hα)), and Ca II H and K λ3934/λ3938 (S/N(HK)).

9652680, and KIC 11610797) among these 64 stars were observed in both studies. As a result, 43 stars among the total 64 solar-type superflare stars are classified as "single" stars. However, we need to remember here that we cannot completely exclude the possibility that some of these 43 "single" superflare stars have companions since observations and analyses in this study are limited, as we have also described in detail in Section 4.1 of Notsu et al. (2015a).

For example, as for the target stars with "multiple" observations in this study, only those showing large RV changes would likely be detected in the randomly spaced observations. Targets with longer-period orbits would require more observations spaced accordingly. Thus, only the short-period systems likely would be captured, and even then some would be missed by accident owing to poorly spaced observations (e.g., the case that the time differences between the observations correspond to the orbital period of the binary system). We must note these points, but we consider that more detailed analyses of binarity are not really necessary for the overall discussion of stellar properties of superflare stars in this paper.

Two target stars, KIC 11551430 and KIC 7093428, are classified as visual binary stars on the basis of the slit viewer images, Figures 19 and 20 in Appendix A.1. Pixel count data of these two stars suggested that superflares occur on the primary star KIC 11551430A as for the visual binary system KIC 11551430, while flares occur on the fainter companion stars KIC 7093428B or KIC 7093428C as for the system KIC 7093428. Measurement results of rotation velocity $v \sin i$ and chromospheric line intensities in this study (listed in Tables 4 and 5) support this suggestion. As for KIC 11551430, the primary star KIC 11551430A rotates much more rapidly ($v \sin i \sim 18.8$ km s^{-1}) than the companion star KIC 11551430B ($v \sin i < 4$ km s^{-1}). Moreover, the primary KIC 11551430A shows strong chromospheric emissions, while the

companion KIC 11551430B does not show any strong emissions (Figures 26–28). The primary KIC 11551430A can have much higher probability of generating superflares since superflare stars are generally well characterized with rapid rotation velocity and high chromospheric activity levels. In contrast, the primary KIC 7093428A has no strong chromospheric emissions (Figures 26–28), and this primary star does not show any properties as superflare stars. It is therefore highly possible that flares occur on the fainter companion stars KIC 7093428B or KIC 7093428C mentioned above.

As seen in Table 1, stars identified as binary stars tend to show a larger number of flares. For example, KIC 11551430 and KIC 4543412, which show RV shifts, have $N_{\rm flare} = 89$ and 13, respectively. All the stars identified as "single" stars have $N_{\rm flare} < 10$ in Table 1. As a result, among the 187 superflares (on 23 stars) from *Kepler* 1-minute cadence data in Maehara et al. (2015), at least 127 events are found to occur on binary stars. This means that a large portion of the superflare data of the *Kepler* 1-minute cadence sample (Maehara et al. 2015) are contaminated by binary stars (e.g., close binary stars). The data from Maehara et al. (2015) are therefore not enough for investigating the possibility of superflares on Sun-like stars, and we need more investigations by increasing the number of single superflare stars (e.g., See also the first paragraph of Section 6.3).

4.2. Estimated Atmospheric Parameters

We estimated the atmospheric parameters ($T_{\rm eff}$, $\log g$, and [Fe/H]) of the target superflare stars in Appendix A.2. The measured values of the 13 single target stars of this observation are $T_{\rm eff} = 5400$–6300 K, $\log g = 3.9$–4.8, and [Fe/H] = $(-0.3) - (+0.3)$, respectively (Figure 1). This indicates that the stellar parameters of these 13 single target superflare stars are roughly in the range of solar-type (G-type main-sequence)

Table 3
Observations of Comparison Stars to Calibrate Ca II H and K S-index

Star Name	Remarks[a]	$T_{\rm eff}$[b] (K)	$B-V$[b] (mag)	$S_{\rm MWO}$[c]	Date (UT)[d]	Time (UT)[d]	S/N(8542)[e]	S/N(HK)[e]	$r_0(8542)$	$S_{\rm APO}$	$S_{\rm HK}$	$\log \mathcal{F}^{+}_{\rm 2HK}$ (erg/(cm^2 s))	$\log R^{+}_{\rm HK}$
HIP 9519[e]	(1)	5899	0.594	0.417	2016 Nov 7	08:01:15.75	134	64	0.50	0.0185	0.416	6.77	−4.07
...	...	...	...	...	2018 Feb 24	01:43:15.26	86	31	0.46	0.0167	0.376	6.71	−4.12
HIP 19793[e]	(1)	5833	0.620	0.347	2016 Nov 7	10:00:22.79	108	64	0.42	0.0165	0.372	6.66	−4.16
HIP 21091[e]	(1)	5857	0.601	0.352	2016 Nov 7	10:13:11.72	76	42	0.44	0.0163	0.367	6.69	−4.14
...	...	...	...	...	2018 Jan 5	08:29:18.26	102	21	0.44	0.0167	0.376	6.70	−4.12
HIP 22175[e]	(1)	5667	0.637	0.213	2016 Nov 7	10:25:47.00	116	58	0.26	0.0104	0.238	6.36	−4.41
...	...	...	...	...	2018 Jan 2	08:20:23.05	119	27	0.26	0.0104	0.238	6.36	−4.41
...	...	...	...	...	2018 Feb 24	02:18:39.39	278	37	0.26	0.0101	0.230	6.34	−4.43
HIP 27980[e]	(1)	5854	0.615	0.205	2016 Nov 7	10:53:12.14	105	58	0.23	0.0098	0.226	6.35	−4.48
...	...	...	...	...	2018 Jan 2	09:10:44.10	116	31	0.23	0.0091	0.208	6.29	−4.54
HIP 35185[e]	(1)	5830	0.601	0.341	2016 Nov 7	11:16:44.46	74	43	0.41	0.0150	0.338	6.64	−4.17
...	...	...	...	...	2018 Jan 2	10:09:19.57	97	35	0.41	0.0153	0.346	6.65	−4.16
...	...	...	...	...	2018 Feb 1	07:48:08.24	95	38	0.43	0.0157	0.354	6.67	−4.15
...	...	...	...	...	2018 Apr 30	02:31:36.03	70	31	0.43	0.0158	0.357	6.67	−4.14
HIP 37971[e]	(1)	5774	0.642	0.322	2016 Nov 7	11:28:03.37	69	38	0.38	0.0157	0.354	6.59	−4.20
...	...	...	...	...	2018 Jan 5	09:15:25.35	92	43	0.36	0.0148	0.334	6.56	−4.24
...	...	...	...	...	2018 Apr 30	02:44:36.92	77	36	0.39	0.0161	0.364	6.61	−4.19
HIP 38228[e]	(1)	5631	0.657	0.406	2016 Nov 7	11:37:22.49	117	65	0.45	0.0181	0.407	6.65	−4.10
...	...	...	...	...	2018 Jan 4	08:32:28.21	130	59	0.42	0.0164	0.370	6.60	−4.16
...	...	...	...	...	2018 Jan 5	09:05:22.10	137	63	0.44	0.0173	0.389	6.63	−4.13
...	...	...	...	...	2018 Feb 1	07:59:52.56	160	73	0.48	0.0186	0.418	6.67	−4.09
...	...	...	...	...	2018 Apr 30	02:55:31.81	109	49	0.42	0.0167	0.377	6.61	−4.14
HIP 51652[e]	(1)	5870	0.620	0.214	2016 Nov 7	12:12:29.36	72	33	0.25	0.0101	0.230	6.35	−4.48
...	...	...	...	...	2016 Dec 11	09:39:04.98	63	23	0.24	0.0099	0.226	6.33	−4.49
...	...	...	...	...	2018 Jan 5	11:09:21.87	102	50	0.24	0.0099	0.228	6.34	−4.49
HIP 79068[e]	(1)	5809	0.615	0.235	2016 Dec 11	12:53:01.25	52	25	0.28	0.0120	0.272	6.48	−4.33
...	...	...	...	...	2018 Jan 5	13:02:29.03	71	32	0.27	0.0109	0.248	6.42	−4.39
HIP 117184[e]	(1)	5890	0.609	0.354	2016 Nov 7	07:31:06.71	72	33	0.39	0.0153	0.346	6.64	−4.20
18Sco	(2)	5794	0.618	0.170	2016 Aug 21	02:18:54.94	222	98	0.2	0.0074	0.172	6.13	−4.68
...	...	...	...	...	2016 Aug 23	02:00:15.72	198	102	0.23	0.0082	0.188	6.21	−4.60
...	...	...	...	...	2017 May 3	07:19:54.42	238	97	0.21	0.0082	0.190	6.21	−4.59
59Vir	(2)	6017	0.573	0.324	2017 Apr 10	07:23:42.69	90	52	0.4	0.0154	0.347	6.70	−4.17
...	...	...	...	...	2017 Dec 31	12:53:01.38	212	106	0.38	0.0144	0.326	6.66	−4.21
...	...	...	...	...	2018 Jan 2	12:55:33.66	134	64	0.39	0.0144	0.327	6.66	−4.21
61Vir	(2)	5565	0.678	0.169	2017 Apr 10	07:31:23.31	107	41	0.21	0.0074	0.171	6.03	−4.70
HIP 100963	(2)	5751	0.620	0.227	2016 Oct 12	01:01:03.01	160	98	0.23	0.0085	0.195	6.24	−4.55
...	...	...	...	...	2016 Oct 14	00:52:57.66	170	106	0.26	0.0088	0.203	6.27	−4.52
...	...	...	...	...	2017 Jun 5	07:19:50.33	160	69	0.23	0.0087	0.200	6.26	−4.54
...	...	...	...	...	2017 Oct 3	01:17:15.01	154	71	0.22	0.0085	0.196	6.24	−4.55
...	...	...	...	...	2017 Oct 7	01:11:38.75	133	56	0.24	0.0089	0.206	6.28	−4.51
...	...	...	...	...	2017 Oct 29	01:40:46.82	103	51	0.24	0.0088	0.202	6.27	−4.53
...	...	...	...	...	2017 Oct 31	00:37:45.39	116	55	0.27	0.0089	0.204	6.28	−4.52
...	...	...	...	...	2017 Dec 10	02:08:12.60	137	41	0.23	0.0086	0.199	6.26	−4.54
HD 11131	(3)	5735	0.654	0.299	2017 Dec 10	05:10:03.30	171	58	0.37	0.0143	0.324	6.52	−4.27
HD 114710	(3)	6006	0.572	0.222	2017 Dec 31	12:45:12.67	235	120	0.28	0.0104	0.238	6.46	−4.40
...	...	...	...	...	2018 Jan 2	12:40:47.75	154	76	0.27	0.0103	0.236	6.46	−4.41
...	...	...	...	...	2018 Feb 1	10:31:27.18	169	89	0.26	0.0099	0.227	6.43	−4.44

Table 3
(Continued)

Star Name	Remarks[a]	T_{eff}[b] (K)	$B-V$[b] (mag)	S_{MWO}[c]	Date (UT)[d]	Time (UT)[d]	S/N(8542)[e]	S/N(HK)[e]	r_0(8542)	S_{APO}	S_{HK}	$\log \mathcal{F}_{\mathrm{HK}}^{+}$ (erg/(cm^2 s))	$\log R_{\mathrm{HK}}^{+}$
⋯	⋯	⋯	⋯	⋯	2018 Apr 23	05:59:54.81	135	67	0.26	0.0098	0.224	6.42	−4.45
⋯	⋯	⋯	⋯	⋯	2018 Apr 30	04:19:41.44	116	62	0.27	0.0103	0.237	6.46	−4.41
⋯	⋯	⋯	⋯	⋯	2018 May 5	09:21:05.68	180	67	0.26	0.0095	0.219	6.40	−4.47
HD 129333	(3)	5824	0.626	0.695	2017 Oct 3	01:29:23.45	130	36	0.75	0.0286	0.639	6.94	−3.87
⋯	⋯	⋯	⋯	⋯	2017 Dec 31	13:00:47.58	93	37	0.76	0.0309	0.688	6.98	−3.84
⋯	⋯	⋯	⋯	⋯	2018 Jan 2	12:47:38.75	92	35	0.74	0.0292	0.652	6.95	−3.86
⋯	⋯	⋯	⋯	⋯	2018 Feb 1	10:54:29.71	108	45	0.78	0.0321	0.715	7.00	−3.82
⋯	⋯	⋯	⋯	⋯	2018 Feb 24	06:54:57.88	89	29	0.76	0.0310	0.692	6.98	−3.83
⋯	⋯	⋯	⋯	⋯	2018 Apr 23	06:31:24.21	92	39	0.77	0.0318	0.709	6.99	−3.82
⋯	⋯	⋯	⋯	⋯	2018 Apr 30	04:30:19.90	120	51	0.79	0.0319	0.711	7.00	−3.82
⋯	⋯	⋯	⋯	⋯	2018 May 5	09:51:25.55	137	57	0.74	0.0293	0.653	6.95	−3.86
HD 17925	(3)	5183	0.862	0.659	2017 Dec 10	05:32:13.48	238	59	0.54	0.0281	0.626	6.55	−4.06
⋯	⋯	⋯	⋯	⋯	2018 Feb 24	01:53:43.39	170	33	0.57	0.0299	0.667	6.58	−4.03
HD 1835	(3)	5720	0.659	0.319	2017 Oct 29	04:18:11.31	212	66	0.4	0.0157	0.354	6.57	−4.22
⋯	⋯	⋯	⋯	⋯	2017 Oct 31	03:25:37.19	175	53	0.41	0.0156	0.352	6.56	−4.22
⋯	⋯	⋯	⋯	⋯	2017 Dec 10	04:58:32.18	148	32	0.39	0.0155	0.351	6.56	−4.22
HD 190406	(3)	5910	0.600	0.183	2017 Sep 23	01:28:27.37	224	98	0.24	0.0091	0.210	6.32	−4.52
⋯	⋯	⋯	⋯	⋯	2017 Oct 31	02:20:07.29	59	26	0.25	0.0092	0.211	6.32	−4.52
⋯	⋯	⋯	⋯	⋯	2017 Oct 31	03:09:10.26	281	107	0.24	0.0092	0.211	6.32	−4.52
⋯	⋯	⋯	⋯	⋯	2018 May 5	10:19:25.86	156	76	0.23	0.0085	0.195	6.26	−4.58
HD 20630	(3)	5654	0.681	0.379	2017 Oct 31	03:48:26.44	104	21	0.45	0.0182	0.410	6.61	−4.15
⋯	⋯	⋯	⋯	⋯	2017 Oct 31	05:51:54.28	201	31	0.46	0.0178	0.401	6.60	−4.16
⋯	⋯	⋯	⋯	⋯	2017 Dec 10	05:42:11.24	296	121	0.42	0.0170	0.382	6.57	−4.19
⋯	⋯	⋯	⋯	⋯	2018 Jan 5	07:18:21.90	245	34	0.41	0.0158	0.357	6.53	−4.23
⋯	⋯	⋯	⋯	⋯	2018 Feb 24	02:02:44.05	117	43	0.43	0.0171	0.384	6.58	−4.19
HD 206860	(3)	5954	0.587	0.332	2017 Oct 7	06:51:16.37	157	53	0.43	0.0153	0.345	6.67	−4.18
⋯	⋯	⋯	⋯	⋯	2017 Oct 31	02:35:20.55	136	63	0.44	0.0151	0.341	6.67	−4.19
⋯	⋯	⋯	⋯	⋯	2018 May 5	10:42:35.83	125	50	0.45	0.0160	0.362	6.70	−4.15
HD 22049	(3)	5140	0.881	0.501	2017 Oct 31	04:56:33.84	315	48	0.39	0.0204	0.457	6.36	−4.24
⋯	⋯	⋯	⋯	⋯	2018 Feb 24	01:59:09.42	191	49	0.4	0.0214	0.480	6.38	−4.22
HD 30495	(3)	5804	0.632	0.287	2018 Jan 02	07:34:44.74	180	33	0.34	0.0131	0.298	6.51	−4.30
⋯	⋯	⋯	⋯	⋯	2018 Feb 24	02:08:32.46	199	64	0.33	0.0126	0.286	6.48	−4.33
HD 39587	(3)	5930	0.594	0.379	2017 Oct 31	06:09:28.99	134	39	0.41	0.0147	0.333	6.64	−4.21
⋯	⋯	⋯	⋯	⋯	2017 Dec 31	08:19:44.48	243	114	0.4	0.0141	0.319	6.61	−4.23
⋯	⋯	⋯	⋯	⋯	2018 Jan 2	07:24:13.10	281	134	0.41	0.0144	0.325	6.63	−4.22
⋯	⋯	⋯	⋯	⋯	2018 Jan 10	07:32:03.90	64	34	0.41	0.0141	0.320	6.61	−4.23
⋯	⋯	⋯	⋯	⋯	2018 Apr 30	02:02:28.04	231	83	0.41	0.0133	0.302	6.58	−4.26
HD 41593	(3)	5296	0.814	0.467	2017 Dec 10	05:51:26.50	176	58	0.49	0.0230	0.515	6.52	−4.12
⋯	⋯	⋯	⋯	⋯	2017 Dec 31	08:37:11.85	157	55	0.49	0.0233	0.522	6.53	−4.12
⋯	⋯	⋯	⋯	⋯	2018 Jan 2	09:56:19.71	195	41	0.47	0.0228	0.510	6.52	−4.13
⋯	⋯	⋯	⋯	⋯	2018 Jan 5	08:46:02.36	193	65	0.49	0.0233	0.523	6.53	−4.12
⋯	⋯	⋯	⋯	⋯	2018 Feb 1	07:35:33.81	188	54	0.5	0.0240	0.538	6.55	−4.10
⋯	⋯	⋯	⋯	⋯	2018 Apr 30	02:20:09.28	138	37	0.47	0.0217	0.487	6.50	−4.15
HD 72905	(3)	5850	0.618	0.407	2017 Dec 31	11:51:52.03	233	94	0.44	0.0158	0.358	6.64	−4.18
⋯	⋯	⋯	⋯	⋯	2018 Jan 2	12:34:48.19	127	46	0.46	0.0166	0.373	6.67	−4.16
⋯	⋯	⋯	⋯	⋯	2018 Jan 4	07:18:42.04	78	36	0.46	0.0165	0.372	6.66	−4.16
⋯	⋯	⋯	⋯	⋯	2018 Jan 5	10:37:53.08	163	75	0.46	0.0162	0.365	6.65	−4.17

8

Table 3
(Continued)

Star Name	Remarks[a]	$T_{\rm eff}$[b] (K)	$B - V$[b] (mag)	$S_{\rm MWO}$[c]	Date (UT)[d]	Time (UT)[d]	S/N(8542)[e]	S/N(HK)[e]	r_0(8542)	$S_{\rm APO}$	$S_{\rm HK}$	$\log \mathcal{F}_{\rm 2HK}^{+}$ (erg/(cm^2 s))	$\log R_{\rm HK}^{+}$
...	...	...	...	...	2018 Jan 10	07:56:29.39	67	31	0.47	0.0159	0.358	6.64	−4.18
...	...	...	...	...	2018 Feb 1	09:53:35.71	161	67	0.48	0.0171	0.385	6.68	−4.14
...	...	...	...	...	2018 Feb 24	06:46:08.98	129	60	0.48	0.0171	0.386	6.68	−4.14
...	...	...	...	...	2018 Apr 23	06:22:34.92	115	41	0.48	0.0172	0.387	6.69	−4.14
...	...	...	...	...	2018 Apr 30	04:41:56.76	168	68	0.49	0.0177	0.399	6.70	−4.12

Notes.

[a] (1) Active solar-type stars having strong X-ray luminosity, which we have also spectroscopically investigated in Notsu et al. (2017). (2) Bright solar-type (inactive or mildly active) comparison stars also observed in Notsu et al. (2017). (3) Other active solar-type stars for which we have newly started monitoring spectroscopic observations in this study. These stars are also photometrically observed with *TESS* (Ricker et al. 2015) and are included in the target list of *TESS* Guest Investigator programs G011264 (PI: James Davenport) and G011299 (PI: Vladimir Airapetian) (see https://heasarc.gsfc.nasa.gov/docs/tess/approved-programs.html).

[b] Stellar effective temperature ($T_{\rm eff}$) and stellar color ($B - V$). As for the first 15 stars with footnote e or f, $T_{\rm eff}$ values reported in Notsu et al. (2017) are used here, and we newly derive $B - V$ values from the $T_{\rm eff}$ and metallicity values in Notsu et al. (2017), by using Equation (2) of Alonso et al. (1996). As for the latter 13 stars with footnote g, $B - V$ values reported in Table 1 of Isaacson & Fischer (2010) are used here, and $T_{\rm eff}$ values are derived from these $B - V$ values by using Equation (2) of Valenti & Fischer (2005).

[c] Mount Wilson S-index value (Median value of each target) reported in Table 1 of Isaacson & Fischer (2010).

[d] Observation date (Universal Time; format: YYYY-MM-DD) and middle time (Universal Time; format: hh:mm:ss) of each exposure.

[e] S/N of the spectral data around Ca II λ8542 (S/N(8542)) and Ca II H and K λ3934/λ3938 (S/N(HK)).

Table 4
Parameters of the Target Stars Estimated from Our Spectroscopic Data

Star Name	Remarks[a]	Binarity[b]	$T_{\rm eff}$ (K)	log g (cm s^{-2})	$v_{\rm t}$ (km s^{-1})	[Fe/H]	$v \sin i$ (km s^{-1})	$R_{\rm spec}$[c] ($R_\odot$)	R_{Gaia} ($R_\odot$)	$P_{\rm rot}$ (days)	$v_{\rm lc}$ (km s^{-1})	A(Li)
KIC 10532461	⋯	no	5455 ± 20	4.71 ± 0.05	1.14 ± 0.17	−0.14 ± 0.03	4.3 ± 0.3	0.77^{c4}	0.78$^{+0.06}_{-0.05}$	7.14	5.5$^{+0.9}_{-0.7}$	1.98
KIC 11652870	⋯	no	5489 ± 15	4.67 ± 0.04	1.02 ± 0.12	−0.27 ± 0.03	<4	0.76^{c4}	0.78$^{+0.06}_{-0.05}$	8.54	4.6$^{+0.8}_{-0.6}$	2.29
KIC 9139151	⋯	no	6063 ± 18	4.31 ± 0.04	1.13 ± 0.11	0.09 ± 0.03	4.5 ± 0.2	1.24	1.14$^{+0.05}_{-0.05}$	6.15	9.4$^{+1.3}_{-1.0}$	2.76
KIC 4554830	⋯	no	5642 ± 30	4.22 ± 0.07	1.05 ± 0.17	0.35 ± 0.05	<4	1.34	1.44$^{+0.06}_{-0.06}$	7.73	9.4$^{+1.3}_{-1.0}$	<1.0
KIC 4742436	(1)	no	5905 ± 38	3.90 ± 0.09	1.05 ± 0.16	−0.23 ± 0.05	<4	1.83^{c4}	⋯	2.34	39.5$^{+9.1}_{-8.7}$	2.44
KIC 4831454	⋯	no	5637 ± 25	4.65 ± 0.06	1.21 ± 0.17	0.04 ± 0.04	<4	0.88	0.91$^{+0.07}_{-0.06}$	5.19	8.9$^{+1.4}_{-1.1}$	2.79
KIC 8656342	⋯	no	6028 ± 33	4.11 ± 0.07	1.22 ± 0.14	0.02 ± 0.05	4.6 ± 0.2	1.57	1.70$^{+0.07}_{-0.07}$	17.50	4.9$^{+0.7}_{-0.5}$	2.57
KIC 9652680	(2)	no	⋯	⋯	⋯	⋯	38.2 ± 0.1	0.88	1.09$^{+0.08}_{-0.07}$	1.47	37.5$^{+5.9}_{-4.3}$	3.43
KIC 6777146	⋯	no	6158 ± 38	4.39 ± 0.08	1.37 ± 0.19	−0.02 ± 0.06	7.6 ± 0.1	1.11	1.60$^{+0.12}_{-0.11}$	7.21	11.2$^{+1.8}_{-1.3}$	2.57
KIC 8508009	⋯	no	6301 ± 35	4.51 ± 0.07	1.13 ± 0.17	0.18 ± 0.05	4.5 ± 0.2	1.19^{c4}	1.15$^{+0.09}_{-0.08}$	2.95	19.7$^{+3.1}_{-2.3}$	3.35
KIC 11610797	⋯	no	6209 ± 43	4.41 ± 0.10	1.70 ± 0.20	0.26 ± 0.05	23.0 ± 0.1	1.24	1.17$^{+0.05}_{-0.05}$	1.62	36.5$^{+4.9}_{-3.7}$	3.62
KIC 11253827	⋯	no	5686 ± 23	4.76 ± 0.06	1.07 ± 0.22	0.19 ± 0.05	<4	0.95^{c4}	0.90$^{+0.04}_{-0.04}$	13.40	3.4$^{+0.5}_{-0.4}$	1.34
KIC 6291837	⋯	no	6270 ± 48	4.29 ± 0.09	1.48 ± 0.23	0.00 ± 0.07	7.9 ± 0.1	1.30	1.42$^{+0.07}_{-0.07}$	14.30	5.0$^{+0.8}_{-0.6}$	2.71
KIC 11551430A	(1), (3)	RV(+VB)	5589 ± 40	3.95 ± 0.10	1.88 ± 0.25	−0.20 ± 0.07	18.8 ± 0.1	1.81	⋯	4.26	21.4$^{+5.0}_{-4.8}$	2.33
KIC 11551430B	(3)	(VB)	5943 ± 98	5.44 ± 0.27	0.81 ± 0.50	0.22 ± 0.10	<4	1.08^{c4}	⋯	⋯	⋯	<2.3
KIC 4543412	(4)	RV	5655 ± 73	4.92 ± 0.18	1.95 ± 0.38	0.07 ± 0.10	18.3 ± 0.1	0.97^{c4}	0.96$^{+0.07}_{-0.06}$	2.16	22.5$^{+3.5}_{-2.6}$	<2.0
KIC 11128041	(5)	SB2+RV	⋯	⋯	⋯	⋯	⋯	⋯	1.21$^{+0.09}_{-0.08}$	7.36	8.3$^{+1.3}_{-1.0}$	⋯
KIC 10338279	(1), (5)	SB2	⋯	⋯	⋯	⋯	⋯	⋯	⋯	6.53	⋯	⋯
KIC 7093428	(1), (6)	VB	6364 ± 60	4.02 ± 0.01	1.45 ± 0.25	−0.02 ± 0.07	5.1 ± 0.2	1.90	⋯	0.51	187.8$^{+43.0}_{-41.3}$	<2.3

Notes.

[a] (1) As for these four stars (KIC 4742436, KIC 11551430A, KIC 10338279, and KIC 7093428), there are no stellar radius values $R_{\rm Gaia}$ reported in Berger et al. (2018) (*Gaia*-DR2). For these four stars, $R_{\rm spec}$ (stellar radius estimated from $T_{\rm eff}$, log g, and [Fe/H] in Appendix A.3) values are used to calculate $v_{\rm lc}$ values, while $R_{\rm Gaia}$ values are used for the other stars. (2) We cannot estimate atmospheric parameters ($T_{\rm eff}$, log g, $v_{\rm t}$, and [Fe/H]) of KIC 9652680 since the rotational velocity of this star is large ($\gtrsim$30 km s^{-1}) and the spectral lines of these stars are too wide to estimate the atmospheric parameters in our way using equivalent widths of Fe I/II lines (see Appendix A.2 for details). When we estimate $v \sin i$, $R_{\rm spec}$, and A(Li) values listed in this table, $T_{\rm eff,DR25}$, (log g)$_{\rm DR25}$, and [Fe/H]$_{\rm DR25}$ (DR25-KSPC values) in Table 1 are used, and microturbulence velocity ($v_{\rm t}$) is assumed to be 1 km s^{-1}, as also done in Notsu et al. (2015a). (3) KIC 11551430 is found to be a visual binary (KIC 11551430A and KIC 1551430B), as described in Appendix A.1. We took spectra of each component of the visual binary separately and measured stellar parameters of each of them. (4) KIC 4543412 shows RV changes but has single-lined profiles. After shifting the wavelength value of each spectrum to the laboratory frame on the basis of the RV value of each observation, we added up these shifted spectra to one co-added spectrum, as described in Appendix A.1. We measured stellar parameters by using this combined spectrum. (5) We do not measure any parameters from the spectra of KIC 11128041 and KIC 10338279 since these stars show double-lined profiles. (6) As described in Appendix A.1, KIC 7093428 has two fainter companion stars, and pixel data analyses suggest that flares occur on these companion stars. Since companion stars are faint, here we only measured stellar parameters of the main (brightest) star for reference, though we do not use these values in the main discussion of this paper.

[b] Same as in footnote a of Table 1. See also Appendix A.1.

[c] As for the six stars with the marks $c1$, $c2$, $c3$, or $c4$, there are no suitable PARSEC isochrones within their original error range of $T_{\rm eff}$ and log g values ($\Delta T_{\rm eff}$ and Δlog g), as mentioned in Appendix A.3. We then enlarge error ranges to find the appropriate isochrone values. As for the three stars with $c1$, we take into account $2\Delta T_{\rm eff}$ and 2Δlog g. As for the stars with $c2$, $c3$, $c4$, we take into account the error ranges "$2\Delta T_{\rm eff}$ and 3Δlog g," "$2\Delta T_{\rm eff}$ and 4Δlog g," and "$2\Delta T_{\rm eff}$ and 5Δlog g," respectively.

Table 5
Activity Indicators of the Target Stars

Star Name	Remarks[a]	Binarity[b]	$\langle$BVAmp$\rangle$[c] (%)	r_0(8542)	r_0(Hα)	S_{HK}	$\log \mathcal{F}'_{HK}$ (erg/(cm^2 s))	$\log R'_{HK}$	$\log \mathcal{F}^+_{HK}$ (erg/(cm^2 s))	$\log R^+_{HK}$
KIC 10532461	⋯	no	$1.55^{+0.73}_{-0.74}$	0.51	0.33	0.465	6.70	−4.00	6.66	−4.04
KIC 11652870	⋯	no	$0.93^{+0.23}_{-0.25}$	0.46	0.32	0.413	6.68	−4.03	6.64	−4.07
KIC 9139151	⋯	no	$0.06^{+0.07}_{-0.02}$	0.22	0.19	0.177	6.40	−4.49	6.27	−4.61
KIC 4554830	⋯	no	$0.03^{+0.01}_{-0.01}$	0.19	0.18	0.164	6.11	−4.65	5.93	−4.83
KIC 4742436	⋯	no	$0.46^{+0.43}_{-0.24}$	0.28	0.30	0.216	6.52	−4.32	6.43	−4.41
KIC 4831454	⋯	no	$0.91^{+1.27}_{-0.50}$	0.53	0.32	0.480	6.77	−3.99	6.73	−4.02
KIC 8656342	⋯	no	$0.03^{+0.01}_{-0.01}$	0.22	0.20	0.175	6.39	−4.48	6.26	−4.61
KIC 9652680	⋯	no	$4.72^{+1.32}_{-2.06}$	0.65	0.51	0.509	6.95	−3.87	6.92	−3.90
KIC 6777146	⋯	no	$0.09^{+0.05}_{-0.03}$	0.26	0.23	0.179	6.47	−4.44	6.35	−4.56
KIC 8508009	⋯	no	$0.28^{+0.16}_{-0.09}$	0.38	0.28	0.278	6.74	−4.21	6.69	−4.27
KIC 11610797	⋯	no	$2.44^{+0.66}_{-0.95}$	0.63	0.47	0.498	6.99	−3.93	6.96	−3.96
KIC 11253827	⋯	no	$1.59^{+0.84}_{-0.83}$	0.39	0.26	0.351	6.61	−4.17	6.55	−4.22
KIC 6291837	⋯	no	$0.08^{+0.02}_{-0.02}$	0.26	0.22	0.195	6.56	−4.38	6.47	−4.47
KIC 11551430A	(1)	RV(+VB)	$2.65^{+1.42}_{-1.13}$	0.83	0.69	0.813	7.04	−3.70	7.02	−3.72
KIC 11551430B	(1)	VB	⋯	0.24	0.20	0.462	6.85	−3.99	6.82	−4.03
KIC 4543412	(2)	RV	$4.77^{+2.02}_{-2.25}$	0.80	0.62	0.844	7.04	−3.72	7.02	−3.74
KIC 11128041	(3)	SB2+RV	$0.48^{+0.28}_{-0.21}$	⋯	⋯	⋯	⋯	⋯	⋯	⋯
KIC 10338279	(3)	SB2	$1.29^{+0.35}_{-0.40}$	⋯	⋯	⋯	⋯	⋯	⋯	⋯
KIC 7093428	(4)	VB	$0.13^{+0.04}_{-0.06}$	0.22	0.19	0.150	6.44	−4.53	6.30	−4.67

Notes.

[a] (1) KIC 11551430 is found to be a visual binary (KIC 11551430A and KIC 11551430B), as described in Appendix A.1. We took spectra of each component of the visual binary separately and measured stellar parameters of each of them. (2) KIC 4543412 shows RV changes but has single-lined profiles. After shifting the wavelength value of each spectrum to the laboratory frame on the basis of the RV value of each observation, we added up these shifted spectra to one co-added spectrum, as described in Appendix A.1. We measured stellar parameters by using this combined spectrum. (3) We do not measure any parameters from the spectra of KIC 11128041 and KIC 10338279 since these stars show double-lined profile. (4) As described in Appendix A.1, KIC 7093428 has two fainter companion stars, and pixel data analyses suggest that flares occur on these companion stars. Since companion stars are faint, here we only measured stellar parameters of the main (brightest) star for reference, though we do not use these values in the main discussion of this paper.

[b] Same as in footnote a of Table 1. See also Appendix A.1.

[c] The amplitude of the brightness variation. This value is calculated by taking the average of the amplitude value of each quarter (Q2–Q16) of data, as also done in Notsu et al. (2015b). We did not use Q0, Q1, and Q17 data since the duration of these three quarters is short (30 days) compared to those of the other 15 quarters (∼90 days) (Thompson et al. 2015). The errors of $\langle$BVAmp$\rangle$ correspond to the maximum and minimum of the amplitude values of all Quarter (Q2–Q16) data.

Table 6
Number of the "Single" and "Binary" Stars

Source	Total	Single	Binary[a]
APO 3.5 m (this study)	18	13	5(2)
Subaru/HDS (Notsu et al. 2015a)	50	34	16(4)
Total	64[b]	43[b]	21(6)

Notes.

[a] Numbers in parentheses correspond to visual binary stars.

[b] Four single stars (KIC 4742436, KIC 4831454, KIC 9652680, and KIC 11610797) were observed in both studies (APO 3.5 m and Subaru/HDS).

stars, though the stars with $\log g \lesssim 4.0$ are possibly subgiant G-type stars (for discussions on evolutionary state of the target stars, see also Section 5.1). Compared with the 34 single target superflare stars that we observed in Notsu et al. (2015a), the target stars tend to have a bit hotter T_{eff} values, and most of them are "solar-analog" stars (early-type G-type main-sequence stars). No clear "metal-rich" or "metal-poor" stars are included in the target stars of this observation.

4.3. Rotational Velocity

As described above, we report the values of projected rotational velocity $v \sin i$, stellar radius R (R_{Gaia} and R_{spec}), and

rotation period P_{rot} from the brightness variation of the single target superflare stars (listed in Table 4). Using the R and P_{rot} values, we can estimate the rotational velocity (v_{lc}):

$$v_{lc} = \frac{2\pi R}{P_{rot}},\qquad(1)$$

as also described in Section 4 of Notsu et al. (2015b). As for the R values, we used $R = R_{Gaia}$ as a first priority and $R = R_{spec}$ only for the stars without R_{Gaia} values. As for the errors of v_{lc}, we took the root sum squares of the two types of errors from R (see the descriptions in Appendix A.3) and P_{rot}. We here assume that the possible errors of P_{rot} are about 10%, as done in Notsu et al. (2015b). In this assumption, we very roughly consider typical possible differences between equatorial rotation period and the measured period caused by the solar-like differential rotations. For example, the solar latitudinal differential rotation has a magnitude of 11% of the average rate from equator to midlatitudes ($\approx$45° latitude; see Benomar et al. 2018). We must note here that the differences can be much larger if we observe starspots near the pole region, and there can be solar-type stars with much larger differential rotation magnitudes (Benomar et al. 2018). Moreover, it is sometimes hard to distinguish the correct P_{rot} values with $1/n \times P_{rot}$ ($n = 2, 3, ...$) values in the periodogram, especially when there
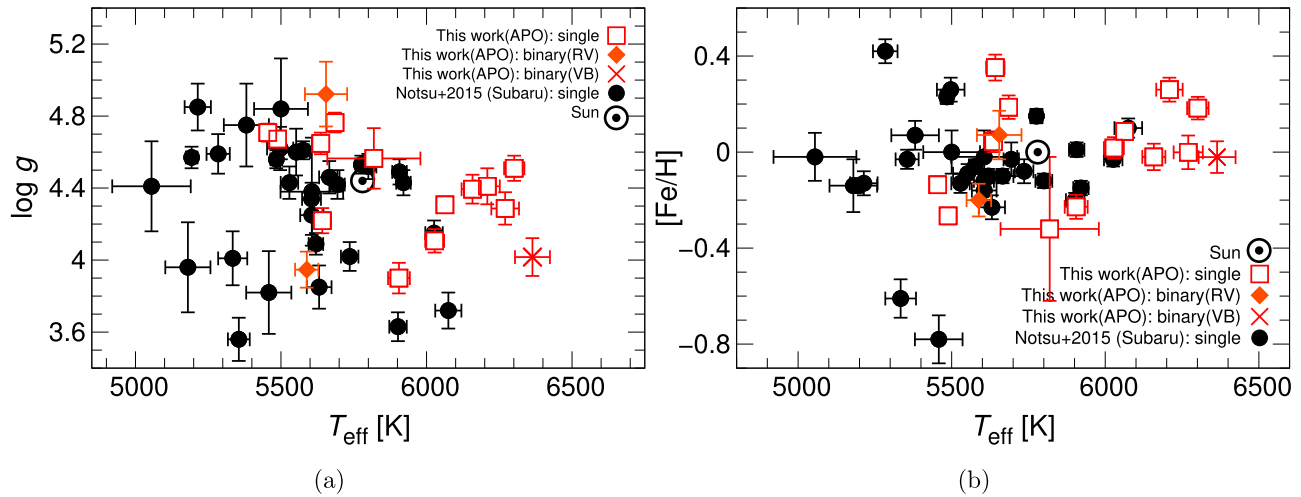
Figure 1. Temperature (T_{eff}), surface gravity (log g), and metallicity ([Fe/H]), estimated from spectroscopic observations. The red open square points are the target superflare stars classified as single stars in Appendix A.1, and the orange diamonds correspond to the spectra of binary superflare stars that do not show any double-lined profiles (KIC 11551430A and KIC 4543412). A visual binary superflare star KIC 7093428 (see Section 4.1 for details) is plotted for reference with the red cross. The single superflare stars that we investigated using the Subaru telescope (Notsu et al. 2015a), excluding the four stars also investigated in this study (see footnote f of Table 1), are plotted with the black circles. The circled dot corresponds to the Sun.

are several starspots on the surface of the stars (see Figure 2 of Notsu et al. 2013b). As a result, we must note here with caution that P_{rot} can have much larger error values, though the detailed investigations of each error value are beyond the scope of the overall discussions of $v \sin i$ versus v_{lc} in Figure 2. The resultant values of v_{lc} are listed in Table 4.

We then plot $v \sin i$ as a function of v_{lc} in Figure 2. Not only the target superflare stars of this study (13 "single" stars and two binary stars categorized as "RV" and "VB" in Appendix A.1) but also the 34 single superflare stars that we have observed in Notsu et al. (2015b) are plotted for reference. The v_{lc} values of the latter 34 superflare stars are updated from the original ones in Notsu et al. (2015b). We newly recalculated v_{lc} (see Equation (1)) of each target star by using the R_{Gaia} value if the star has an R_{Gaia} value reported in Berger et al. (2018).

In Figure 2, $v \sin i$ tends to be smaller than v_{lc}, and such differences should be explained by the inclination angle effect, as mentioned in the previous studies (e.g., Hirano et al. 2012; Notsu et al. 2015b). On the basis of $v \sin i$ and v_{lc}, the stellar inclination angle (i) can be estimated by using the following relation:

$$i = \arcsin\left(\frac{v \sin i}{v_{\text{lc}}}\right). \quad (2)$$

In Figure 2, we also show four lines indicating $i = 90°(v \sin i = v_{\text{lc}})$, $i = 60°$, $i = 30°$, and $i = 10°$. First of all, almost all the stars (except for KIC 6291837, with $v \sin i \sim 7.9\,\text{km s}^{-1}$ and $v_{\text{lc}} \sim 5.0\,\text{km s}^{-1}$) in Figure 2, the relation "$v \sin i \lesssim v_{\text{lc}}$" is satisfied. This is consistent with the assumption that the brightness variation is caused by the rotation since the inclination angle effect can cause this relation "$v \sin i \lesssim v_{\text{lc}}$" if v_{lc} really corresponds to the rotation velocity (i.e., $v = v_{\text{lc}}$). This is also supported by the fact that the distribution of the data points in Figure 2 is not random, but is concentrated between the lines of $i = 90°$ and $i = 60°$. The distribution is expected to be much more random if the brightness variations have no relations with the stellar rotation.
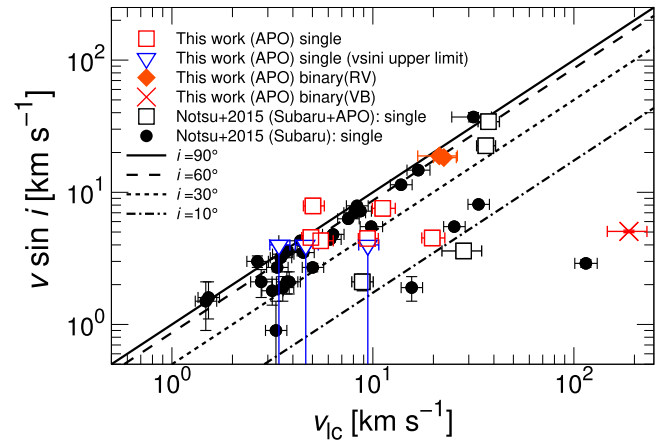
Figure 2. Projected rotational velocity ($v \sin i$) vs. the stellar rotational velocity (v_{lc}) estimated from the period of the brightness variation (P_{rot}) and stellar radius (R). The solid line represents the case that our line of sight is perpendicular to the stellar rotation axis ($i = 90°$, $v \sin i = v_{\text{lc}}$). We also plot three different lines, which correspond to smaller inclination angles ($i = 60°$, $30°$, $10°$). The open red squares and blue downward-pointing triangles are the target superflare stars classified as single stars in Appendix A.1, and the latter points (blue triangles) correspond to the slowly rotating stars only with the upper-limit values of $v \sin i$ ($v \sin i < 4\,\text{km s}^{-1}$; see Appendix A.4 for details). The orange diamonds correspond to the spectra of binary superflare stars that do not show any double-lined profiles (KIC 11551430A and KIC 4543412). Visual binary superflare star KIC 7093428 (see Section 4.1 for details) is plotted for reference with the red cross. The single superflare stars that we investigated using the Subaru telescope (Notsu et al. 2015b) are plotted with black circles and black open squares. As for the four stars (KIC 4742436, KIC 4831454, KIC 9652680, and KIC 11610797) investigated both in Notsu et al. (2015b) and in this study (see footnote f of Table 1), the values in Notsu et al. (2015b; Subaru) are only plotted in this table (black open squares), and the values from APO data are not used. This is because the wavelength resolution (i.e., accuracy of $v \sin i$ estimation) of Subaru/HDS data is higher than that of APO data (see Appendix A.4).

In addition, stars that are distributed in the lower right side of Figure 2 are expected to have small inclination angles and to be nearly pole-on stars. Later in Section 5.2, we see these inclination angle effects from another point of view with the scatter plot of flare energy and starspot size.
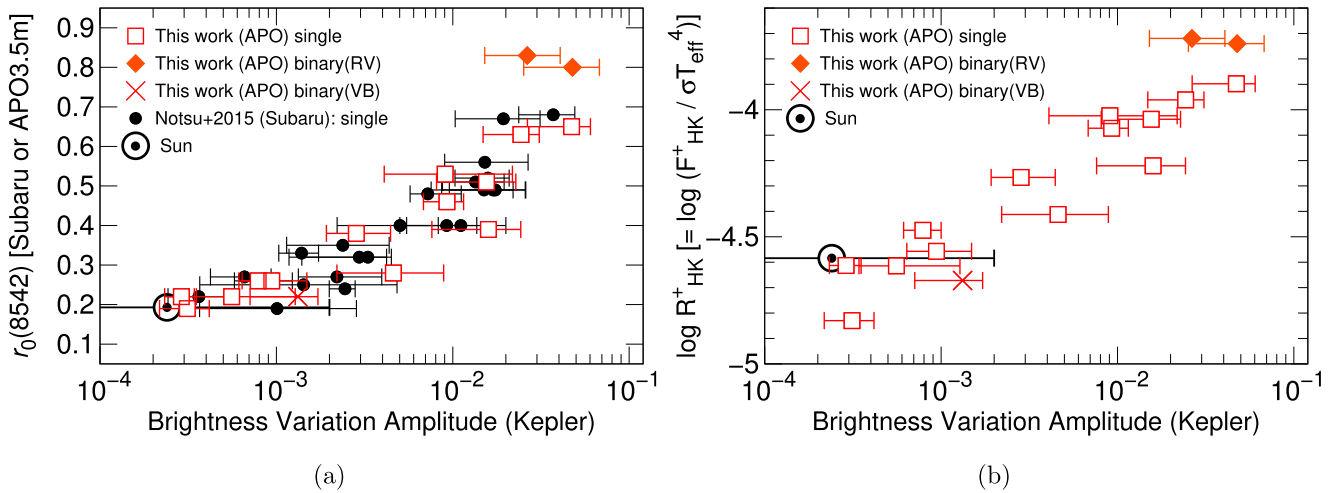
Figure 3. (a) $r_0(8542)$ (the normalized intensity at the center of Ca II $\lambda8542$ line) vs. $\langle$BVAmp$\rangle$ (the amplitude of stellar brightness variation of *Kepler* data). (b) Ca II H and K activity index $\log \mathcal{R}_{HK}^+$ ($=\mathcal{F}_{HK}^+/\sigma T_{eff}^4$) vs. $\langle$BVAmp$\rangle$. The red open squares are the target superflare stars classified as single stars in Appendix A.1, and the orange diamonds correspond to the spectra of binary superflare stars that do not show any double-lined profiles (KIC 11551430A and KIC 4543412). Visual binary superflare star KIC 7093428 (see Section 4.1 for details) is plotted for reference with the red cross. Only in panel (a), the single superflare stars that we investigated using the Subaru telescope (Notsu et al. 2015b), excluding the four stars also investigated in this study (see footnote f of Table 1), are also plotted with black circles. The solar value is plotted by using a circled dot. The difference of Ca II index values between solar maximum and solar minimum is no larger than the size of this point (Lockwood et al. 2007).

Summarizing the results in this section, we can remark that rotation velocity values from spectroscopic results ($v \sin i$) and those from *Kepler* brightness variation (v_{lc}) are consistent, and this supports that the brightness variation of superflare stars is caused by the rotation. This remark was already suggested in Notsu et al. (2015b), but the conclusions are more strongly confirmed by the new spectroscopic observations and *Gaia*-DR2 stellar radius (R_{Gaia}) values.

4.4. Stellar Chromospheric Activity and Starspots of Superflare Stars

We measured the core intensity and flux values of chromospheric lines (Ca II $\lambda8542$, Hα $\lambda6563$, and Ca II H and K lines) in Appendices A.5–A.7. These lines have been widely used for investigating stellar chromospheric activities (e.g., Wilson 1978; Linsky et al. 1979a; Noyes et al. 1984; Duncan et al. 1991; Baliunas et al. 1995; Hall 2008) and are good indicators of stellar average magnetic fields (e.g., Schrijver et al. 1989; Notsu et al. 2015b). Only the Ca II $\lambda8542$ line is mainly used in our previous studies using the Subaru telescope (Notsu et al. 2013a, 2015b; Nogami et al. 2014). In this study, Ca II H and K lines are used with high-dispersion spectra for the first time in our series of studies of the *Kepler* solar-type superflare stars.[18]

In Figure 3, we compare the Ca II $\lambda8542$ and Ca II H and K index values ($r_0(8542)$ and $\log \mathcal{R}_{HK}^+$) with the amplitude of the brightness variation of *Kepler* data ($\langle$BVAmp$\rangle$). The $r_0(8542)$ index is the normalized intensity at the center of the Ca II $\lambda8542$ line (see Section A.5 for details). The $\log R_{HK}^+$ index is a universal and "pure" Ca II H and K activity indicator introduced by Mittag et al. (2013) and is defined as $\mathcal{R}_{HK}^+ = \mathcal{F}_{HK}^+/\sigma T_{eff}^4$ (Equation (18)), where $\mathcal{F}_{HK}^+$ is the Ca II H and K surface flux (unit: erg cm^{-2} s^{-1}) with photospheric and "basal" flux contributions removed (see Appendix A.7 for

details). As described in Figure 30 in Appendix A.7, this $\log R_{HK}^+$ index has a good correlation with the $r_0(8542)$ index, and $\log R_{HK}^+$ can be more sensitive to the difference in the lower activity level region compared with $r_0(8542)$. $\langle$BVAmp$\rangle$ values are calculated by taking the average of the amplitude value of each Quarter (Q2–Q16) data, as we have done in Notsu et al. (2015b). The resultant values of $\langle$BVAmp$\rangle$ of the target stars of our APO 3.5 m observations are listed in Table 5. In Figure 3, we also plot solar values as a reference, as done in Notsu et al. (2015b), and we can see that, as for most of the target superflare stars, Ca II $\lambda8542$ and Ca II H and K index values are higher than the solar values. This suggests that these superflare stars have higher chromospheric activities compared with the Sun.

More importantly, there is a rough positive correlation between Ca II index values and $\langle$BVAmp$\rangle$ in Figure 3. Assuming that the brightness variation of superflare stars is caused by the rotation of a star with starspots, the brightness variation amplitude ($\langle$BVAmp$\rangle$) corresponds to the starspot coverage of these stars. As mentioned above, Ca II index values are good indicators of stellar average magnetic field (or total magnetic flux). Then, we can remark that there is a rough positive correlation between the starspot coverage from *Kepler* photometric data and the stellar average magnetic field from spectroscopic data. All the target stars expected to have large starspots on the basis of their large amplitude of the brightness variation show strong average magnetic field compared with the Sun. In other words, our assumption that the amplitude of the brightness variation corresponds to the spot coverage is supported, since the average magnetic field is considered to be caused by the existence of large starspots. These results have already been confirmed in Notsu et al. (2015b) with the Ca II $\lambda8542$ line, but in this study we confirmed the same conclusion with the following two updates: (i) larger number of stars with Ca II $\lambda8542$ line data (Figure 3(a)), and (ii) analyses using Ca II H and K lines (Figure 3(b)).

---

[18] We note here that Karoff et al. (2016) already investigated Ca II H and K line intensity and flux values of superflare stars with LAMOST "low-resolution" spectra.
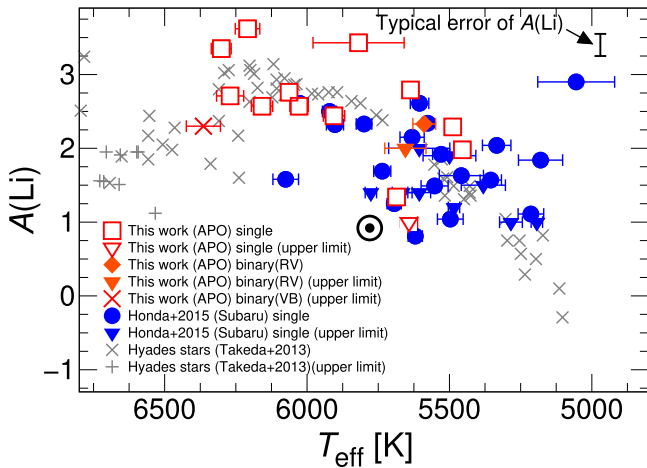
Figure 4. A(Li) vs. $T_{\rm eff}$ of the target superflare stars in comparison with the stars in the Hyades. The age of Hyades is 6.25×10^8 yr (e.g., Perryman et al. 1998). The red open squares/triangles are the target superflare stars classified as single stars in Appendix A.1, and the orange diamonds/triangles correspond to the spectra of binary superflare stars that do not show any double-lined profiles (KIC 11551430A and KIC 4543412). A visual binary superflare star KIC 7093428 (see Section 4.1 for details) is plotted for reference with the red cross. The single superflare stars that we investigated using the Subaru telescope (Notsu et al. 2015b), excluding the four stars also investigated in this study (see footnote f of Table 1), are also plotted with blue circles/triangles. Among the above symbols, the triangles and the cross correspond to the upper-limit values of A(Li) for the unmeasurable cases. We plot the data of the stars in Hyades reported by Takeda et al. (2013) with gray crosses and plus signs, and the plus signs correspond to the upper-limit values of A(Li) for the unmeasurable cases. The solar value is also plotted with a circled dot for reference. The typical error value of A(Li) ($\sim$0.15 dex) mentioned in Appendix A.8 is shown with the error bar in the upper right of this figure.

4.5. Li Abundances

We also estimated Li abundances A(Li) of the target superflare stars in Appendix A.8. Li abundance is known to be a clue for investigating the stellar age of solar-type stars (e.g., Skumanich 1972; Takeda et al. 2010, 2013; Honda et al. 2015; Notsu et al. 2017). The Li depletion is seen in the stars with $T_{\rm eff} \lesssim 5500$ K, while the stars with $T_{\rm eff} \gtrsim 6000$ K show no Li depletion. This is because as the star becomes cooler, the convection zone in the stellar atmosphere evolves and the Li is transported to a deeper hotter zone, where Li is easily destroyed (p, α reactions: ^{7}Li, $T \geqslant 2.5 \times 10^6$ K; ^{6}Li, $T \geqslant 2.0 \times 10^6$ K). The depletion of Li in the stellar surface caused by convective mixing increases as time passes, and we can remark that young stars tend to have high A(Li) values.

In Figure 4, we plot A(Li) as a function of $T_{\rm eff}$ of the superflare stars in comparison with the ordinary stars in the Hyades (taken from Takeda et al. 2013). Some of the superflare stars show high Li compared with the stars in the Hyades (Figure 4), and such stars are suggested to be younger than the Hyades. The age of the Hyades is estimated to be 6.25×10^8 yr (e.g., Perryman et al. 1998). It is reasonable that such young stars tend to have high activity levels and produce superflares. However, more than 10 target stars do not show higher A(Li) values compared with the Hyades, and a few of them are as low as the solar value. These results suggest that superflare stars include many young stars but also include old stars like our Sun, as also suggested in Honda et al. (2015).

5. Statistical Properties of *Kepler* Solar-type Superflare Stars Incorporating *Gaia*-DR2 Data

5.1. Evolutionary State Classifications of Superflare Stars

In this section, we investigate again the statistical discussions of *Kepler* solar-type superflare stars in our previous studies (Maehara et al. 2012, 2015, 2017; Notsu et al. 2013b; Shibayama et al. 2013), by incorporating *Gaia*-DR2 stellar radius estimates (reported in Berger et al. 2018) and the results of our spectroscopic observations (Subaru and APO 3.5 m observations). In these previous studies, we reported 1547 superflare events on 279 solar-type (G-type main-sequence) stars from *Kepler* 30-minute (long) time-cadence data (Shibayama et al. 2013) and 189 superflares on 23 solar-type stars from *Kepler* 1-minute (short) time-cadence data (Maehara et al. 2015; line 1 of Tables 7 and 8). As also used in Appendix A.3, Berger et al. (2018) reported the catalog of the 177,911 *Kepler* stars with the stellar radius estimates (R_{Gaia}) estimated from *Gaia*-DR2 parallax values. A total of 245 out of the 279 solar-type superflare stars in Shibayama et al. (2013) and 18 of the 23 stars in Maehara et al. (2015) have R_{Gaia} values in this *Gaia*-DR2 catalog, respectively (Line 2 of Tables 7 and 8).

We plot these superflare stars on the stellar radius (R) versus $T_{\rm eff}$ diagram in Figures 5(a) and (b). In these figures, all the *Kepler* stars reported in Berger et al. (2018) are also plotted for reference with the evolutionary state classifications (main sequence (MS)/subgiants/red giants/cool main-sequence binaries). In Figure 5(a), among the 245 stars found as solar-type superflare stars from *Kepler* 30-minute time-cadence data in Shibayama et al. (2013), 136 stars (55.5%) are classified as main-sequence stars, while 108 stars (44.1%) are classified as subgiants and only one star (KIC 4633721) as a red giant (lines (3)–(5) of Table 7). Originally in Shibayama et al. (2013), we used the $T_{\rm eff}$ and log g values in the initial *Kepler* Input Catalog (KIC; Brown et al. 2011) and selected solar-type (G-type main-sequence) stars with the definition of 5100 K $\leqslant T_{\rm eff} \leqslant$ 6000 K and log $g \geqslant 4.0$. $T_{\rm eff}$ and log g values in the initial KIC have large error values of $\pm$200 K and 0.4 dex, respectively (Brown et al. 2011), and the reliability of each value can be low. In Figure 5(a), in addition to the updated stellar radius R_{Gaia} from *Gaia*-DR2 data, $T_{\rm eff}$ values are also updated with the latest DR25-KSPC (Mathur et al. 2017), which incorporates the revised method of $T_{\rm eff}$ estimation (see Pinsonneault et al. 2012). As a result, a large fraction (more than 40%) of the stars that were originally identified as solar-type superflare stars in Shibayama et al. (2013) are now classified as subgiant or red giant stars.

In Figure 5(b), among the 18 stars found as solar-type superflare stars from *Kepler* 1-minute time-cadence data in Maehara et al. (2015), 13 stars are classified as main-sequence stars, while 5 stars are classified as subgiant stars (lines (3)–(5) of Table 8). In the case of these 18 stars, the revised KIC catalog (Huber et al. 2014) was used when we selected solar-type stars in Maehara et al. (2015), and it is possible that the errors of $T_{\rm eff}$ were somewhat smaller, compared with the case of the stars from Shibayama et al. (2013) in Figure 5(a).

In Figure 5(c), we plot 50 superflare stars found from *Kepler* 30-minute cadence data that we have spectroscopically observed using the Subaru telescope (Notsu et al. 2015a, 2015b). As for the radius value in the vertical axis of these two figures, the R_{Gaia}

Table 7
Number of Solar-type Superflare Stars ($N_{\rm star}$) and Superflares on These Stars ($N_{\rm flare}$) Found from *Kepler* 30-minute Time-cadence Data (See Figures 5(a) and 6)

	$N_{\rm star}$	$N_{\rm flare}$
(1) Original data (Shibayama et al. 2013)	279	1547
(2) Stars having R_{Gaia} values (Berger et al. 2018) among (1)	245	1402
(3) Stars identified as main sequence among (2) (see Figure 5(a))	136 (55.5%)	496
(4) Stars identified as subgiants among (2) (see Figure 5(a))	108 (44.1%)	905
(5) Stars identified as red giants among (2) (see Figure 5(a))	1 (0.4%)	1
(6) Stars with $T_{\rm eff,DR25}$ = 5100–6000 K among (3)	106	419
(7) Stars that were originally early K dwarfs in Candelaresi et al. (2014) but are newly identified as solar-type stars with $T_{\rm eff,DR25}$ and R_{Gaia}	36	178
(8) (6)+(7)	142	597
(9) Stars having $\Delta F/F$ values in McQuillan et al. (2014) among (8)	113	527

Table 8
Number of Solar-type Superflare Stars ($N_{\rm star}$) and Superflares on These Stars ($N_{\rm flare}$) Found from *Kepler* 1-minute Time-cadence Data (See Figures 5(b) and 6)

	$N_{\rm star}$	$N_{\rm flare}$
(1) Original data (Maehara et al. 2015)	23	187
(2) Stars having R_{Gaia} values (Berger et al. 2018) among (1)	18	68
(3) Stars identified as main sequence among (2) (see Figure 5(b))	13 (2, 2)[a]	55 (15, 9)[a]
(4) Stars identified as subgiants among (2) (see Figure 5(b))	5 (0, 2)[a]	13 (0, 9)[a]
(5) Stars identified as red giants among (2) (see Figure 5(b))	0	0
(6) Stars with $T_{\rm eff,DR25}$ = 5100–6000 K among (3)	10	51
(7) Stars having $\Delta F/F$ values in McQuillan et al. (2014) among (6)	8	48

Note.
[a] Numbers in parentheses show the stars identified as binary and the stars for which we have not conducted spectroscopic observations because they are too faint, respectively, on the basis of our APO 3.5 m spectroscopic observations in this study (see also Figure 5(d) and Table 1).

value is used if it exists. If the star has no R_{Gaia} value in Berger et al. (2018), $R_{\rm spec}$ values (in Table 4 of Notsu et al. 2015a) are used for single stars and $R_{\rm DR25}$ values (from DR25-KSPC in the above) are used for binary stars. As for the temperature value in the horizontal axis, $T_{\rm eff}$ values estimated from spectroscopic data (in Table 4 of Notsu et al. 2015a) are used for single stars, while $T_{\rm eff,DR25}$ values are used for binary stars. As a result, 24 stars are classified as main sequence, while the remaining 10 stars[19] are classified as subgiants, among all 34 "single" target stars. Among the 16 "binary" target stars, only 5 stars are classified as main-sequence stars, while the remaining 11 stars[20] are classified as subgiants.

In Figure 5(d), we plot the target stars of the APO 3.5 m spectroscopic observation of this study, which are equal to all 23 superflare stars found from *Kepler* 1-minute cadence data (Maehara et al. 2015). The radius and temperature values in the vertical and horizontal axes are plotted in the basically same way as in Figure 5(c), but $R_{\rm spec}$ values are used for "RV" binary stars if the stars have no R_{Gaia} values, and $T_{\rm eff}$ estimated from spectroscopic data are used for all "RV" binary stars. As a result, 9 stars are classified as main sequence, while 4 stars[21] are classified as subgiants, among all 13 "single target stars. Among the five "binary" target stars, three stars are classified as main sequence, while two stars[22] are classified as subgiants. Moreover, among

the remaining five stars for which we did not get spectroscopic data with enough S/N in this study (see Section 2),[23] three stars are classified as main sequence, while two stars[24] are classified as subgiants. In the following sections, we update statistical studies by using the data of the stars that we can newly classify as solar-type (G-type main-sequence) stars.

5.2. Starspot Size and Energy of Superflares

Most superflare stars show large-amplitude brightness variations, and they suggest that the surfaces of superflare stars are covered by large starspots (see Section 4.4). Figure 6 shows the scatter plot of flare energy ($E_{\rm flare}$) as a function of the spot group area ($A_{\rm spot}$). The values of solar flares in Figure 6 are the same as those in our previous studies (Notsu et al. 2013b; Shibata et al. 2013; Maehara et al. 2015). We estimate bolometric energies (white-light flare [WLF] energies) of solar flares from *GOES* soft X-ray (SXR) flux values. We use the relation that WLF energy ($E_{\rm WL}$) is proportional to SXR flux ($F_{\rm SXR}$), $E_{\rm WL} \propto F_{\rm SXR}$, on the basis of the results and detailed descriptions in Section 4.1 of Namekata et al. (2017). This relation is supported by the observational comparisons between WL and SXR data during flares (e.g., Figure 4 of Namekata et al. 2017), which are related to the well-known relation between hard X-ray flux and SXR flux during a flare ("Neupert effect"; Neupert 1968). As a result, we here assume that bolometric energies of B-, C-, M-, X-, and X10-class solar flares are 10^{28}, 10^{29}, 10^{30}, 10^{31}, and 10^{32} erg, respectively.

[19] KIC 3626094, KIC 6503434, KIC 7420545, KIC 8547383, KIC 9412514, KIC 9459362, KIC 10252382, KIC 10528093, KIC 11455711, and KIC 11764567.
[20] KIC 4045215, KIC 4138557, KIC 7264976, KIC 7902097, KIC 8479655, KIC 9653110, KIC 9764192, KIC 9764489, KIC 10120296, KIC 10453475, and KIC 11560431.
[21] KIC 4554830, KIC 4742436, KIC 6777146, and KIC 8656342.
[22] KIC 11551430A and KIC 7093428.

[23] As also done for "SB2" and "VB" binary stars, $R_{\rm gaia}$ and $T_{\rm eff,DR25}$ values are used if $R_{\rm gaia}$ exists. If not, $T_{\rm eff,DR25}$ and $T_{\rm eff,DR25}$ values are used.
[24] KIC 10528093 and KIC 10745663.

In Figure 6, A_{spot} of superflare stars were estimated from the normalized amplitude of light variations ($\Delta F/F$) by using the following equation (Notsu et al. 2013b; Shibata et al. 2013):

$$A_{spot} = \frac{\Delta F}{F} A_{star} \left[1 - \left(\frac{T_{spot}}{T_{star}} \right)^4 \right]^{-1}, \qquad (3)$$

where A_{star} is the apparent area of the star and T_{spot} and T_{star} are the temperature values of the starspot and photosphere of the star. In Figure 6(a), original values of superflares on solar-type stars reported in Shibayama et al. (2013) (from Kepler 30-minute cadence data) and Maehara et al. (2015) (from Kepler 1-minute cadence data) are plotted[25] for comparisons with the results of this study. In these previous papers, we defined the amplitude ($\Delta F/F$) as the brightness range normalized by the average stellar brightness, in which the lower 99% of the distribution of the brightness difference from average, except for the flares, is included. A_{star} and T_{star} values were based on the stellar radius and temperature values used in these previous papers,[26] and we assumed $T_{spot} = 4000$ K.

In this study, we newly updated both of the E_{flare} and A_{spot} values by using the latest $T_{eff,DR25}$ and R_{Gaia} values described in Section 5.1. First, from the superflare stars that we previously reported from Kepler 30-minute and 1-minute time-cadence data (Shibayama et al. 2013; Candelaresi et al. 2014; Maehara et al. 2015) we selected the stars classified again as solar-type stars (main-sequence stars with $T_{eff} = 5100$–6000 K) on the basis of $T_{eff,DR25}$ and R_{Gaia} values (see Figure 5; line (6) of Tables 7 and 8). Not only "subgiants" and "red giants" but also stars identified as "cool main-sequence binary" stars in Figure 5 are not included in the "solar-type" stars classified in this study.

As for the selection from Kepler 30-minute cadence data, we used the data not only from Shibayama et al. (2013) (described in Figure 5(a)) but also from Candelaresi et al. (2014). We investigated superflares on solar-type stars in Shibayama et al. (2013) and those on G-, K-, and M-type stars in Candelaresi et al. (2014). Exactly the same Kepler data set (the first 500 days: Quarters 0–6) is used for the flare surveys in both these studies, and the superflare data of Shibayama et al. (2013) (solar-type stars) exactly correspond to the subset of those of Candelaresi et al. (2014) (G-, K-, and M-type stars). Then in this paper, we newly selected solar-type superflare stars not only from the original solar-type superflare stars in Shibayama et al. (2013) (see Figure 5(a)) but also from the stars originally identified as K- and M-type stars in Candelaresi et al. (2014). A total of 36 superflare stars originally identified as early K-type stars (with $T_{eff} = 4900$–5100 K) in Candelaresi et al. (2014) are newly categorized as solar-type stars with the revised $T_{eff,DR25}$ and R_{Gaia} values (line (7) of Table 7). We note that these superflare stars were not included in Figure 5(a) but are included in the following discussions of solar-type superflare stars in this paper. As a result, 142 solar-type stars (with 597 superflares in total) from Kepler 30-minute cadence data (Shibayama et al. 2013;

Candelaresi et al. 2014; line (8) of Table 7) and 10 solar-type stars (with 51 superflares in total) from 1-minute cadence data (Maehara et al. 2015) are selected (line (6) of Table 8).

We then recalculated E_{flare} and A_{spot} for these selected data. The recalculation of E_{flare} was done by applying these updated $T_{eff,DR25}$ and R_{Gaia} values to the equations presented in Section 2.3 of Shibayama et al. (2013). As for A_{spot}, we used the new methods presented in Maehara et al. (2017). $\Delta F/F$ values taken from McQuillan et al. (2014) were used, and we applied the following relation on the temperature difference between photosphere and spot ($T_{star} - T_{spot}$) deduced from Berdyugina (2005):

$$\Delta T(T_{star}) = T_{star} - T_{spot}$$
$$= 3.58 \times 10^{-5} T_{star}^2 + 0.249 T_{star} - 808. \qquad (4)$$

As a result, we got the resultant values of the updated E_{flare} and A_{spot} values for 113 stars (with 527 flares in total) from Kepler 30-minute cadence data (Shibayama et al. 2013; Candelaresi et al. 2014; line (9) of Table 7) and eight stars (with 48 flares in total) from 1-minute cadence data (Maehara et al. 2015; line (7) of Table 8). We note that only the stars having $\Delta F/F$ values in McQuillan et al. (2014) are selected here. These resultant superflare values are plotted in Figure 6(b).

In Figure 6, the majority of superflares occur on the stars with large starspots, though there is a large scatter. Flares are sudden releases of magnetic energy stored around starspots (see Shibata & Magara 2011). The total energy released by the flare (E_{flare}) must be smaller than (or equal to) the magnetic energy stored around starspots (E_{mag}). Our previous paper (e.g., Shibata et al. 2013) suggested that the upper limit of E_{flare} can be determined by the simple scaling law:

$$E_{flare} \approx f E_{mag} \approx \frac{B^2 L^3}{8\pi} \approx \frac{B^2}{8\pi} A_{spot}^{3/2}$$
$$\approx 7 \times 10^{32} (\text{erg}) \left(\frac{f}{0.1} \right) \left(\frac{B}{10^3 \text{ G}} \right)^2 \left(\frac{A_{spot}}{3 \times 10^{19} \text{ cm}^2} \right)^{3/2}$$
$$\approx 7 \times 10^{32} (\text{erg}) \left(\frac{f}{0.1} \right) \left(\frac{B}{10^3 \text{ G}} \right)^2 \left(\frac{A_{spot}/(2\pi R_\odot^2)}{0.001} \right)^{3/2},$$
$$(5)$$

where f is the fraction of magnetic energy that can be released as flare energy, B and L are the magnetic field strength and size of the spot, and $R_\odot$ is the solar radius. The black solid and dashed lines in Figure 6 represent Equation (5), and almost all the solar flare data are located below these lines. As for the original superflare data from our previous papers (Figure 6(a)), many of the superflares are located below the solid line, but some of them are located above this line. Our previous papers (e.g., Notsu et al. 2013b, 2015b) considered that these stars above this line are expected to have low inclination angle or have starspots around the pole region. In contrast, as for the new data of superflares updated in this study (Figure 6(b)), the number of flares above this line (Equation (5) with $B = 3000$ G) looks to be decreased, and a much higher fraction of superflares are located below this line. In order to see this point more clearly, we plot only the maximum energy flare of each superflare star in Figures 7(a) and (b) and compare them using histograms in Figure 8. The number of stars above the black solid line (the upper-limit line from Equation (5) with

---

[25] Figure 6(a) is basically the same as Figure 5 of Maehara et al. (2015), but we plot it again for the following two reasons. First, it is helpful for readers to compare the original figure with the new one updated in this study. Second, the solid lines corresponding to Equation (5) were mistakenly plotted (the vertical axis values are a factor of 7 smaller than the correct values) in Figure 5 of Maehara et al. (2015), and so it is better to show the revised figure here.

[26] In Shibayama et al. (2013), we used the values taken from the first Kepler Input Catalog (KIC; Brown et al. 2011). In Maehara et al. (2015), we used those from the latest one (the revised KIC) at that time (Huber et al. 2014).
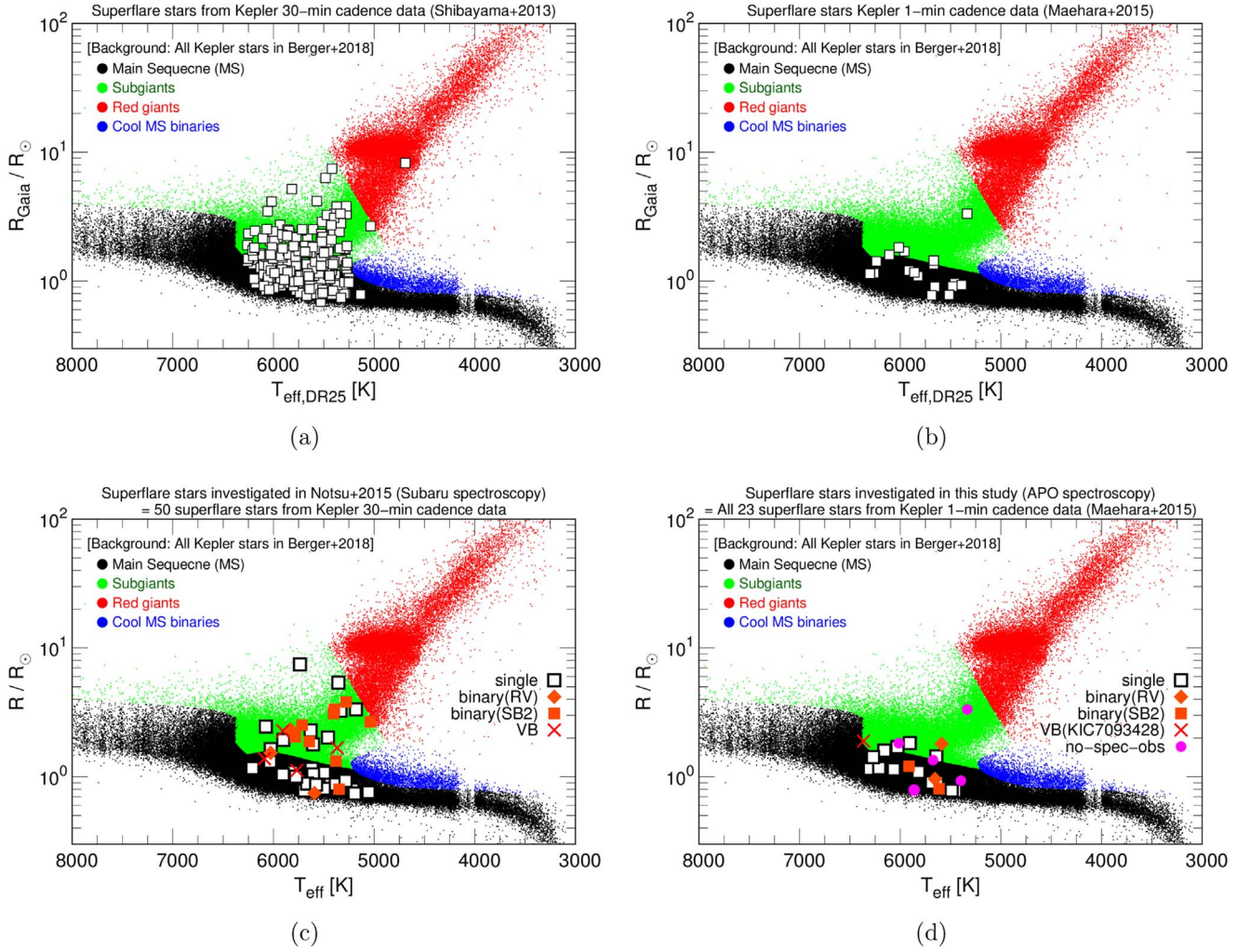
Figure 5. Stellar radius (R) vs. effective temperature $T_{\rm eff}$ of superflare stars. The background black, green, red, and blue circles are all the 177,911 *Kepler* stars listed in Berger et al. (2018) with R_{Gaia} (stellar radius based on *Gaia*-DR2 parallaxes) and $T_{\rm eff,DR25}$ (temperature from DR25-KSPC; Mathur et al. 2017). Each color corresponds to evolutionary state classification presented in Berger et al. (2018): main-sequence stars (black), subgiants (green), red giants (red), and cool main-sequence stars affected by binarity (blue). (a) Superflare stars found from *Kepler* 30-minute cadence data (Shibayama et al. 2013) that have R_{Gaia} values in Berger et al. (2018) are plotted with open squares. The horizontal and vertical axes are R_{Gaia} and $T_{\rm eff,DR25}$, respectively. (b) Same as panel (a), but for superflare stars from *Kepler* 1-minute cadence data (Maehara et al. 2015). (c) Superflare stars that we have investigated with spectroscopic observations using the Subaru telescope (Notsu et al. 2015a, 2015b). The open squares are the target superflare stars classified as single stars (classifications are basically the same as those used in Appendix A.1 of this study). The orange diamonds (RV) and squares (SB2) correspond to the stars classified as binary stars because of RV shifts and double-lined profiles, respectively. Visual binary stars are shown with red crosses. As for the radius value in the vertical axis and the temperature value in the horizontal axis, we use different types of the values for each star. The details are described in Section 5.1. (d) Target superflare stars of this study, which are equal to all 23 superflare stars from *Kepler* 1-minute cadence data reported in Maehara et al. (2015). The symbols and axes are used the same way as in panel (c). Pink circles correspond to the five faint superflare stars for which we did not get spectra with enough S/N in this study (see Section 2).

$B = 3000$ G and the inclination angle $i = 90°$) is significantly decreased. With these updates, it is more strongly supported that the upper limit of the energy released by the flare is not inconsistent with the magnetic energy stored around the starspots.

Next, we see this point (the difference of the number of superflare stars above Equation (5) between the previous studies and this study) a bit more in detail by incorporating the results of our spectroscopic studies in Section 4. In Figure 2 in Section 4.3, we compared the projected rotational velocity ($v \sin i$) with the stellar rotational velocity ($v_{\rm lc}$) on the basis of our spectroscopic observations (Notsu et al. 2015b; this study), and stellar inclination angle (i) can be calculated using Equation (2). We plot again the data of single superflare stars in Figure 9. In this figure, we newly classified solar-type stars by using spectroscopically measured temperature ($T_{\rm eff,spec}$) and

stellar radius values ($R_{\rm gaia}$ or $R_{\rm spec}$) in Figures 5(c) and (d). White open symbols and black filled ones are solar-type stars (main-sequence stars with $T_{\rm eff} = 5100$–6000 K). The former points are the stars having $A_{\rm spot}$ values deduced from $\Delta F/F$ in McQuillan et al. (2014) so that we can plot the data points in Figure 10(b), but the latter ones are the stars without $\Delta F/F$ values in McQuillan et al. (2014) so that we cannot plot the data in Figure 10(b). Orange and green symbols correspond to the main-sequence stars with a bit hotter ($T_{\rm eff} = 6000$–6300 K) and a bit cooler ($T_{\rm eff} = 5000$–5100 K) temperature values, respectively. Red symbols are the stars classified as subgiants (see Section 5.1). As a result, many of the low inclination angle stars are not classified as solar-type stars in this study.

Then, in Figures 10(a) and (b), we overplotted the maximum energy flare data of these spectroscopically observed superflare stars on the data of Figures 7(a) and (b), respectively. In
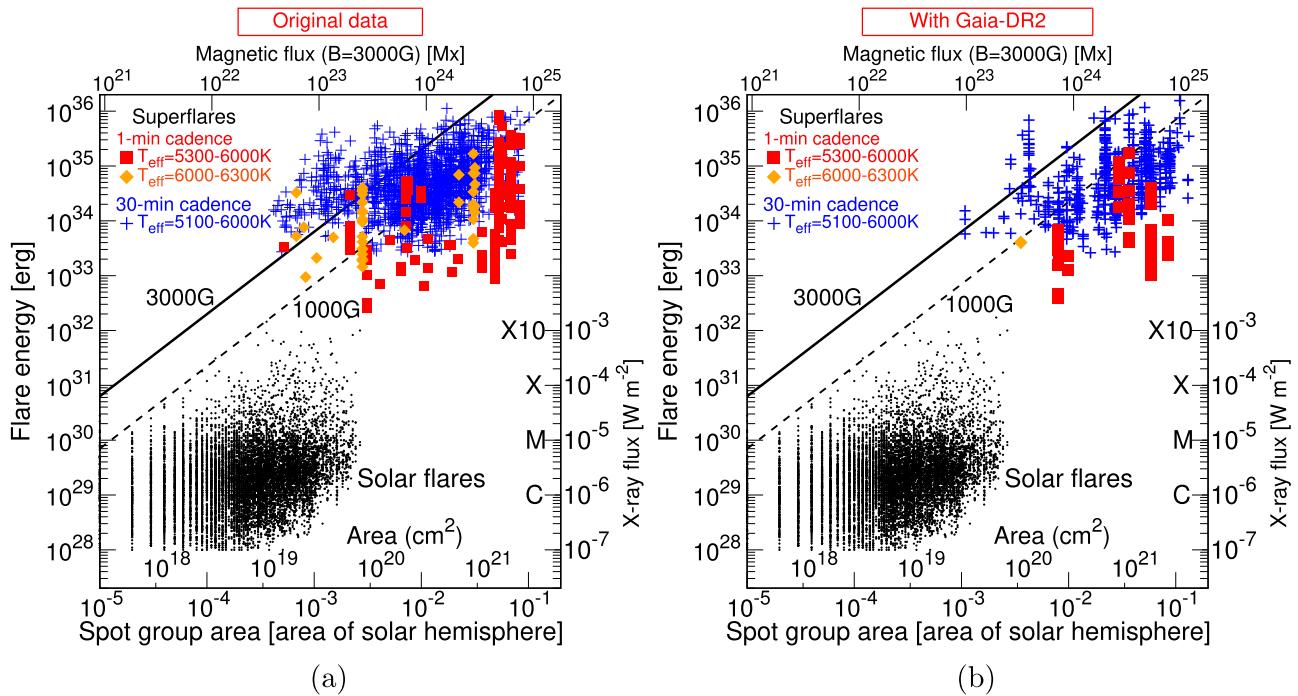
Figure 6. Scatter plot of flare energy (E_{flare}) as a function of spot area (A_{spot}) for solar flares and superflares. The lower and upper horizontal axes indicate the area of the spot group in the units of the area of the solar hemisphere ($A_{1/2\odot} \sim 3 \times 10^{22}$ cm^2) and the magnetic flux for $B = 3000$ G. The vertical axis represents the bolometric energy released by each flare. The data of solar flares are exactly the same as those in our previous studies (e.g., Figure 5 of Maehara et al. 2015). We assumed that bolometric energies of B-, C-, M-, X-, and X10-class solar flares are 10^{28}, 10^{29}, 10^{30}, 10^{31}, and 10^{32} erg, respectively, from observational estimates of typical solar flare energies (see the main text for details). The black solid and dashed lines correspond to the analytic relationship between E_{flare} and A_{spot} from Equation (5) for $B = 3000$ and 1000 G, respectively. (a) Original data of superflares on solar-type (G-type main-sequence) stars presented in our previous studies (Shibayama et al. 2013 and Maehara et al. 2015). Blue crosses indicate 1549 superflares (on 279 stars) detected from *Kepler* 30-minute cadence data (Shibayama et al. 2013), while red squares and orange diamonds are those (187 flares on 23 stars) detected from 1-minute cadence data (Maehara et al. 2015). Among the 187 flares from 1-minute cadence data, stars with $T_{eff} = 6000$–6300 K, which are not included in the range of solar-type stars in this study ($T_{eff} = 5100$–6000 K), are distinguished with orange diamonds. (b) Data of superflares on solar-type stars updated in this study using $T_{eff,DR25}$ and R_{Gaia} values. Symbols are used in the same way as in panel (a). In addition to the data of solar-type stars (blue crosses and red squares), the data of one main-sequence star with $T_{eff} = 6000$–6300 K (KIC 8508009) from *Kepler* 1-minute cadence data are also calculated and plotted for reference.

Figure 10(a), the starspot size and flare energy data of the overplotted stars are taken from those used in Figure 7(a).[27] As for Figure 10(b), we update starspot size and flare energy values of the overplotted stars by recalculating them with $T_{eff,spec}$ and stellar radius values (R_{gaia} or R_{spec}) used in Figures 5(c) and (d). The equations used for these recalculations are the same as those used for Figures 6(b) and 7 in the above. Notsu et al. (2015b) suggested that many of the data points located on the upper left side of the A_{spot} versus E_{flare} diagram tend to have low inclination angle values. This tendency can also be seen in Figure 10(a), but most of these low inclination angle stars are now classified as subgiant stars (i.e., red points in this figure). In the updated Figure 10(b), the data points are located more in the lower right side of this diagram. There is only one star above the black solid line (Equation (5)). However, the number of stars is decreased in Figure 10(b) compared with Figure 10(a), and we need to increase the number of target stars with more spectroscopic observations in the future.

Finally, in Figures 11(a) and (b), we plot again A_{spot} and E_{flare} values (taken from Figure 6(b)), separating the superflare data on the basis of the stellar temperature values. The data of

the stars with a temperature range ($T_{eff} = 5600$–6000 K) close to the solar temperature are plotted in Figure 11(b), while those of late G-type main-sequence stars ($T_{eff} = 5100$–5600 K) are in Figure 11(a). There are no big differences between Figures 11(a) and (b). As a result, almost all the data points of superflares are located below the line of Equation (5), and we confirmed again that the upper limit of the energy released by flares is not inconsistent with the magnetic energy stored around the starspots.

5.3. Dependence of Superflare Energy and Frequency on Rotation Period

Previous observations of solar-type stars (e.g., X-ray, UV, Ca II H and K) have shown that the stellar magnetic activity level decreases as rotation period increases (e.g., Noyes et al. 1984; Güdel 2007; Wright et al. 2011). Since stellar age has a good correlation with rotation, young, rapidly rotating stars show the higher activity levels, and it was expected that they show more energetic flares more frequently compared with slowly rotating stars like the Sun. In our previous paper (Notsu et al. 2013b), we investigated the relationship between the superflare energy (E_{flare}) and the rotation period (P_{rot}) and suggested that the maximum superflare energy in a given rotation period bin does not have a clear correlation with the rotation period (Figure 12(a) of this paper), while the average flare frequency in a given period bin has a correlation with the rotation (Figure 7(b) of Notsu et al. 2013b and Figure 2 of

---

[27] We note that three spectroscopically investigated stars (KIC 7420545, KIC 6934317, and KIC 8429280) that are not in Figure 7(a) are also included in this figure. These stars were not included in the data of Shibayama et al. (2013) but have been spectroscopically investigated in our previous papers (see the footnote of Table 1 of Notsu et al. 2015b).
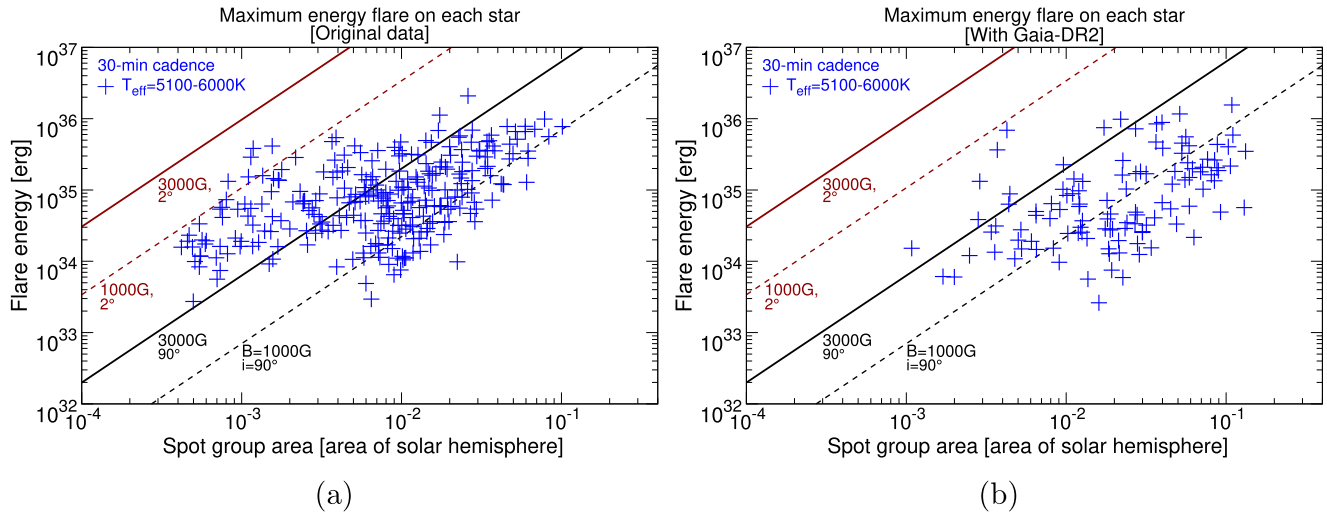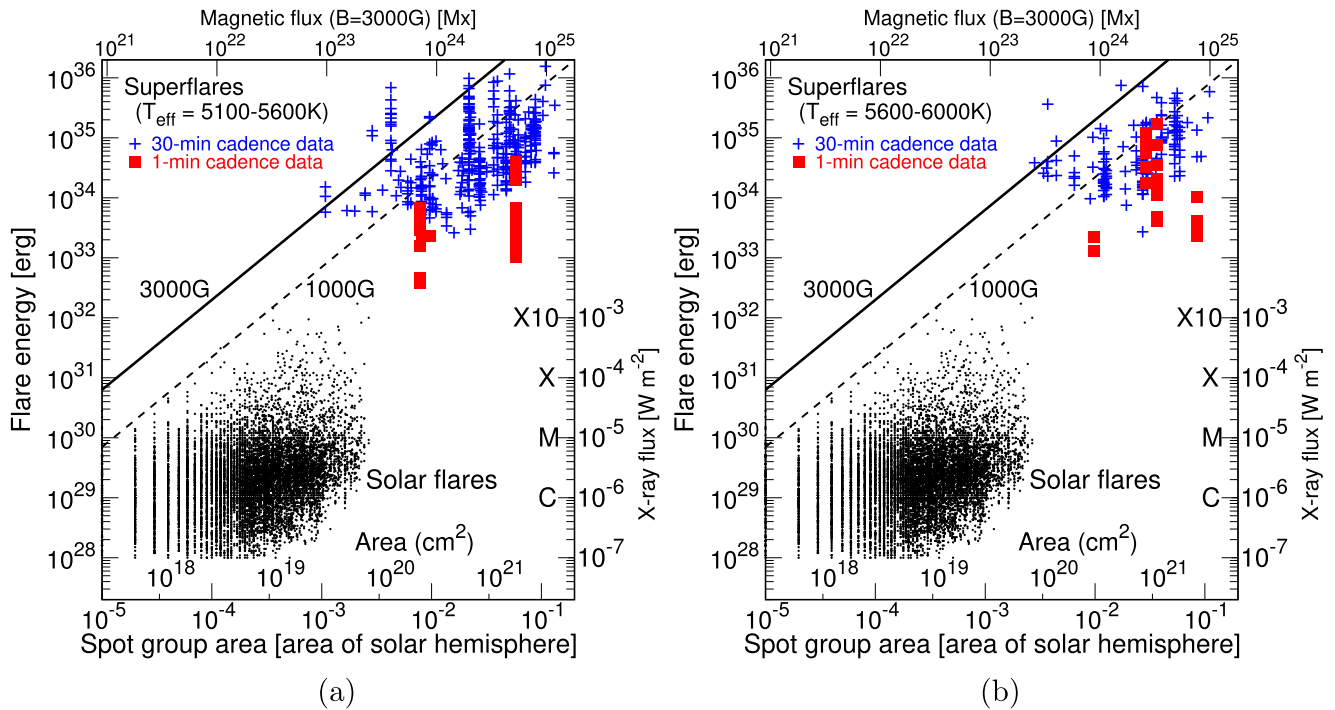
Figure 7. (a) Scatter plot of flare energy (E_{flare}) as a function of spot area (A_{spot}) for superflares (as Figure 6), but only the maximum energy flare of each superflare star from *Kepler* 30-minute cadence data using the original data in Shibayama et al. (2013) is plotted. The black solid and dashed lines correspond to the analytic relationship between E_{flare} and A_{spot} from Equation (5) with the inclination angle $i = 90°$ for $B = 3000$ and 1000 G, respectively. The dark-red solid and dashed lines correspond to the same relationship with $i = 2°$ for $B = 3000$ and 1000 G, respectively. (b) Same as panel (a), but only the maximum energy flare of each superflare star from *Kepler* 30-minute cadence data using the data updated with $T_{eff,DR25}$ and R_{Gaia} in this study is plotted.
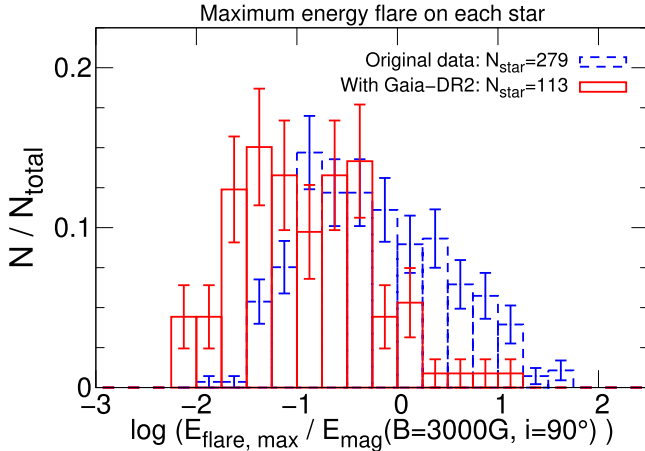
Figure 8. Histograms showing the distribution of the maximum energy flare of each superflare star ($E_{flare,max}$) found from *Kepler* 30-minute time-cadence data. The horizontal axis value is the fraction of $E_{flare,max}$ to the upper-limit magnetic energy (E_{mag}). E_{mag} values correspond to the black solid lines in panels (a) and (b) ($B = 3000$ G and $i = 90°$) at the A_{spot} value of each star. The blue dashed line corresponds to the original superflare data shown in Figure 7(a), while the red solid line corresponds to the updated data in Figure 7(b). The error bars represent the 1σ uncertainty estimated from the square root of the number of stars in each bin.

Figure 9. Projected rotational velocity ($v \sin i$) vs. the stellar rotational velocity (v_{lc}) estimated from the period of the brightness variation (P_{rot}) and stellar radius (R). The data points are basically the same as those of Figure 2 in Section 4.3, but they are limited to single superflare stars. The three single stars (KIC 11652870, KIC 4554830, and KIC 11253827, which are shown with blue triangles in Figure 2) that have only $v \sin i$ upper-limit values in APO data (and no values from Subaru data) are removed from this figure since we cannot estimate their inclination angle values correctly. They are classified with colors and shapes of the symbols on the basis of the stellar type classifications (see the main text for details) and inclination angles (circles: $i \geqslant 60°$; squares: $30° < i \leqslant 60°$; upward-pointing triangles: $10° < i \leqslant 30°$; downward-pointing triangles: $i < 10°$), respectively. The solid line represents the case in which our line of sight is vertical to the stellar rotation axis ($i = 90°$, $v \sin i = v_{lc}$). We also plot three different lines, which correspond to smaller inclination angles ($i = 60°$, $30°$, $10°$).

Maehara et al. 2015). This suggestion is important since, against the above-mentioned previous expectations, energetic superflares with $\sim 10^{35}$ erg can occur on solar-type stars rotating as slow as the Sun ($P_{rot} \sim 25$ days), even though the frequency is low (once in a few thousand years), compared with rapidly rotating stars.

Next, we investigate again this relation by using superflare values updated with *Gaia*-DR2 stellar radius (R_{Gaia}) data. In Section 5.2, we newly classified solar-type stars on the basis of $T_{eff,DR25}$ and R_{Gaia} and recalculated flare energy E_{flare}. Figure 12(b) shows the relationship between this updated E_{flare} value and the rotation period P_{rot} of each solar-type superflare star. P_{rot} values plotted here are taken from McQuillan et al. (2014). Unlike the results of our previous studies (Figure 12(a)), Figure 12(b) suggests that the upper

limit of E_{flare} in each period bin has a continuous decreasing trend with rotation period. For example, stars rotating as slow as the Sun ($P_{rot} \sim 25$ days) show superflares up to 10^{35} erg, while rapidly rotating stars with $P_{rot} = 1-3$ days have more energetic superflares, up to 10^{36} erg.

Flare activity also depends on stellar temperature (Candelaresi et al. 2014; Davenport 2016; Van Doorsselaere et al. 2017), and even among solar-type stars, cooler stars can have higher flare activities (see Figure 5 of Shibayama et al. 2013). Then, the data of superflares plotted in Figure 13 are separated into panels (a)
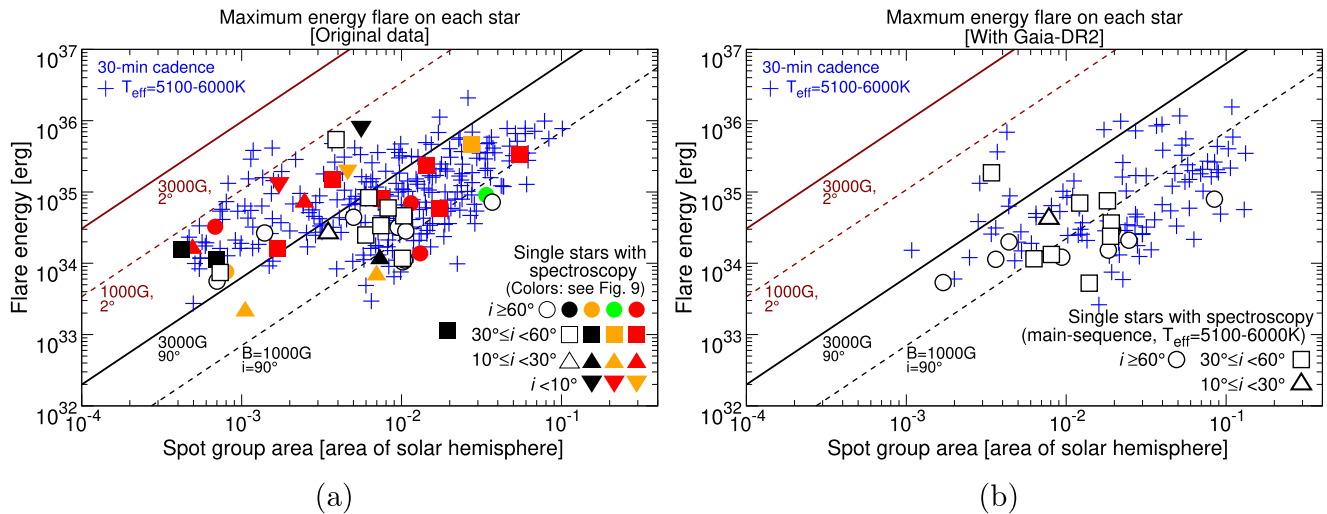
Figure 10. (a) Same as Figure 7(a), but the data of maximum energy flares on single superflare stars that we have spectroscopically investigated (Figure 9) are overplotted with bigger points. The colors and shapes of the overplotted symbols are used in the basically the same way as in Figure 9. (b) Same as Figure 7(b), but the maximum energy flares on single superflare stars that we have spectroscopically investigated (Figure 9) are overplotted using the updated values (see the main text for details). Different from Figure 10(a), only the stars categorized as solar-type stars in this study are plotted. The shapes of the overplotted symbols (open points) are used in basically the same way as in Figure 9.

and (b) on the basis of the stellar temperature values. The data of the stars with a temperature range (T_{eff} = 5600–6000 K) close to the solar temperature are plotted in Figure 13(b), while those of late G-type main-sequence stars (T_{eff} = 5100–5600 K) are in Figure 13(a). In Figure 13(b), we also added the scale of stellar age (t) on the basis of the gyrochronology relation of solar-type stars ($t \propto P_{rot}^{0.6}$; Ayres 1997) in order to compare the age of superflare stars with that of the Sun (t = 4.6 Gyr). The scale of t is only plotted in the limited age range t = 0.5–5 Gyr for the following two reasons: (1) As for young solar-type stars with $t \lesssim 0.5$–0.6 Gyr, a large scatter in the age–rotation relation has been reported from young cluster observations (e.g., Soderblom et al. 1993; Ayres 1997; Tu et al. 2015). (2) As for old solar-type stars beyond solar age (t = 4.6 Gyr), a breakdown of gyrochronology relations has been recently reported (van Saders et al. 2016; Metcalfe & Egeland 2018). With this scale, for example, we can see that Sun-like stars with $P_{rot} \sim 25$ days are more than four times older ($t \sim 4.6$ Gyr) than the stars with $P_{rot} \sim 10$ days ($t \sim 1$ Gyr).

As a result of Figures 13(a) and (b), we confirmed again the suggestions from Figure 12(b). The upper limit of superflare energy in each period bin depends on the rotation period in both Figures 13(a) and (b), and there is a one-order-of-magnitude difference between the maximum flare energy on young stars ($t < 0.5$ Gyr) and that on Sun-like old stars ($t \sim 4.6$ Gyr). We cannot judge whether there are any clear differences between these two figures because of the low number statistics. It is necessary to increase the number of superflare data with future observations (see also Section 6.3).

Then, we see the relation between flare frequency and rotation period by using the updated superflare data. Figure 14 shows that the average flare frequency in a given period bin tends to decrease as the period increases in the range of P_{rot} longer than a few days. The frequency is averaged from all of the superflare stars in the same period bin. This result is basically the same as that presented in Notsu et al. (2013b) with the original superflare data. The frequency of superflares on young, rapidly rotating stars (P_{rot} = 1–3 days) is ~ 100 times higher compared with old, slowly rotating stars

($P_{rot} \sim 25$ days), and this indicates that as a star evolves (and its rotational period increases), the frequency of superflares decreases. We can now interpret that this correlation between the rotation period (roughly corresponding to age) and flare frequency is consistent with the correlation between the rotation period (age) and previous measurement of the stellar activity level such as the average X-ray luminosity (e.g., Noyes et al. 1984; Güdel 2007; Wright et al. 2011). Summarizing the results in this section, superflares with their energy $\lesssim 5 \times 10^{34}$ erg can occur on old, slowly rotating Sun-like stars (T_{eff} = 5600–6000 K, $P_{rot} \sim 25$ days, and $t \sim 4.6$ Gyr), even though the frequency and maximum flare energy are lower compared with young, rapidly rotating stars and cooler stars.

5.4. Starspot Size versus Rotation Period of Solar-type Stars, and Implications for Superflare Energy

Our previous paper (Maehara et al. 2017) investigated the statistical properties of starspots on solar-type stars by using the starspot size A_{spot} and rotation period P_{rot} estimated from the brightness variations of *Kepler* data. Here we update these values by using *Gaia*-DR2 stellar radius, as also done for superflare stars in the above. As done in Maehara et al. (2017), we used P_{rot} and brightness variation amplitude $\Delta F/F$ values reported in McQuillan et al. (2014). We newly classified 49,212 solar-type stars (N_{data} in Table 9 in Appendix B) among the stars in McQuillan et al. (2014) by using $T_{eff,DR25}$ and R_{Gaia} values, as done for superflare stars in Section 5.2. P_{rot} and $\Delta F/F$ values of 11,594 stars (see N_P(all) values in Table 9) are detected among these 49,212 stars. Then, we recalculated A_{spot} values from $\Delta F/F$ values, using these $T_{eff,DR25}$ and R_{Gaia} values. The method of A_{spot} calculation is exactly the same as those used for superflare stars in Section 5.2. The resultant values are plotted in Figure 15. The data in Figure 15 are separated into panels (a) and (b) on the basis of the temperature values. The data of the stars with a temperature range (T_{eff} = 5600–6000 K) close to the solar temperature are plotted in Figure 15(b), while those of late G-type main-sequence stars (T_{eff} = 5100–5600 K) are in Figure 15(a). The stars showing

Figure 11. Scatter plot of flare energy ($E_{\rm flare}$) as a function of spot area ($A_{\rm spot}$) of solar flares and superflares (as Figure 6(b)). Blue plus signs and red filled squares are the data of superflares found from *Kepler* 30-minute and 1-minute time-cadence data, respectively, which are originally from Figure 6(b). They are separated on the basis of the stellar temperature values: (a) $T_{\rm eff} = 5100$–5600 K and (b) $T_{\rm eff} = 5600$–6000 K.

superflares tend to have shorter rotation periods (younger ages) and larger starspot areas.

Figure 15(b) shows that the largest area of starspots on Sun-like stars with $T_{\rm eff} = 5600$–6000 K in a given period bin has roughly a constant or very gentle decreasing trend around $A_{\rm spot} = 5 \times 10^{-2}$–$1 \times 10^{-1} A_{1/2\odot}$ in the period range of $P_{\rm rot} \lesssim 12$ days (age: $t \lesssim 1.4$ Gyr). However, in the period range of $P_{\rm rot} \gtrsim 12$ days ($t \gtrsim 1.4$ Gyr), the largest starspot area on them clearly decreases as the rotation period increases. As for the late G-type main-sequence stars with $T_{\rm eff} = 5100$–5600 K in Figure 15(a), the similar steep trends can be seen for maximum size of starspots, but the exact values are a bit different. This steep decreasing trend starts around $P_{\rm rot} \sim 14$ days (Figure 15(a)). In the longer period range, the maximum area of spots on the stars with $T_{\rm eff} = 5600$–6000 K at a given period bin is roughly half compared with those of the stars with $T_{\rm eff} = 5100$–5600 K (see the black dashed line in Figure 15(b)). These differences support that cooler stars can generate larger magnetic flux more effectively thanks to the development of the convection zone. We discuss such temperature differences of the $P_{\rm rot}$ versus $A_{\rm spot}$ relations including more cooler (K- and M-type) dwarf stars in more detail in our next study (H. Maehara et al. 2019, in preparation).

The trends similar to those presented here were already reported in Figure 1(a) of Maehara et al. (2017), but we did not discuss the temperature differences. Moreover, the steep decreasing trend in the longer period range is now much clearer compared with this previous paper. It might be because the errors of $A_{\rm spot}$ values decrease thanks to the updates using *Gaia*-DR2 stellar radius (R_{Gaia}) values, and the potential contamination of subgiants in the previous data can also be eliminated. Then, the steep decreasing trend of maximum spot area in the longer period range is more strongly supported.

In Section 5.3, we reported that maximum energy of superflares in a given period bin decreases as $P_{\rm rot}$ increases (Figures 13(a) and (b)). This decreasing trend of maximum flare energy can be related to the decreasing trend of maximum area of starspots in the longer-period regime in Figures 15(a) and (b) described in this section. This is because the maximum area of starspots determines well the upper limit of flare energy (see Section 5.2). For example, Figure 15(b) shows that the maximum size of starspots on old ($t \sim 4.6$ Gyr) Sun-like stars with $T_{\rm eff} = 5600$–6000 K and $P_{\rm rot} \sim 25$ days is $\sim 1\%$ of the solar hemisphere. This corresponds to flare energy of 10^{34}–10^{35} erg on the basis of Equation (5), and the upper limit of superflare energy of such Sun-like stars in Figure 13(b) is roughly in the same range.

However, there is a difference in a bit strict sense between the decreasing trend of the maximum superflare energy in Figures 13(a) and (b) and that of the maximum area of starspots in Figures 15(a) and (b). The maximum superflare energy roughly continuously decreases as the rotation period increases (the star becomes older) in Figures 13(a) and (b), but the maximum area of starspots does not show such continuous decreasing trend in Figures 15(a) and (b). The maximum area of starspots is constant in the short-period range ($P_{\rm rot} \lesssim 12$–14 days), but it steeply decreases as the period increases in the longer range ($P_{\rm rot} \gtrsim 12$–14 days). This difference can suggest a possibility that the flare energy is determined not only by the starspot area but also by the other important factors, though the starspot area is still a necessary condition determining flare energy (see Section 5.2). By analogy with the correlation between the flare activity and the magnetic structure of sunspot groups (see Sammis et al. 2000; Maehara et al. 2017), one of the possible factors might be the effect of the magnetic structure of starspots. More complex spots can generate more frequent and more energetic flares
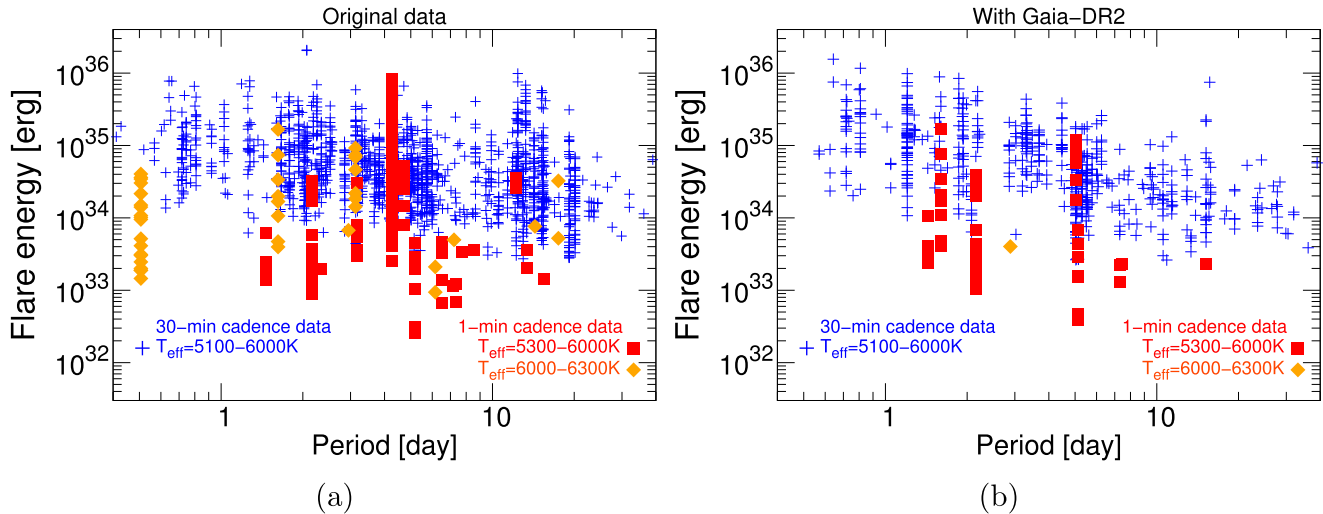
Figure 12. Scatter plot of the superflare energy (E_{flare}) vs. the rotation period (P_{rot}) of each star (estimated from the brightness variation period). Apparent negative correlations between P_{rot} and the lower limit of E_{flare}, which are mainly seen for blue plus signs, result from the detection limit of our flare search method (see Shibayama et al. 2013). (a) Original data of superflares on solar-type (G-type main-sequence) stars presented in our previous studies (Shibayama et al. 2013; Maehara et al. 2015). Blue plus signs indicate superflares detected from *Kepler* 30-minute cadence data (Shibayama et al. 2013), while red squares and orange diamonds are those detected from 1-minute cadence data (Maehara et al. 2015). Among the flares from 1-minute cadence data, stars with T_{eff} = 6000–6300 K, which are not included in the range of solar-type stars in this study (T_{eff} = 5100–6000 K), are distinguished with orange diamonds. (b) Data of superflares updated in this study using $T_{eff,DR25}$ and R_{Gaia} values. Symbols are used in the same way as in panel (a). In addition to the data of solar-type stars (blue plus signs and red squares), the data of one main-sequence star with T_{eff} = 6000–6300 K (KIC 8508009) from *Kepler* 1-minute cadence data are also calculated and plotted for reference.

according to solar observations. If the magnetic structure (complexity) of spots also has a correlation with the rotation period, the upper limit of flare energy can depend on rotation period even if the starspot size is roughly constant. We need to conduct more detailed studies on starspot properties to clarify such possibilities (see also the final paragraph of Maehara et al. 2017). We must note here that we also need more superflare observations to more quantitatively discuss the above difference between Figures 13 and 15, since the number of superflare events, especially in Figure 13(b), is small.

In addition, the existence of constant and decreasing trends of maximum starspot coverage can be compared with the relation between SXR flux and rotation period (e.g., Wright et al. 2011). The SXR fluxes of solar-type stars are also known to show the constant regime (or so-called "saturation" regime) in the period range of $P_{rot} \lesssim 2$–3 days, but they decrease constantly as the P_{rot} values increase in the range of $P_{rot} > 2$–3 days. The changing point of this SXR trend ($P_{rot} \sim 2$–3 days) is different from that of maximum spot size values ($P_{rot} \sim 12$–14 days). Although a detailed study on this point is beyond the scope of this paper, these similarities and differences can be interesting and helpful when considering the relation between stellar activity (including starspots, flares, X-ray steady emissions) and rotation in more detail.

5.5. Superflare Frequency on Sun-like Stars and Implications for the Sun

Figure 16 represents the occurrence frequency distributions of superflares on solar-type stars with T_{eff} = 5600–6000 K ("the temperature range close to the solar value" in the above sections) and various rotation period (P_{rot}) values, derived from the superflare data updated earlier in this study. As also presented in our previous studies (e.g., Shibayama et al. 2013) with the original data of superflares, we can see that there are the power-law distributions ($dN/dE \propto E^{-\alpha}$ with the index $\alpha \lesssim 2$), and rapidly rotating stars tend to have larger frequency

values. The upper-limit values of flare energy roughly depend on rotation period, as already seen in Figure 13. However, error values are relatively large, especially for slowly rotating stars, because of the small number of analyzed data. For example, one blue circle in the energy range $E_{flare} = 10^{35.75}$–$10^{36.0}$ erg in Figure 16, which is a bit far from the other blue circles, corresponds to only one superflare event. We must note here that these values are treated with caution, and we need to increase the number of slowly rotating superflare stars by including more new data in the future. We also note here that, as in Figure 14, the flare frequency value in the vertical axis of Figure 16 is calculated by using the number of solar-type stars in each P_{rot} bin ($N_P(P_{rot})$ in Table 9 in Appendix B) detected in McQuillan et al. (2014). The potential errors from this $N_P(P_{rot})$ value, which are discussed in Appendix B, should be kept in mind when we discuss the dependence of flare frequency on the rotation period on the basis of Figure 16. For example, flare frequency of Sun-like stars with $P_{rot} = 20$–40 days could become a factor of two smaller in the largest error case, and more investigations with new data in the future are strongly needed.

Our previous papers (Shibayama et al. 2013; Maehara et al. 2015) pointed out that the frequency distribution of superflares on Sun-like stars and those of solar flares are roughly on the same power-law line. However, the definition of Sun-like stars in these previous studies ($T_{eff} = 5600$–6000 K and $P_{rot} > 10$ days) includes many stars much younger than the Sun. For example, stars with $P_{rot} \sim 10$ days have an age of $t \sim 1$ Gyr (see Figures 13(b) and 15(b)). It might be better to use only the data of stars rotating as slowly as the Sun ($P_{rot} \sim 25$ days and $t \sim 4.6$ Gyr). Then, in Figure 17 we newly plot the frequency value of superflares on Sun-like stars with $P_{rot} = 20$–40 days ($t > 3.2$ Gyr) taken from Figure 16, in addition to the data of solar flares and superflares shown in Figure 4 of Maehara et al. (2015). As a result, the newly added data point of superflares on Sun-like stars is roughly on the same power-law line, though the exact value of superflare
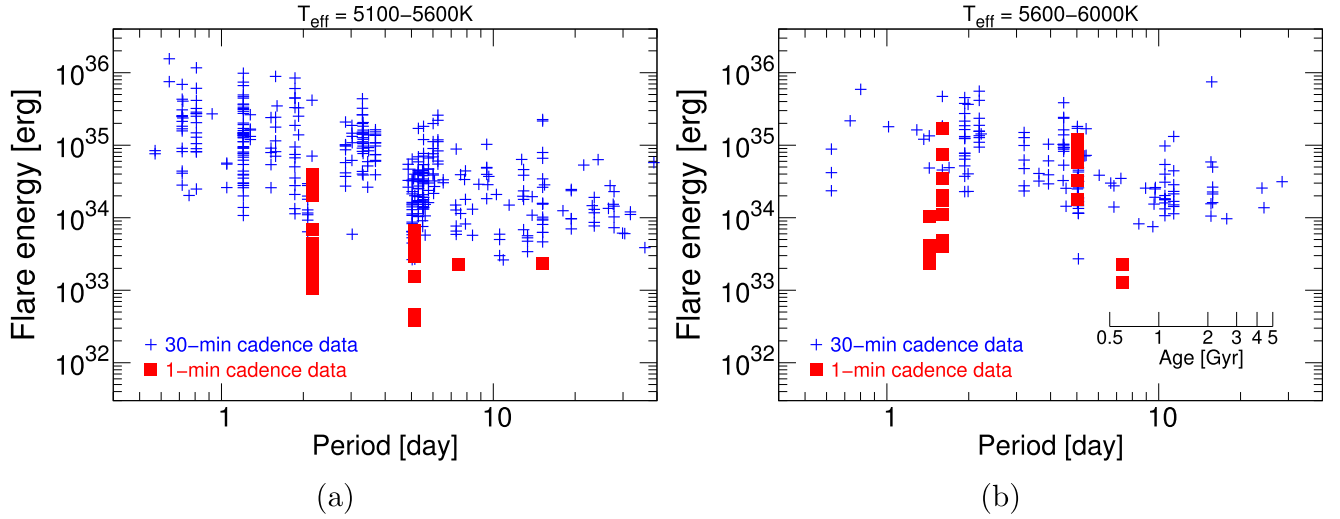
Figure 13. Scatter plot of the superflare energy (E_{flare}) vs. the rotation period (P_{rot}) of each star (as Figure 12(b)). Blue plus signs and red filled squares are the data of superflares found from *Kepler* 30-minute and 1-minute time-cadence data, respectively, which are originally from Figure 12(b). They are separated on the basis of the stellar temperature values: (a) T_{eff} = 5100–5600 K and (b) T_{eff} = 5600–6000 K. Only in panel (b) did we add the scale of stellar age (t) on the basis of the gyrochronology relation of solar-type stars ($t \propto P_{rot}^{0.6}$; Ayres 1997; see main text for details).
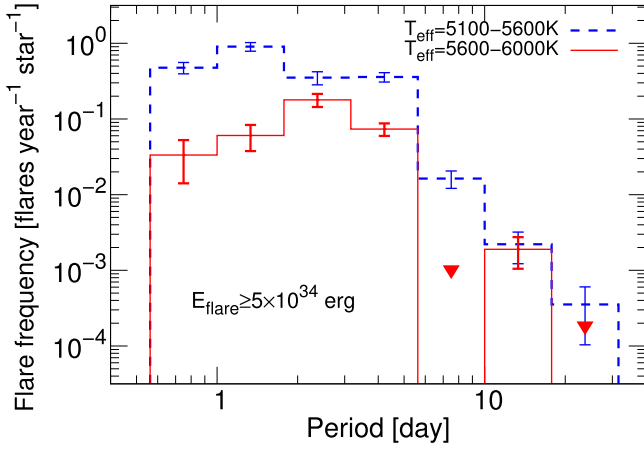
Figure 14. Occurrence frequency distribution of superflares as a function of the rotation period (P_{rot}), using the data of superflares on solar-type stars that were originally found from *Kepler* 30-minute cadence data (Shibayama et al. 2013; Candelaresi et al. 2014) but are updated with $T_{eff,DR25}$ and R_{Gaia} in this study (E_{flare} and P_{rot} data in Figure 12). The vertical axis indicates the number of superflares with energy $\geqslant 5 \times 10^{34}$ erg per star and per year. The error bars represent the 1σ uncertainty estimated from the square root of the number of flares in each bin. Unlike Figure 7 of Notsu et al. (2013b), we do not take into account the error values of E_{flare} since this is now more reliable with *Gaia*-DR2 stellar radius values. This vertical axis value is calculated by using the number of solar-type stars in each P_{rot} bin ($N_P(P_{rot})$ in Table 9) detected in McQuillan et al. (2014). The potential errors from this $N_P(P_{rot})$ value are discussed in Appendix B. Red solid lines correspond to the frequency values calculated from the solar-type stars with their temperature values limited to a range (T_{eff} = 5600–6000 K) close to the solar temperature, while blue dashed lines are those from the late G-type main-sequence stars with T_{eff} = 5100–5600 K. $T_{eff,DR25}$ values are used for the temperature classifications here. As for the red solid lines, in the case of no events in a period bin, the upper-limit values are shown with the red downward-pointing triangles assuming that less than one event occurs in each bin.

frequency of stars with P_{rot} = 20–40 days ($t >$ 3.2 Gyr) is a bit smaller than those of stars with $P_{rot} >$ 10 days ($t >$ 1 Gyr). From this figure, we can roughly remark that superflares with energy $>10^{34}$ erg would be approximately once every 2000–3000 yr on old Sun-like stars with $P_{rot} \sim$ 25 days and $t \sim$ 4.6 Gyr, though the error value is relatively large because of the small amount of data of slowly rotating stars.

We note here that several potential candidates of extreme solar flare events, which can be bigger than the largest solar flare in the past 200 yr ($E_{flare} \sim 10^{32}$ erg), have been reported from the data over the recent 1000–2000 yr (e.g., Usoskin 2017 for review). For example, significant radioisotope ^{14}C enhancements have been reported in tree rings for the years AD 775 and AD 994, and they suggest extremely strong and rapid cosmic-ray increase events possibly caused by extreme solar flares (e.g., Miyake et al. 2012, 2013). Various potential low-latitude auroral drawings have also been reported from the historical documents around the world, and they suggest the possibility that extreme solar flare events have occurred several times in the recent $\sim$1000 yr (e.g., Hayakawa et al. 2017a, 2017b). In the future studies, the superflare frequency information as in Figure 17 should be compared with these radioisotope and historical data in detail.

5.6. Size–Frequency Distribution of Starspots and Comparison with Sunspots

In addition to the relation between the rotation period and starspot area in Section 5.4, in the following we also investigate the size–frequency distribution of large starspot groups on Sun-like stars and that of sunspots. Our previous paper (Maehara et al. 2017) already conducted this analysis, but here we aim to investigate again whether both sunspots and larger starspots can be related to the same physical processes, by including the updates using *Gaia*-DR2 stellar radius values.

Figure 18 shows the comparison between the cumulative appearance frequency of starspots on Sun-like stars (T_{eff} = 5600–6000 K and P_{rot} = 20–40 days) and that of sunspot groups. The estimation method of the cumulative appearance frequency values is basically the same as that used for Figure 5 of Maehara et al. (2017), and this was already described in detail in that paper. Only one difference is that we use the updated A_{spot} values described in the above Section 5.4. The occurrence frequency decreases as the area of sunspots or starspots increases. The appearance rate of both the sunspot groups and that of starspots with the area $>10^{-2.5}A_{1/2\odot}$ is approximately once in a few years. The cumulative appearance

frequency of starspots on Sun-like stars can be fitted by a power-law function with the power-law index of -2.9 ± 0.5 (red dashed line) for spot areas between $10^{-2.5}A_{1/2\odot}$ and $10^{-1.0}A_{1/2\odot}$. This power-law index is a bit steeper compared with those originally presented in Maehara et al. (2017).

According to Bogdan et al. (1988), the size distribution of individual sunspot umbral areas shows lognormal distribution. Although the overall size–frequency distribution of sunspot groups in Figure 18 also shows a similar lognormal distribution, the distribution of sunspot groups for large sunspots is roughly on this power-law line for sunspot areas between $10^{-3.25}A_{1/2\odot}$ and $10^{-2.5}A_{1/2\odot}$. The appearance frequency of sunspots with spot areas of $\sim 10^{-2}A_{1/2\odot}$ is about 10 times lower than that of starspots on Sun-like stars. This difference between the Sun and Sun-like stars might be caused by the lack of a "superactive" phase on our Sun during the past 140 yr (Schrijver et al. 2012). These results shown here are basically the same as those originally presented in Maehara et al. (2017), and we confirmed the similarity between the size distribution of sunspots and that of starspots. This supports that both sunspots and larger starspots could be related to the same physical processes. The upper limit of starspot size values of Sun-like stars in Figure 18 is approximately a few $\times 10^{-2}A_{1/2\odot}$, and the appearance frequency of these spots is approximately once every 2000–3000 yr.

6. Summary and Future Prospects

This paper reports the latest view of superflares on solar-type stars found from our series of studies using *Kepler* data, by including the recent updates using APO 3.5 m telescope spectroscopic observations and *Gaia*-DR2 data.

6.1. Summary of APO 3.5 m Telescope Spectroscopic Observations

In Sections 2–4, we described the results of our spectroscopic observations of *Kepler* solar-type superflare stars. We newly conducted APO 3.5 m telescope spectroscopic observations of the 18 solar-type superflare stars found from *Kepler* 1-minute (short) time-cadence data (Maehara et al. 2015).

(i) More than half (43 stars) are confirmed to be "single" stars, among the 64 solar-type superflare stars in total that have been spectroscopically investigated so far in this APO 3.5 m observation and our previous Subaru/HDS (Notsu et al. 2015a) observations (Table 6).

(ii) The "$v \sin i$" (projected rotational velocity) values are consistent with the rotational velocity values v_{lc} estimated from the brightness variation period of *Kepler* data (Figure 2).

(iii) There is a positive correlation between the amplitude of the brightness variation and Ca II (Ca II $\lambda 8542$ and Ca II H and K lines) index values (Figure 3), and this suggests that there is a rough positive correlation between the starspot coverage from *Kepler* photometric data and the stellar average magnetic field.

(iv) The results of (ii) and (iii) support the idea that the quasi-periodic brightness variation of *Kepler* solar-type superflare stars is caused by the rotation with large starspots.

(v) Lithium abundances of superflare stars suggest that *Kepler* solar-type superflare stars include many young stars but also include old stars like our Sun (Figure 4).

6.2. Summary of the Statistical Properties of Kepler Solar-type Superflare Stars Incorporating Gaia-DR2 Data

Then in Section 5, we investigated the statistical properties of *Kepler* solar-type superflare stars originally described in our previous studies (Maehara et al. 2012, 2015, 2017; Notsu et al. 2013b; Shibayama et al. 2013), by incorporating *Gaia*-DR2 stellar radius estimates (reported in Berger et al. 2018) and updating the parameters (e.g., flare energy, spot size).

(i) More than 40% of the original solar-type superflare stars in our previous studies are now classified as subgiant stars (Figure 5).

(ii) The bolometric energy released by flares (E_{flare}) is not inconsistent with the magnetic energy (E_{mag}) stored around the large starspots (Figures 6(b) and 11).

(iii) Our previous studies suggested that the maximum superflare energy in a given rotation period bin does not have a clear correlation with the rotation period, and superflares up to 10^{35} erg could occur on slowly rotating solar-type stars (Figure 12(a)). This study suggests that the maximum superflare energy continuously decreases as the rotation period increases (as the star becomes older; Figures 12(b) and 13). Superflares with energies $\lesssim 5 \times 10^{34}$ erg occur on old, slowly rotating Sun-like stars ($T_{\text{eff}} = 5600$–6000 K, $P_{\text{rot}} \sim 25$ days, and age $t \sim 4.6$ Gyr) approximately once every 2000–3000 yr (Figures 13(b) and 17). In contrast, superflares up to $\sim 10^{36}$ erg can occur on young, rapidly rotating stars ($P_{\text{rot}} \sim$ a few days and $t \sim$ a few hundred megayears; Figure 13), and the flare frequency of such young, rapidly rotating stars is ~ 100 times higher compared with the above old, slowly rotating Sun-like stars (Figures 14 and 16).

(iv) The maximum area of starspots does not depend on the rotation period and has a roughly constant or very gentle decreasing trend around $A_{\text{spot}} = 5 \times 10^{-2}$–$1 \times 10^{-1}A_{1/2\odot}$ ($A_{1/2\odot} \sim 3 \times 10^{22}$ cm^2: solar hemisphere) when the star is young and rapidly rotating. However, as the star becomes older and its rotation slows down, it starts to have a steep decreasing trend at a certain point: $P_{\text{rot}} \sim 12$ days ($t \sim 1.4$ Gyr) for the stars with $T_{\text{eff}} = 5600$–6000 K (Figure 15(b)), and $P_{\text{rot}} \sim 14$ days for the stars with $T_{\text{eff}} = 5100$–5600 K (Figure 15(a)). The maximum size of starspots on slowly rotating Sun-like stars is $\sim 1\%$ of the solar hemisphere, and this is enough for generating superflares with the energy $\lesssim 5 \times 10^{34}$ erg described in (iii).

(v) These decreasing trends of the maximum flare energy (in (iii)) and the maximum starspot area (in (iv)) can be related to each other since the superflare energy can be explained by the starspot magnetic energy as in (ii). However, there is also a difference between the two: the maximum area of starspots starts to steeply decrease at a certain P_{rot} value (as in (iv)), while the maximum flare energy continuously decreases as the rotation slows down (as in (iii)). This can suggest a possibility that the flare energy is determined not only by the starspot area but also by other important factors (e.g., spot magnetic structure).

(vi) The size distribution of starspots on Sun-like stars ($T_{\text{eff}} = 5600$–6000 K and $P_{\text{rot}} \sim 25$ days) between $A_{\text{spot}} = 10^{-2.5}A_{1/2\odot}$ and $10^{-1.0}A_{1/2\odot}$ is roughly located on the extension line of the distribution of sunspot groups between $A_{\text{spot}} = 10^{-3.25}A_{1/2\odot}$ and $10^{-2.5}A_{1/2\odot}$ (Figure 18).
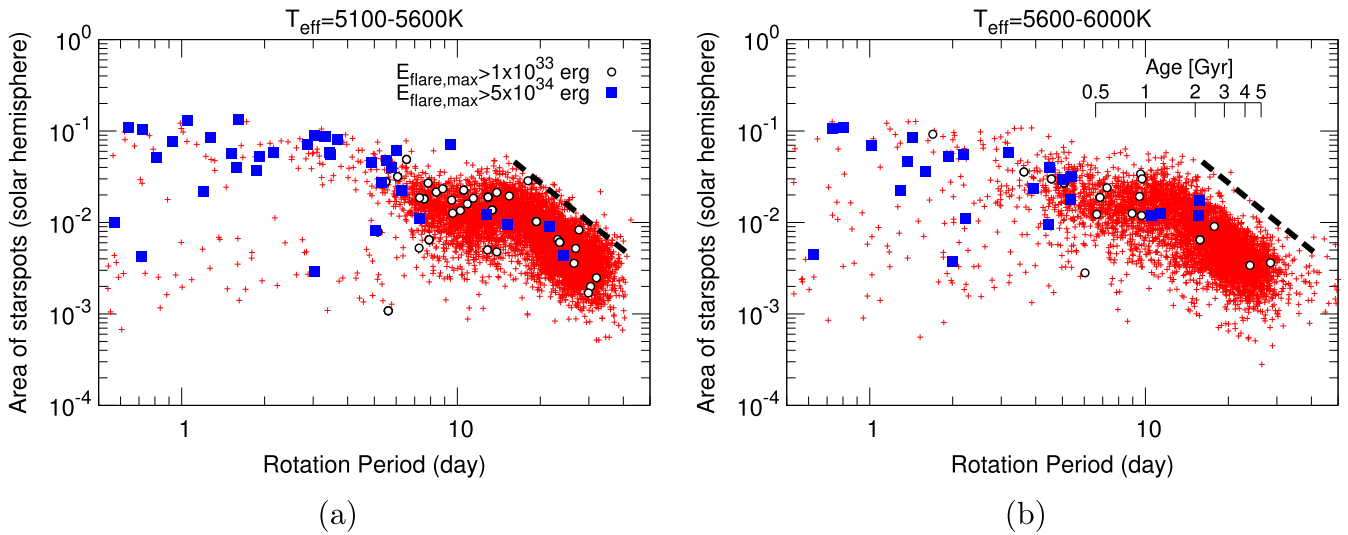
Figure 15. Scatter plot of the spot group area of solar-type stars (A_{spot}) as a function of the rotation period (P_{rot}), using the data updated with $T_{eff,DR25}$ and R_{Gaia} values in this study. The vertical axis represents A_{spot} in units of the area of solar hemisphere ($A_{1/2\odot} \sim 3 \times 10^{22}$ cm^2). Open circles and blue filled squares indicate solar-type stars that have superflares with the energy values of their most energetic flares $E_{flare,max} > 1 \times 10^{33}$ erg and $E_{flare,max} > 5 \times 10^{34}$ erg, respectively. Small red crosses indicate solar-type stars without superflares. The plotted data are separated on the basis of the temperature values: (a) $T_{eff} = 5100$–5600 K and (b) $T_{eff} = 5600$–6000 K. The black dashed line in panel (a) is plotted by eye to roughly show the upper limit of the data points in the range of $P_{rot} \gtrsim 14$ days. The black dashed line in panel (b) is plotted at the same place as in panel (a) in order for comparison with the results of panel (a). Only in panel (b) do we also add the scale of stellar age (t) on the basis of the gyrochronology relation of solar-type stars ($t \propto P_{rot}^{0.6}$; Ayres 1997; see Section 5.3 for details).
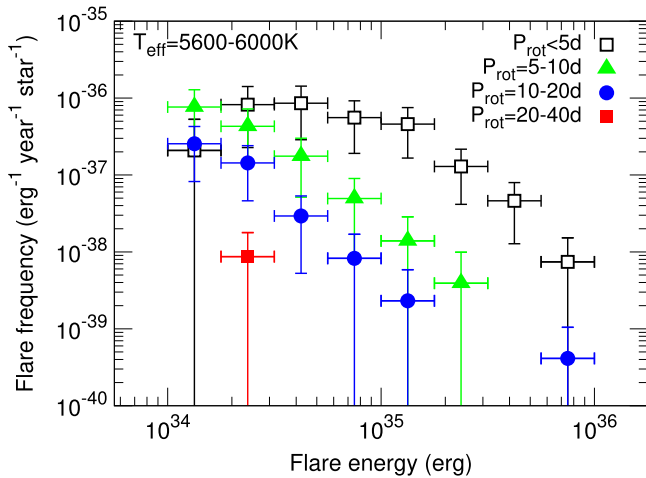
Figure 16. Occurrence frequency distribution of superflares on solar-type stars with $T_{eff} = 5600$–6000 K, using the superflare data that were originally found from *Kepler* 30-minute cadence data (Shibayama et al. 2013; Candelaresi et al. 2014) but are updated using $T_{eff,DR25}$ and R_{Gaia} in this study. The flare energy values in the horizontal axis are limited to 10^{34}–10^{36} erg since flare frequency in the range of $\lesssim 10^{34}$ erg can be heavily affected from the detection limit. The error bar in the horizontal axis direction corresponds to each energy bin. The vertical axis indicates the number of superflares per star, per year, and per unit energy in each energy bin. Error bars in the vertical axis represent 1σ uncertainty of the frequency estimated from $\sqrt{N+1}$ (N being the number of detected flares in each energy bin) considering Poisson statistics. Unlike the figures in our previous papers (e.g., Shibayama et al. 2013; Maehara et al. 2015), we do not take into account the error values of E_{flare} since this is now more reliable because of the *Gaia*-DR2 stellar radius values. The symbols are classified with rotation period (P_{rot}) values: open squares for $P_{rot} < 5$ days (age: $t < 0.5$ Gyr), green triangles for $P_{rot} = 5$–10 days ($t = 0.5$–1 Gyr), blue circles for $P_{rot} = 10$–20 days ($t = 1$–3.2 Gyr), and the red filled square for $P_{rot} = 20$–40 days ($t > 3.2$ Gyr). Age values here are taken from Figures 13(b) and 15(b).
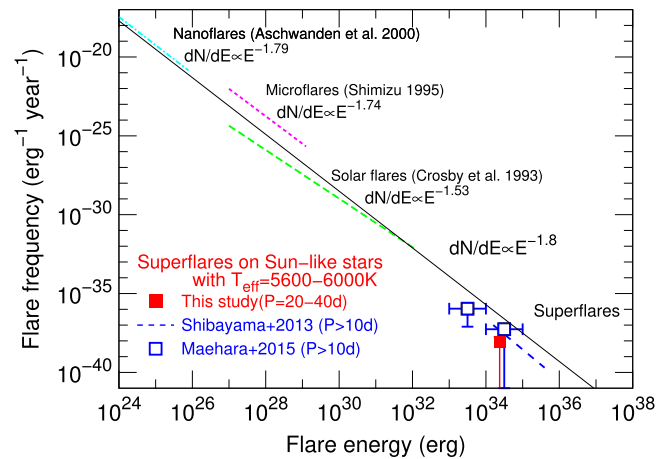
Figure 17. Comparison between the frequency distribution of superflares and solar flares. The red square, blue dashed line, and blue open squares indicate the occurrence frequency distributions of superflares on Sun-like stars (slowly rotating solar-type stars with $T_{eff} = 5600$–6000 K). The red square corresponds to the updated frequency value of superflares on the stars with $P_{rot} = 20$–40 days, which are calculated in this study and presented in Figure 16. Horizontal and vertical error bars are the same as those in Figure 16. For reference, the blue dashed line and blue open squares are the values of superflares on the stars with $P_{rot} > 10$ days, which we presented in Figure 4 of Maehara et al. (2015) on the basis of original superflare data using *Kepler* 30-minute cadence data (Shibayama et al. 2013) and 1-minute cadence data (Maehara et al. 2015), respectively. Definitions of error bars of the blue open squares are the same as those in Figure 4 of Maehara et al. (2015). Three dashed lines on the upper left side of this figure indicate the power-law frequency distribution of solar flares observed in hard X-ray (Crosby et al. 1993), soft X-ray (Shimizu 1995), and EUV (Aschwanden et al. 2000). Occurrence frequency distributions of superflares on Sun-like stars and solar flares are roughly on the same power-law line with an index of -1.8 (black solid line) for the wide energy range between 10^{24} and 10^{35} erg.
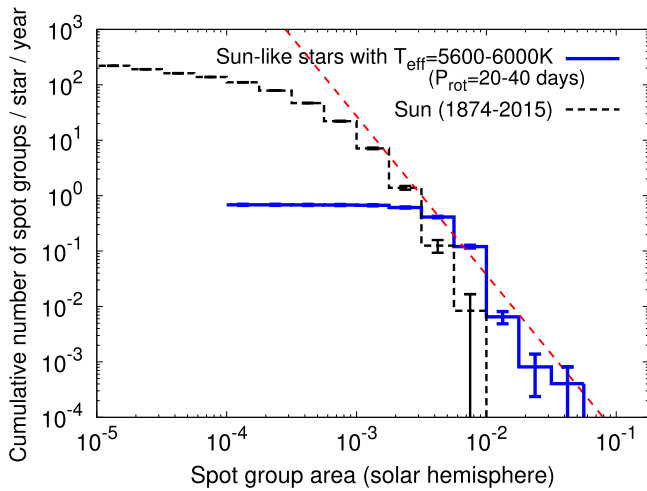
Figure 18. Comparison between the appearance frequency vs. spot area distribution of starspots on Sun-like stars and that of sunspot groups. Blue solid lines indicate the cumulative appearance frequency of starspots on Sun-like stars ($T_{\rm eff} = 5600$–6000 K and $P_{\rm rot} = 20$–40 days). The value is almost constant in the spot area range below $2 \times 10^{-3} A_{1/2\odot}$ ($A_{1/2\odot} \sim 3 \times 10^{22}$ cm^2), and this is because the brightness variations of the stars with small starspots could not be detected, as mentioned in Maehara et al. (2017). Black dashed lines indicate the cumulative appearance frequency of sunspot groups as a function of the maximum area of each sunspot group, which are exactly the same data presented in Figure 5 of Maehara et al. (2017; for details of the data description, see also Maehara et al. 2017). The vertical error bars of these two lines indicate the square root of the number of stars in each bin. The red dashed line represents the power-law fit to the frequency distribution of starspots in the spot area range of $10^{-2.5} A_{1/2\odot}$ to $10^{-1.0} A_{1/2\odot}$. The power-law index of the line is -2.9 ± 0.5.

The upper limit of starspot size values on slowly rotating Sun-like stars would be $\sim$a few $\times 10^{-2} A_{1/2\odot}$, and the appearance frequency of these spots is approximately once every 2000–3000 yr.

6.3. Future Prospects

In this paper, we have reported the current updates of our series of studies on superflares on solar-type stars. However, we need more studies to clarify the properties of superflare stars on Sun-like stars and to answer the important question, "Can our Sun have superflares?" For example, our spectroscopic observations so far have observed 64 solar-type superflare stars, but the number of Sun-like superflare stars ($T_{\rm eff} = 5600$–6000 K, $P_{\rm rot} \sim 25$ days, and $t \sim 4.6$ Gyr) that have been investigated spectroscopically and found to be "single" stars are now only a few ($\sim$1). In the figures in Section 5, the number of old, slowly rotating Sun-like superflare stars are now very small, and the current statistical discussions are not enough. In this study, as for superflares found from *Kepler* 30-minute cadence data, we only used the data originally found as solar-type superflare stars from *Kepler* data of the first $\sim$500 days (Quarter 0–6) in our previous study (Shibayama et al. 2013; Candelaresi et al. 2014). In our next study, we plan to increase the amount of data by using the whole *Kepler* data set of $\sim$1500 days (Quarter 0–17).[28] Moreover, the data from the next missions such as *TESS* (Ricker et al. 2015) and *PLATO* (Rauer et al. 2014) are expected to bring us more superflare

data on solar-type stars in the near future. These two missions are helpful also for spectroscopic follow-up observations of superflare stars since these two missions observe more nearby stars (with their wider spatial coverage), compared with *Kepler*.

In addition to the statistical properties of superflares that we discussed in this paper, there are so many topics that should be investigated in the near future to fully understand the physics of superflares and their effects in the related research fields, for example, mechanisms of white-light continuum emissions of superflares (e.g., Namekata et al. 2017; Heinzel & Shibata 2018; Kowalski & Allred 2018), chromospheric line profiles during superflares (e.g., Houdebine et al. 1993; Hawley et al. 2007; Honda et al. 2018), stellar mass ejections (e.g., CMEs) during superflares (e.g., Aarnio et al. 2012; Leitzinger et al. 2014; Hudson 2015; Osten & Wolk 2015; Harra et al. 2016; Takahashi et al. 2016; Vida et al. 2016; Moschou et al. 2017; Crosley & Osten 2018), the impacts of superflares on planets (e.g., Segura et al. 2010; Airapetian et al. 2016; Atri 2017; Lingam & Loeb 2017; Riley et al. 2018), detailed comparisons with a history of solar activity over $\sim$1000 yr (e.g., Miyake et al. 2012, 2013; Hayakawa et al. 2017a, 2017b; Usoskin 2017), quasi-periodic pulsations (QPPs) of the brightness during superflares (e.g., Pugh et al. 2016; McLaughlin et al. 2018), complexities of superflare-generating starspots (e.g., Maehara et al. 2017; Toriumi et al. 2017), how starspots are distributed on the surface of superflare stars (e.g., Doyle et al. 2018; Roettenbacher & Vida 2018), how starspots and plages are colocated in the case of active stars (e.g., Morris et al. 2018), and lifetimes and formation/decay processes of large starspots in solar-type stars (e.g., Shibata et al. 2013; Giles et al. 2017; Namekata et al. 2019). The superflare stars newly found from the above new missions (*TESS* and *PLATO*) would be helpful for the detailed observations to investigate these topics (e.g., spectroscopic or multiwavelength observations of superflares themselves, and long-term changes of stellar activities).

---

[28] We note that Davenport (2016) conducted the flare survey of F- to M-type stars using the whole *Kepler* 30-minute cadence data set, but their data are not necessarily enough for investigating flare stars with smaller frequency (e.g., slowly rotating Sun-like stars).

dpac/consortium). Funding for the DPAC has been provided by national institutions, in particular the institutions participating in the *Gaia* Multilateral Agreement.

Appendix A
Details of Analyses and Results of the APO 3.5 m Spectroscopic Observations

A.1. Binarity

For the first step of our analyses, we checked the binarity of each superflare star, as we did in Notsu et al. (2015a). First, we checked slit viewer images of the APO 3.5 m telescope. Two stars (KIC 11551430 and KIC 7093428) have visual companion stars, as shown in Figures 19(a) and 20(a).

As for KIC 11551430, we took spectra of both components (the brighter primary star, KIC 11551430A, and the fainter companion star, KIC 11551430B) of the visual binary system separately, as shown in Figures 19(b) and (c). We checked again pixel count data of superflare events on KIC 11551430 (Figures 19(d) and (e)), which are originally from Maehara et al. (2015), and confirmed that the center positions of the brightness during superflare events are roughly the same as those during quiescent state. This is consistent with the possibility that superflares occur on the primary star KIC 11551430A (see Figures S1 and S2 of Maehara et al. 2012).

As for KIC 7093428, we can see one primary brighter star (KIC 7093428A) and two fainter companion stars (KIC 7093428B and KIC 7093428C) in Figure 20(a). We only took spectra of the main brighter star (KIC 7093428A) as shown in Figure 20(b), since companions stars (B and C) are too faint. We also checked again pixel count data of superflare events on KIC 7093428 (Figures 20(c) and (d)), which are originally from Maehara et al. (2015). We can see that the center positions of the brightness during superflare events are shifted compared with those during quiescent state. This suggests the high possibility that superflares occur on the fainter companion stars KIC 7093428B or KIC 7093428C (see Figures S1 and S2 of Maehara et al. 2012), not on the primary G-type star KIC 7093428A. Then KIC 7093428 has "VB" in the second column of Table 1.

As described in Section 2, we selected 23 target stars and took spectra of 22 stars (minus the too faint target star KIC 10745663; K_p = 14.3 mag). Among the 22 observed stars, the data quality of our spectroscopic data of the fainter four stars (KIC 6032920, KIC 10528093, KIC 10646889, and KIC 9655134) is not high enough for the detailed following discussions. We plot examples of photospheric lines in

Figure 21 for reference. We only remark here that they do not show any clear signs of binarity, on the basis of Figure 21 and the slit viewer images of the APO 3.5 m telescope. In the following discussions of this paper, we only treat the 18 target stars that we got spectra of with enough S/N.

Next, we investigated the line profiles and found that two stars (KIC 11128041 and KIC 10338279) show double-lined profiles. In this process, we checked by eye the profiles of the many spectral lines, and the double-lined spectra of these two stars are shown in Figure 22. Since these double-lined profiles are caused by the overlap of the radiation of multiple stars, we regard these two stars as double-lined spectroscopic binary stars. These two stars have "SB2" in the second column of Table 1.

Third, we investigated time variations of the line profiles between the multiple observations that are expected to be caused by the orbital motion in the binary system. This investigation was for the target stars that we observed multiple times (16 stars). In Section 2, we already measured the RV of all the target stars that were not classified as visual binary stars or double-lined spectroscopic binary stars, and these values are listed in Table 2. We have also conducted spectroscopic observations of these four stars (KIC 4742436, KIC 4831454, KIC 9652680, and KIC 11610797) using the Subaru telescope (Honda et al. 2015; Notsu et al. 2015a, 2015b), and we also use these data in the RV investigation here (they are also listed in Table 2). As a result, KIC 11551430A, KIC 4543412, and KIC 11128041 show RV changes as shown in Figure 22, and these RV changes are large enough compared with RV errors of APO data ($\lesssim 1$ km s^{-1}). We confirmed this typical RV error value ($\lesssim 1$ km s^{-1}) by comparing our spectroscopic data of the single comparison stars that we observed multiple times in this study and are listed in Table 3. These three stars have "RV" in the second column of Table 1.

In total, we regard five superflare stars as binary stars among the 18 target stars of which we got spectra with enough S/N. The remaining 13 superflare stars do not show any evidence of binarity within the limits of our analyses, so we treat them as "single stars" in this paper. They have "no" in the second column of Table 1. Spectra of photospheric lines, including Fe I $\lambda\lambda$6212, 6215, 6216, and 6219 lines, of the 13 "single" superflare stars are shown in Figure 23. We observed nine stars among the 13 "single" stars multiple times, and we made co-added spectra of these nine stars by conducting the following two steps. First, we shifted the wavelength value of each spectrum to the laboratory frame on the basis of the RV value of each observation listed in Table 2. Next, we added up these shifted spectra to one co-added spectrum. The co-added spectra are mentioned as "comb" in Table 2, and only co-added spectra of these nine stars are used in Figure 23. Only the co-added spectra are used for the detailed analyses in the following sections of this paper, when we analyze the spectral data of the nine stars that we observed multiple times.
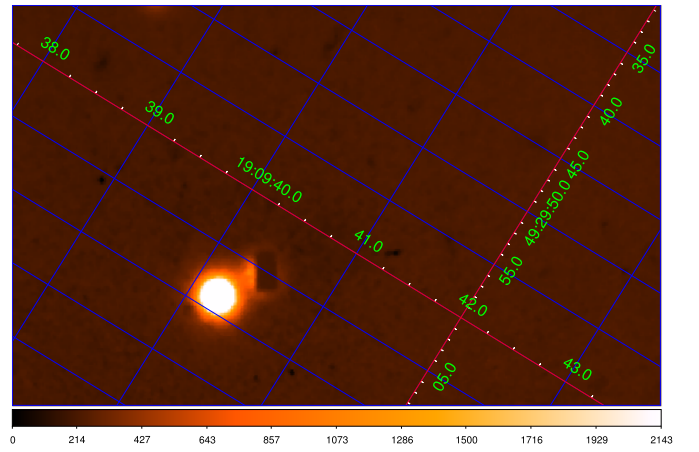
In addition to these nine "single" stars, we also made co-added spectra with the same methods for the two binary target stars (KIC 11551430A and KIC 4543412) that show RV shifts
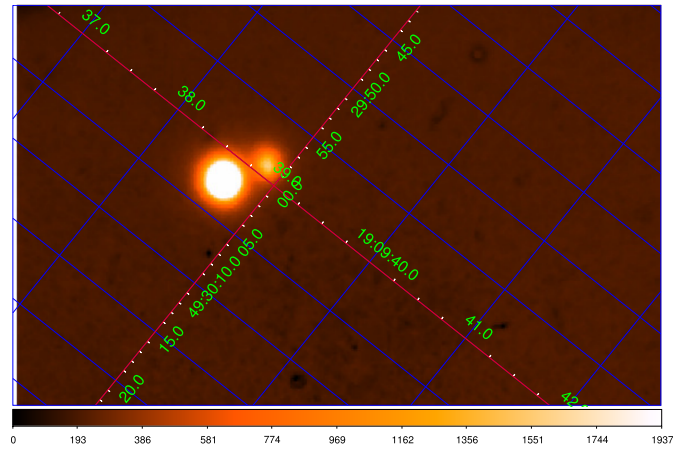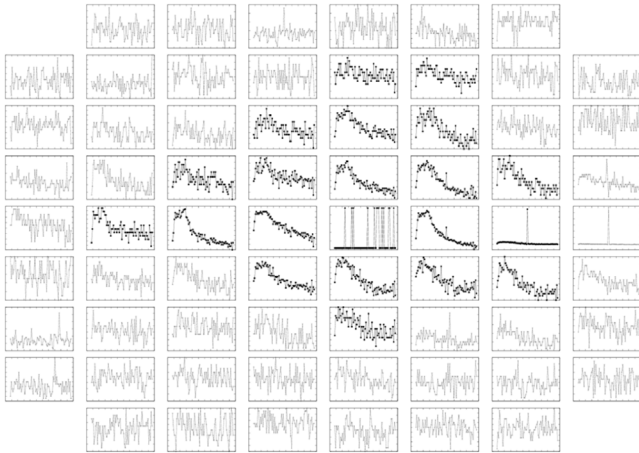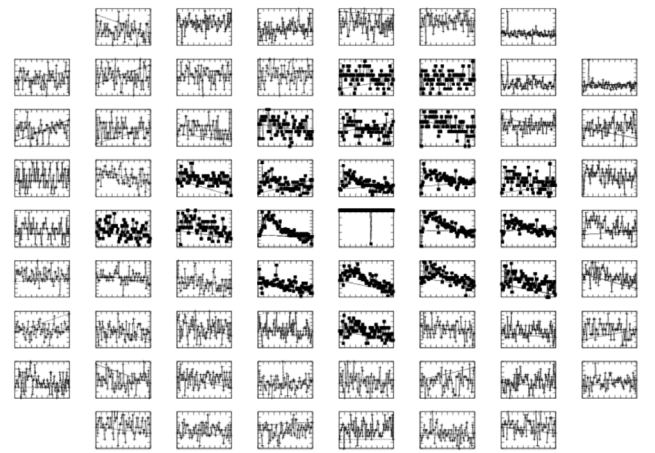
(a)
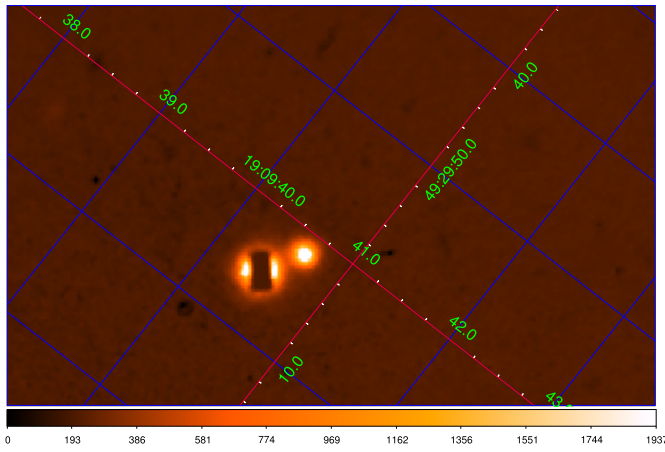
(b)

(c)

(d)

(e)

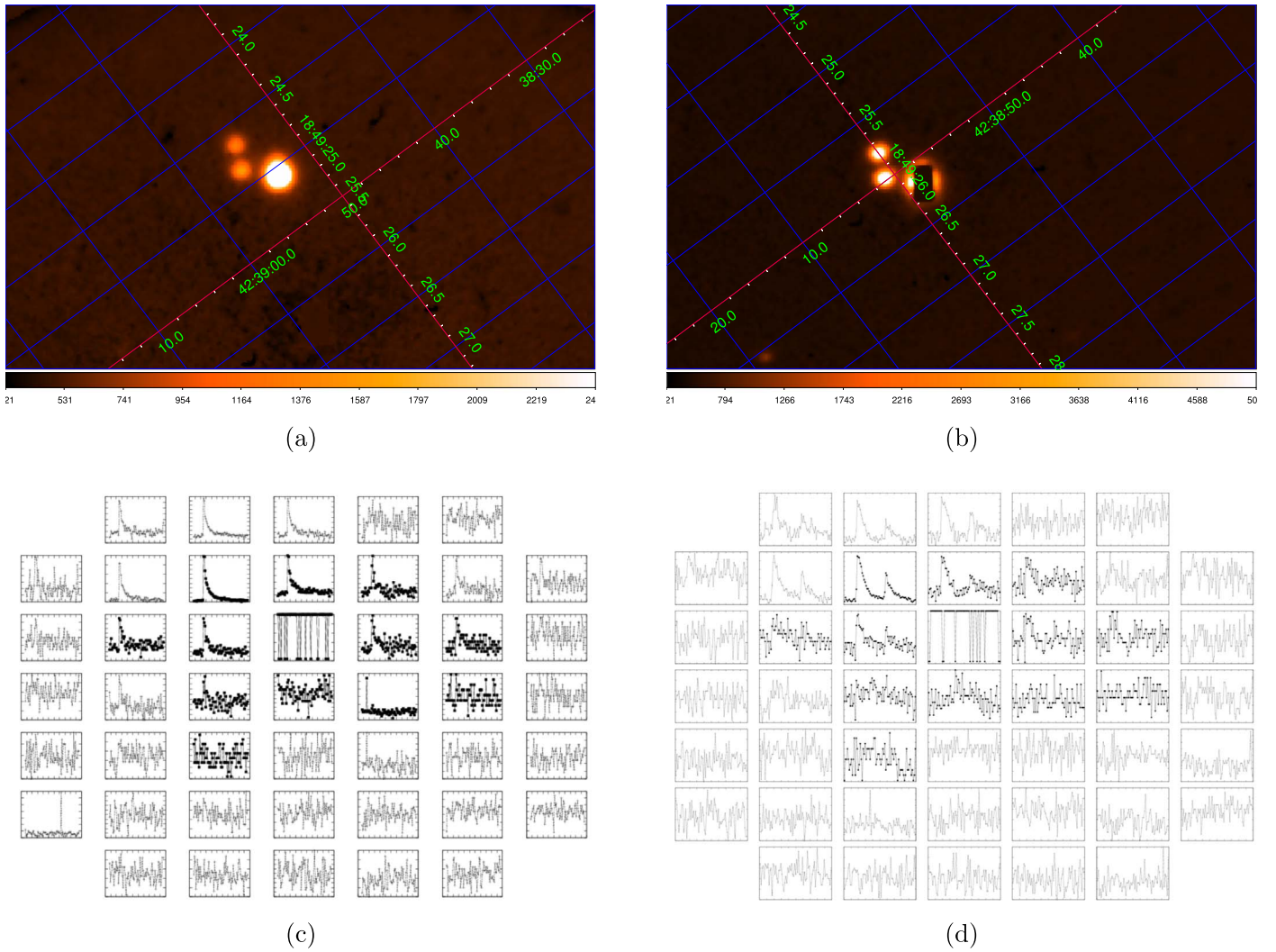**Figure 19.** (a)–(c) Slit viewer images of the visual binary target KIC 11551430. These images show that this star (the brighter primary star KIC 11551430A, for which we took spectroscopic data as in panel (b)) has a visually fainter companion star (KIC 11551430B, for which we took spectroscopic data as in panel (c)). (d, e) Pixel count data around two typical superflares on KIC 11551430 from the data of Maehara et al. (2015). The peak times (BJD [Barycentric Julian Date] −2,400,000) of flares in panels (d) and (e) are 55,019.673718 and 56,196.445193, and the estimated bolometric energies of them are 2.2×10^{35} erg and 2.8×10^{34} erg, respectively. The pixels in the center of the flares are saturated.

(a)

(b)

(c)

(d)

Figure 20. (a, b) Slit viewer images of the visual binary target KIC 7093428. These images show that this star (the brighter primary star KIC 7093428A, for which we took spectroscopic data as in panel (b)) has two fainter visual companion stars (KIC 7093428B and KIC 7093428C). (c, d) Pixel count data around two typical superflares on KIC 7093428 from the data of Maehara et al. (2015). The peak times (BJD –2,400,000) of flares in panels (c) and (d) are 55,102.453431 and 55,104.090097, and the estimated bolometric energies of them are 4.0×10^{34} erg and 1.1×10^{34} erg, respectively. The pixels in the center of the flares are saturated.

but do not show double-lined profiles. They are also shown in Figure 23. For reference, we also use these data when we estimate stellar parameters in the following.

A.2. Temperature, Surface Gravity, and Metallicity

We estimated the effective temperature $T_{\rm eff}$, surface gravity $\log g$, microturbulence $v_{\rm t}$, and metallicity [Fe/H] of the target superflare stars, by using the method that is basically the same as the one we have used in Notsu et al. (2015a, 2017). We measured the equivalent widths of $\sim$200 Fe I and Fe II lines and used the TGVIT program developed by Takeda et al. (2002, 2005). For reference, Rich et al. (2017) also applied this method to their ARCES spectroscopic data, which were taken with the same wavelength resolution value ($R \sim 32,000$) as our data, and they confirmed that the resultant values are consistent with the other previous studies. The resultant atmospheric parameters ($T_{\rm eff}$, $\log g$, $v_{\rm t}$, and [Fe/H]) are listed in Table 4.

We then compare these resultant atmospheric parameters with the values reported in DR25-KSPC (Mathur et al. 2017). We show the results in Figure 24, where the data points are classified with colors on the basis of the methods used to derive the parameters in DR25-KSPC. Our values seem to be in good agreement with the DR25-KSPC values, especially for $T_{\rm eff}$ (Figure 24(a)). $\log g$ has some dispersion (Figure 24(b)), but this small dispersion does not cause essential problems when we consider whether the target stars are main-sequence stars or not. As for [Fe/H], if we only consider the spectroscopic values in DR25-KSPC ("DR25-SPE" in Figure 24(c)), both values have better agreement, and the difference does not affect the overall discussions (e.g., whether the target stars are "metal-rich/poor" or not). Through this, we can remark that our spectroscopically derived values are good sources with which to discuss the actual properties of stars, as also mentioned for our previous Subaru spectroscopic data in Section 4.3 of Notsu et al. (2015a).
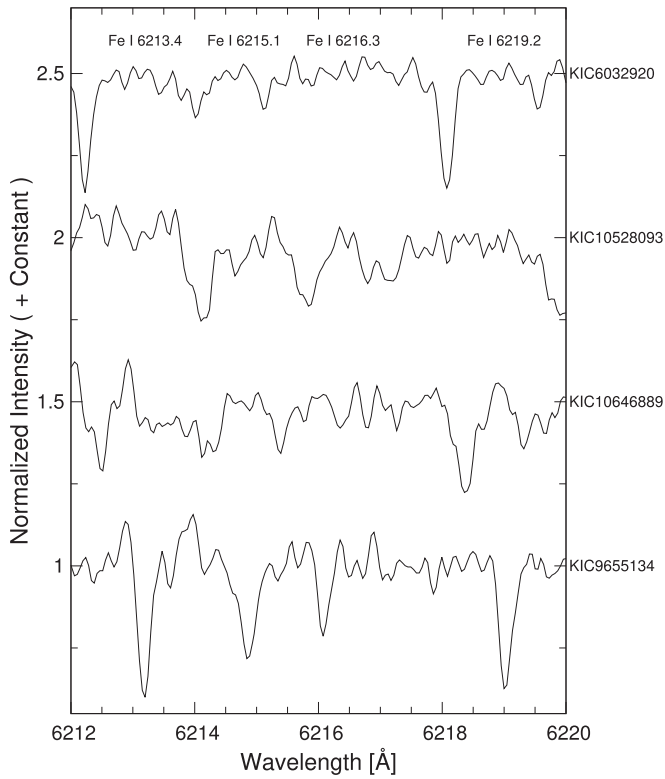
Figure 21. Example of photospheric absorption lines, including Fe I λλ6213, 6215, 6216, and 6219 lines, of the fainter four superflare stars (KIC 6032920, KIC 10528093, KIC 10646889, and KIC 9655134). The wavelength scale is adjusted to the heliocentric frame.
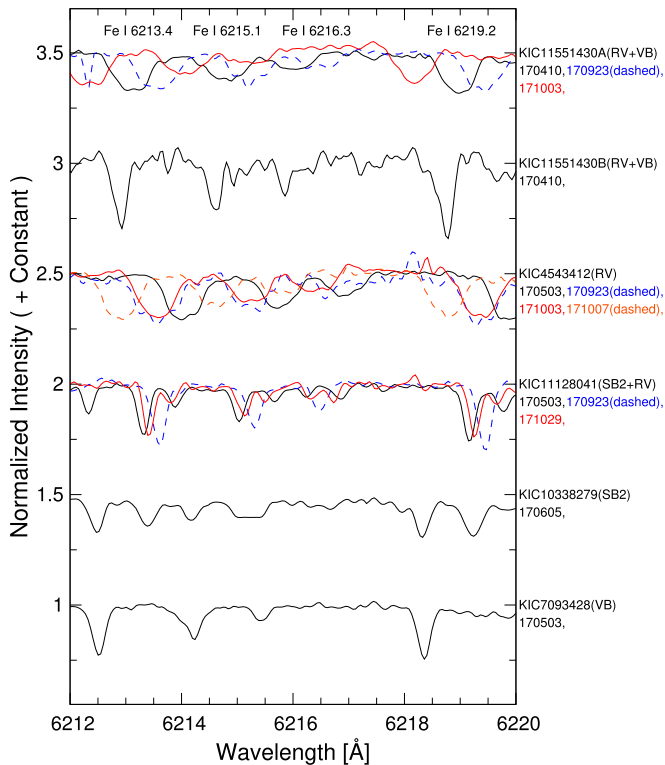

Figure 22. Example of photospheric absorption lines, including Fe I λλ6213, 6215, 6216, and 6219 lines, of superflare stars that we consider as spectroscopic binary stars. The wavelength scale is adjusted to the heliocentric frame. Numbers below each star name show observation dates (see Table 2).

A.3. Stellar Radius

As already listed in Table 1, we have stellar radius values R_{Gaia} of *Kepler* stars deduced from *Gaia*-DR2 parallax values (Berger et al. 2018). These values are listed again in Table 4, but five stars among our observed 18 target stars have no R_{Gaia} values reported in Berger et al. (2018).

In Figure 25 we compare these R_{Gaia} values with log g values estimated from our spectroscopic studies (Notsu et al. 2015a; this study). These two values are roughly correlated, and R_{Gaia} values look more sensitive to the boundary region between main-sequence stars and subgiants (around log $g = 4.0$–4.5 and $R_{Gaia} = 1.5$–$2.0\,R_\odot$). Then in Section 5, we mainly use these stellar radius R_{Gaia} values to strictly define main-sequence stars.

We also estimated stellar radius (R_{spec}) values from the stellar atmospheric parameters (T_{eff}, log g, and [Fe/H]), by applying the latest PARSEC isochrones (Bressan et al. 2012; Marigo et al. 2017).[29] In this process, we used basically the same method as the one used in our previous study (Notsu et al. 2015a). We selected all the data points that had possible sets of T_{eff}, log g, and [Fe/H] from the PARSEC isochrones, taking into account the error values of T_{eff} and log g (ΔT_{eff} and $\Delta \log g$). For the six stars that have no suitable isochrones within their original error range of T_{eff} and log g values, we then took into account larger error values as mentioned in footnote c of Table 4. We note that the resultant values of these six stars can have relatively low accuracy. We then selected the maximum and minimum R_{spec} value of each star and determined the resultant R_{spec} value as a median of the maximum and minimum values. The error values of R_{spec} listed in Table 4 are $\lesssim 20\%$ for most of the stars, as also mentioned in Notsu et al. (2015a).

In the following, we use R_{Gaia} values as a first priority, and we use R_{spec} values only for the stars without R_{Gaia} values.

A.4. Projected Rotation Velocity (v sin i)

We measured $v \sin i$ (stellar projected rotational velocity) of the target stars by using the method that is basically the same as that in our previous studies (Notsu et al. 2015a, 2017). This is originally based on the one described in Takeda et al. (2008). We took into account the effects of macroturbulence and instrumental broadening by considering a simple relationship among the line-broadening parameters (see Takeda et al. 2008), which can be expressed as

$$v_M^2 = v_{ip}^2 + v_{rt}^2 + v_{mt}^2. \tag{6}$$

Here v_M is the *e*-folding width of the Gaussian macrobroadening function $f(v) \propto \exp[(v/v_M)^2]$, including instrumental broadening (v_{ip}), rotation (v_{rt}), and macroturbulence (v_{mt}). We derived v_M by applying an automatic spectrum-fitting technique (Takeda 1995), assuming the model atmosphere corresponding to the atmospheric parameters estimated in Appendix A.2. In this process, we used the MPFIT program contained in the SPTOOL software package developed by Y. Takeda. We applied this fitting technique to the 6212–6220 Å region (shown in Figures 22 and 23) to derive $v \sin i$ values. This region has also been used in our previous studies (Notsu et al. 2015a, 2017).
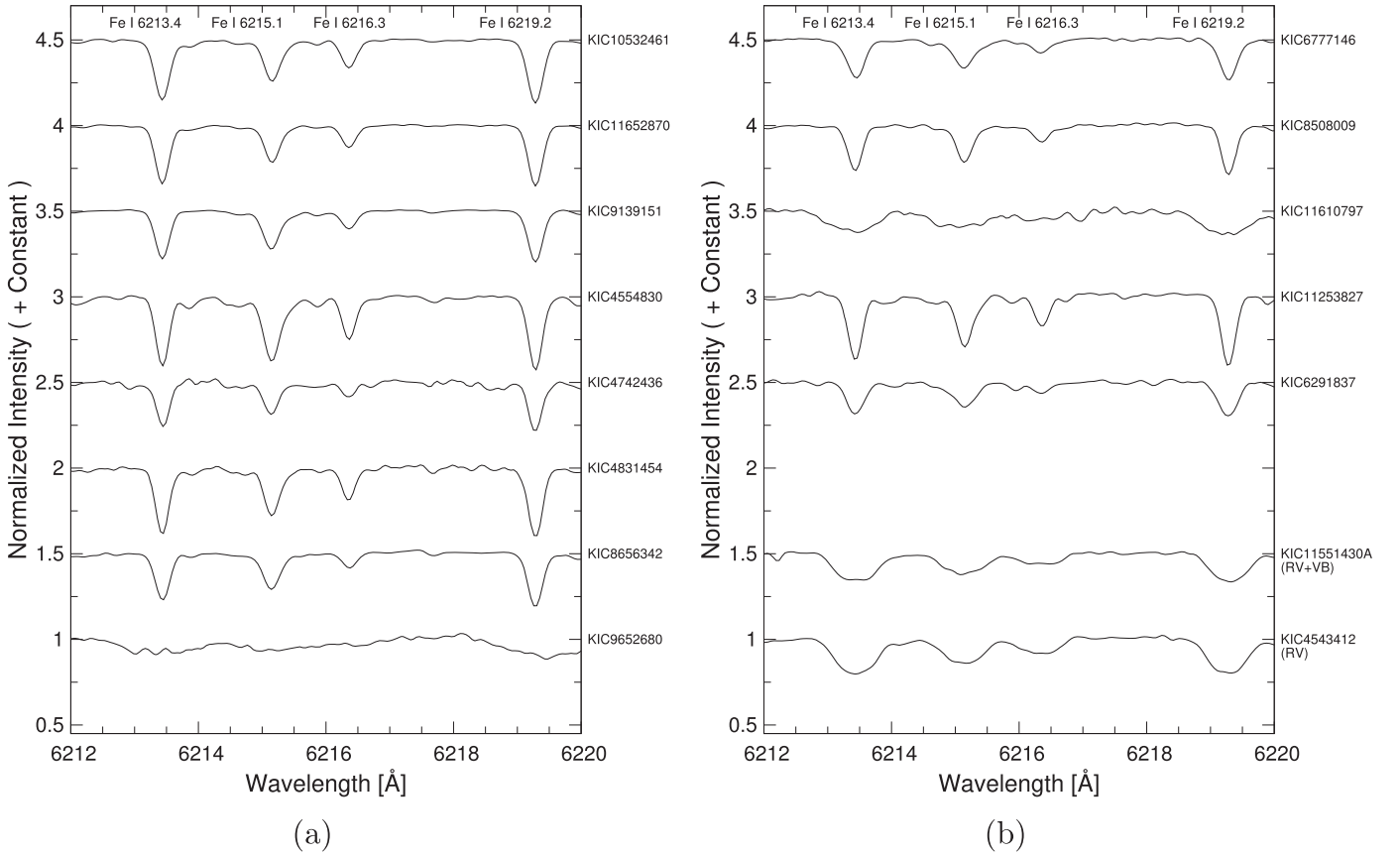
---

[29] http://stev.oapd.inaf.it/cgi-bin/cmd

Figure 23. Example of photospheric absorption lines, including Fe I $\lambda\lambda$6213, 6215, 6216, and 6219 lines. The wavelength scale of each spectrum is adjusted to the laboratory frame. In panel (a) and the upper part of panel (b), 13 "single" superflare stars that show no evidence of binarity are plotted. Co-added spectra are used here in case the star was observed multiple times (see Table 2). In the bottom of panel (b), the co-added spectra of the two binary stars KIC 11551430A and KIC 4543412, which only show RV shifts but do not show any double-lined profiles, are also plotted for reference.

The instrumental broadening velocity $v_{\rm ip}$ was calculated using the following equation (Takeda et al. 2008):

$$v_{\rm ip} = \frac{3 \times 10^5}{2R\sqrt{\ln 2}}, \qquad (7)$$

where $R(=\lambda/\Delta\lambda)$ is the wavelength resolution of the observation. For estimating the R value adopted here, we conducted Gaussian-fitting to emission lines in the 6180–6240 Å region of the Th–Ar spectrum data. This region is around the 6212–6220 Å region, where we conduct the above fitting process. We finally got $R = 32{,}500$, and we applied this to Equation (7) in the following. The macroturbulence velocity $v_{\rm rt}$ was estimated by using the relation $v_{\rm mt} \sim 0.42\xi_{\rm RT}$ (Takeda et al. 2008). The term $\xi_{\rm RT}$ is the radial-tangential macroturbulence, and $\xi_{\rm RT}$ was estimated using the relation reported in Valenti & Fischer (2005):

$$\xi_{\rm RT} = \left(3.98 - \frac{T_{\rm eff} - 5770\,{\rm K}}{650\,{\rm K}}\right). \qquad (8)$$

As we described in Notsu et al. (2015a), the choice of macroturbulence equation is often important, but we only use this Equation (8) to estimate the resultant values of this study, as we have also done in our previous studies (Notsu et al. 2015a, 2017). $v_{\rm rt}$ was then derived with the above equations, and we finally got $v\sin i$ with the relation $v_{\rm rt} \sim 0.94\, v\sin i$

(Gray 2005). The resultant $v\sin i$ values of the target superflare stars are listed in Table 4. As error values of $v\sin i$, we consider the systematic uncertainty with changing $\xi_{\rm RT}$ up to $\pm 25\%$, as described in Hirano et al. (2012).

The above estimation method of $v\sin i$ has been developed to be suitable for the Subaru/HDS spectroscopic data with the high spectral resolutions of $R \sim 55{,}000$–$100{,}000$ (Hirano et al. 2012; Notsu et al. 2013a, 2015a). It is not so appropriate that we apply this method without any modifications to our APO 3.5 m/ARCES spectroscopic data (the spectral resolution of only $\sim 32{,}500$). It is difficult to estimate $v\sin i$ values as low as 2–3 km s^{-1} only with APO spectra. On the other hand, in this study we do not need to estimate $v\sin i$ values with the high precision of 2–3 km s^{-1} for the overall discussions in this study with Figures 2 and 9 (e.g., whether $v\sin i \lesssim v_{\rm lc}$ is roughly achieved, and whether the target stars can have low inclination angle values or not). There are twice as many (or more) differences of the spectral resolution values between this APO observation and the previous Subaru/HDS observations (Hirano et al. 2012; Notsu et al. 2013a, 2015a), and the instrumental velocity $v_{\rm ip}$ has twice (or more) larger values between them. Then, in this study (e.g., Table 4) we only report a rough upper-limit value "$v\sin i < 4$ km s^{-1}" for the slowly rotating stars with $v\sin i < 4$ km s^{-1}. We also need to use the $v\sin i$ values of mildly slowly rotating stars ($v\sin i \sim 5$ km s^{-1}) with caution.
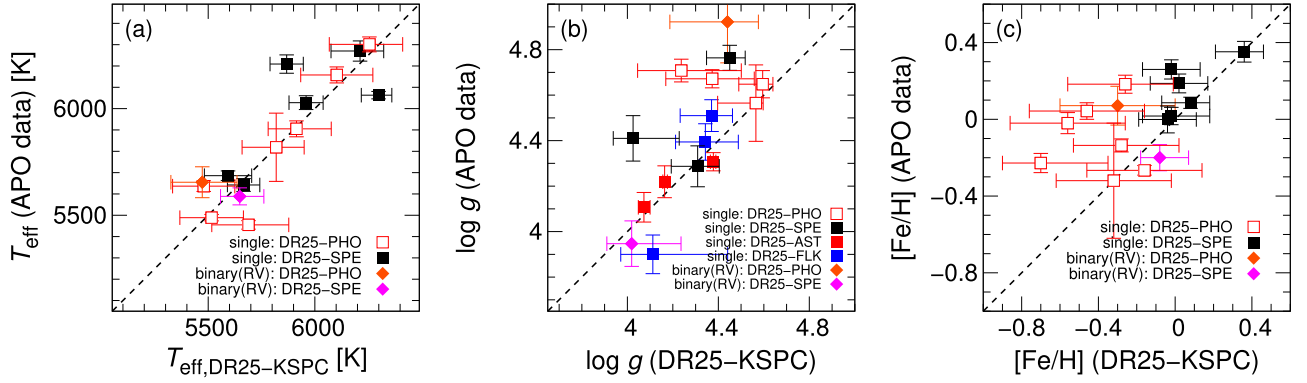
Figure 24. Comparison between the atmospheric parameters (T_{eff}, $\log g$, and [Fe/H]) that we estimated in this study and those reported in DR25-KSPC (Mathur et al. 2017), respectively. The squares are the target superflare stars classified as single stars in Appendix A.1, while the diamonds correspond to the spectra of binary superflare stars that do not show any double-lined profiles (KIC 11551430A and KIC 4543412). Colors show the methods used to derive the atmospheric parameters in DR25-KSPC (PHO: photometry; SPE: Spectroscopy; FLK: flicker method [see Bastien et al. 2016]; AST: Asteroseismolgy). See Mathur et al. (2017) for details of this classification.
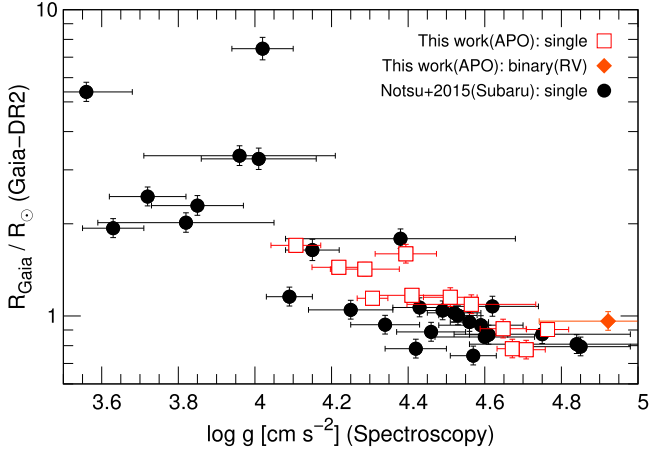
Figure 25. Stellar radius values R_{Gaia} from *Gaia*-DR2 parallaxes (Berger et al. 2018) as a function of $\log g$ estimated from our spectroscopic observations. Only the stars that have R_{Gaia} are included in this figure. The red open squares are the target superflare stars classified as single stars in Appendix A.1, and the orange diamonds correspond to the spectra of binary superflare stars that do not show any double-lined profiles (KIC 4543412). The single superflare stars that we investigated using the Subaru telescope (Notsu et al. 2015a, 2015b), excluding the four stars also investigated in this study (see footnote f of Table 1), are plotted with black circles.

A.5. Measurements of Stellar Activity Indicators Ca II λ8542 and Hα λ6563

The observed spectra of the target superflare stars around Ca II λ8542 and Hα λ6563 are shown in Figures 26 and 27, respectively. We measured the $r_0(8542)$ and $r_0(H\alpha)$ indices, which are the residual core fluxes normalized by the continuum level at the line cores of Ca II λ8542 and Hα λ6563, respectively. As we have already introduced in Notsu et al. (2013a), these indices are known to be indicators of stellar chromospheric activity (e.g., Linsky et al. 1979a; Takeda et al. 2010). As the chromospheric activity is enhanced, the intensity of these indicators becomes large since a greater amount of emission from the chromosphere fills in the core of the lines. The values of the $r_0(8542)$ and $r_0(H\alpha)$ indices of the target superflare stars are listed in Table 5. For reference, $r_0(8542)$ values of the 28 comparison stars are also listed in Table 3.

A.6. Measurements of Ca II H and K S-index

The observed spectra of the target superflare stars around Ca II H λ3968 and Ca II K λ3934 lines are shown in Figure 28. As described in Section 2, these spectra are normalized by using spectra of early-type standard stars, as also done in Morris et al. (2017). The emission in the cores of the Ca II H and K lines is a widely known indicator of the stellar chromospheric activity (e.g., Hall 2008 for review), and this is more sensitive to activity level changes compared with the Ca II λ8542 line (see Takeda et al. 2010, 2012). Ca II H and K emission is often measured as "S-index," which is the flux in the emission features normalized by two pseudocontinuum regions on either side of the absorption features (e.g., Vaughan et al. 1978; Duncan et al. 1991; Isaacson & Fischer 2010; Mittag et al. 2013; Karoff et al. 2016; Morris et al. 2017). We measured the S-index values of the target stars in the rest of this section.

The S-index value can vary among other instruments for the same intrinsic flux, as described in Section 2.1 of Isaacson & Fischer (2010). Following the method used in Isaacson & Fischer (2010) and Morris et al. (2017), we calibrated S-index values of our APO observation data (S_{APO}) against the S-index values already calibrated to the Mount Wilson Observatory (MWO) sample (S_{MWO}).[30] In this calibration process, we use our observation data of the 28 bright solar-type comparison stars described in Section 2 and listed in Table 3. All of these 28 stars have S-index values calibrated to the MWO sample (S_{MWO} values in Table 3) that are reported in Isaacson & Fischer (2010) on the basis of CPS program spectroscopic observations.

We first measured the S-index from our APO data (S_{APO}) of these comparison stars using the following equation (see Morris et al. 2017):

$$S_{APO} = \frac{aH + bK}{cR + dV}, \qquad (9)$$

where H and K are the recorded counts in 1.09 Å FWHM triangular bandpasses centered on the Ca II H and K lines at 3968.469 and 3933.663 Å, respectively. V and R are two

_____
[30] Morris et al. (2017) already conducted the calibration of S-index measurements for APO data, but most of their observed stars are K-type stars. Since S-index is a value also depending on stellar colors (Noyes et al. 1984), we newly conduct the calibration using solar-type (G-type main-sequence) stars in this study.
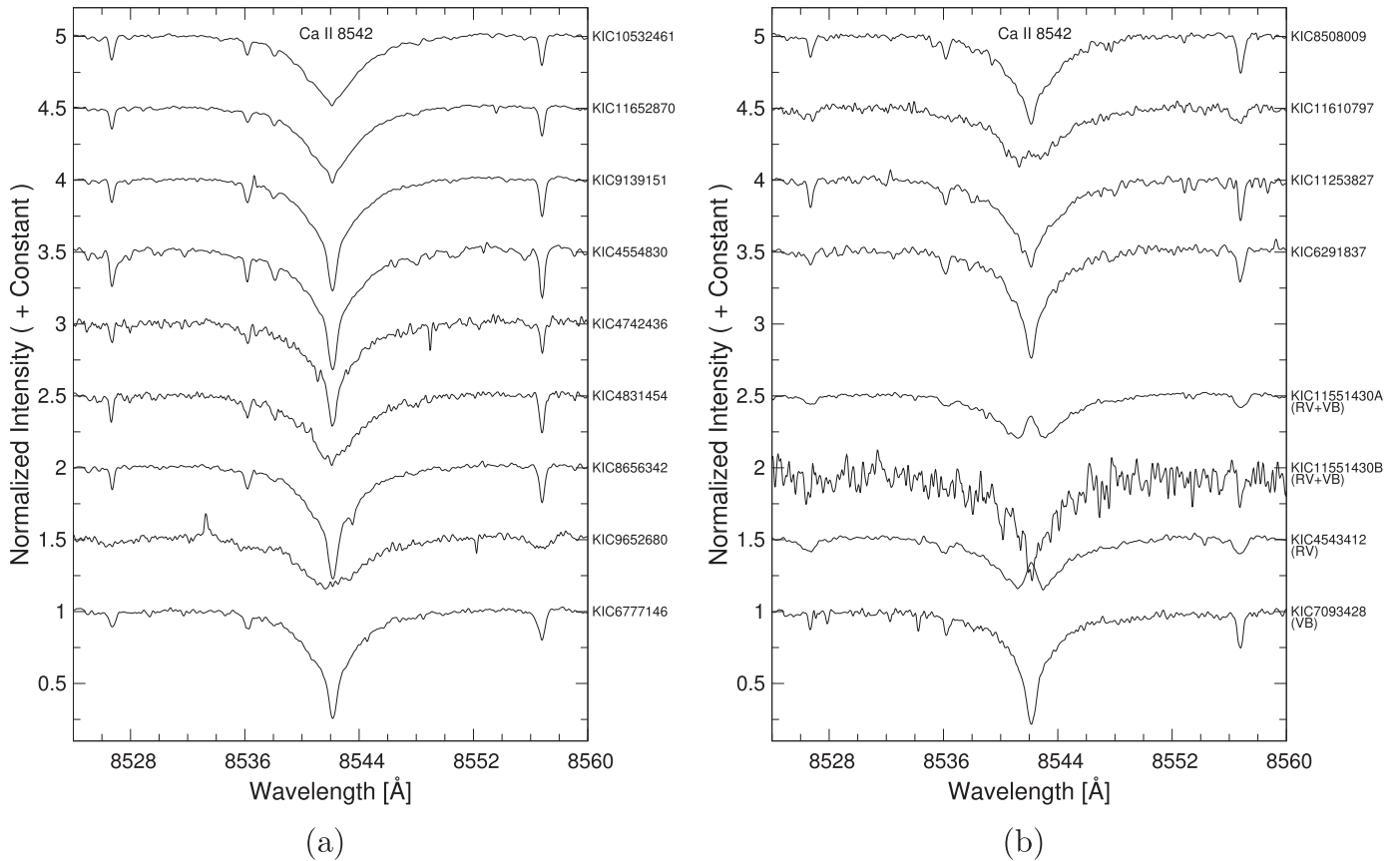
Figure 26. Spectra around the Ca II λ8542 line. The wavelength scale of each spectrum is adjusted to the laboratory frame. In panel (a) and the upper part of panel (b), 13 "single" superflare stars that show no evidence of binarity are plotted. Co-added spectra are used here in case the star was observed multiple times (see Table 2). In the bottom of panel (b), the spectra of binary stars that do not show any double-lined profiles are plotted for reference. As for KIC 11551430A and KIC 4543412 among them, which only show RV shifts, the co-added spectra are used.

20 Å wide reference bandpasses centered on 3901.07 and 4901.07 Å. The values of a, b, c, and d should be selected so that S_{APO} has roughly equal flux contribution from the H and K emission lines and roughly equal flux contribution from the R and V pseudocontinuum regions in the APO spectra. Here we finally had $a = b = c = d = 1$ after trial and error in this study.

Then in Figure 29, we compared these APO S-index values (S_{APO}) listed in Table 3 with the S_{MWO} values reported in Isaacson & Fischer (2010), and we investigated the two constants of the following equation (see Morris et al. 2017):

$$S_{MWO} = C_1 S_{APO} + C_2. \qquad (10)$$

Since S-index varies over time for each star in the sample, the linear correlation between S_{APO} and S_{MWO} can have some intrinsic spread as in Figure 29. Applying the least-squares method to the data in Figure 29, finally we got $C_1 = 22.005$ and $C_2 = 0.009$. Such larger (e.g., $C_1 \sim 22$) conversion factors of S-indices have commonly appeared in studies using a relatively high dispersion spectrograph, for example, Morris et al. (2017) using APO/ARCES data (the same instruments and same method as our study; $C_1 \sim 21.1$), Karoff et al. (2013) using NOT/FIES data ($R \sim 25,000$ and $C_1 \sim 16.6$), and Isaacson & Fischer (2010) using Keck/HIRES data ($R \sim 52,000$ and $C_1 \sim 31.5$). As described in the final paragraph of Section 3.6 of Karoff et al. (2013), the relatively

large C_1 value in our study can be mainly due to the higher spectral resolutions of APO data, compared with the original Mount Wilson observations (Duncan et al. 1991). Using Equations (9) and (10) and these C_1 and C_2 values, we finally estimated the calibrated S-index value of each spectrum ($S_{HK} \equiv S_{MWO}$) from each S_{APO} value. The S_{HK} values from the observations of comparison stars are listed in Table 3, and the resultant S_{HK} values of the target superflare stars from their spectral data (Figure 28) are listed in Table 5.

A.7. Measurements of Ca II H and K Flux

S-index is known to be stellar temperature dependent (e.g., Noyes et al. 1984), and it is a purely empirical quantity. Hence, it can be advantageous to calculate chromospheric fluxes. Then, in the following, we calculated Ca II H and K flux values from the S-index values with stellar colors, using the formulation described in Mittag et al. (2013). We summarize the method in the following.

The stellar surface fluxes emitted in the Ca II H and K lines ($\mathcal{F}_{HK}$) are expressed with S-index (S_{HK}) as

$$\mathcal{F}_{HK} = \frac{\mathcal{F}_{RV}}{\alpha} S_{HK}, \qquad (11)$$

where $\mathcal{F}_{RV}$ is the surface flux in both continua (V and R region mentioned in Appendix A.5) and the factor α is a historical dimensionless conversion factor. Following Mittag et al. (2013), we use the value $\alpha = 19.2$. $\mathcal{F}_{RV}$ is estimated from
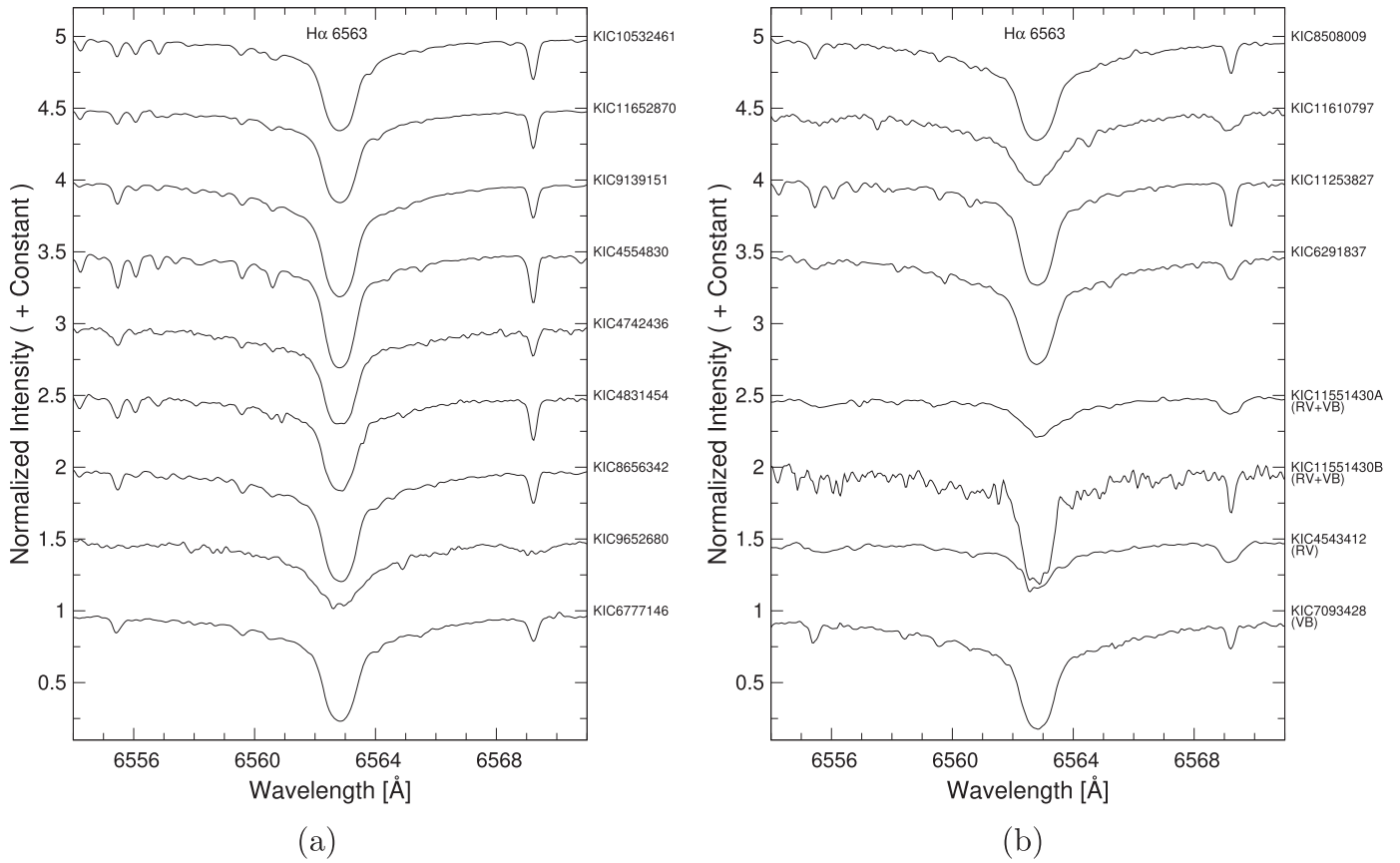
Figure 27. Spectra around the Hα $\lambda6563$ line. The wavelength scale of each spectrum is adjusted to the laboratory frame. In panel (a) and the upper part of panel (b), 13 "single" superflare stars that show no evidence of binarity are plotted. Co-added spectra are used here in case the star was observed multiple times (see Table 2). In the bottom of panel (b), the spectra of binary stars that do not show any double-lined profiles are plotted for reference. As for KIC 11551430A and KIC 4543412 among them, which only show RV shifts, the co-added spectra are used.

stellar color $B - V$ using the following empirical equation applicable to main-sequence and subgiant stars:

$$\log\left(\frac{\mathcal{F}_{\rm RV}}{19.2}\right) = 8.25 - 1.67(B - V). \qquad (12)$$

As for the target *Kepler* superflare stars in Table 4 and the 15 comparison stars (among all the 28 comparison stars) with remarks (1) or (2) in Table 3, which were observed in Notsu et al. (2017), $B - V$ values were calculated from $T_{\rm eff}$ and [Fe/H] using Equation (2) of Alonso et al. (1996). As for the remaining 13 stars, $B - V$ values reported in Table 1 of Isaacson & Fischer (2010) are used, and $T_{\rm eff}$ values used in the following are derived from $B - V$ values by using Equation (2) of Valenti & Fischer (2005).

We then estimated chromospheric excess flux of Ca II H and K lines ($\mathcal{F}'_{\rm HK}$) by subtracting the photospheric flux contribution ($\mathcal{F}_{\rm HK,phot}$) in the line center:

$$\mathcal{F}'_{\rm HK} = \mathcal{F}_{\rm HK} - \mathcal{F}_{\rm HK,phot}. \qquad (13)$$

$\mathcal{F}_{\rm HK,phot}$ were derived from $B - V$ by using the following equations in Mittag et al. (2013):

$$\log \mathcal{R}_{\rm HK,phot} = -4.898 + 1.918(B - V)^2$$
$$- 2.893(B - V)^3 \qquad (14)$$

$$\mathcal{R}_{\rm HK,phot} = \frac{\mathcal{F}_{\rm HK,phot}}{\sigma T_{\rm eff}^4}. \qquad (15)$$

$\mathcal{F}'_{\rm HK}$ is frequently converted to the flux-related stellar activity index $\log R'_{\rm HK}$ (Linsky et al. 1979b):

$$\mathcal{R}'_{\rm HK} = \frac{\mathcal{F}_{\rm HK} - \mathcal{F}_{\rm HK,phot}}{\sigma T_{\rm eff}^4} = \frac{\mathcal{F}'_{\rm HK}}{\sigma T_{\rm eff}^4}. \qquad (16)$$

With this normalization, we can compare the activity level of stars with different effective temperatures and colors. The resultant values of $\mathcal{F}'_{\rm HK}$ and $\mathcal{R}'_{\rm HK}$ of the target superflare stars are listed in Table 5.

Schrijver (1987) introduced the concept of "basal flux" ($\mathcal{F}_{\rm HK,basal}$), which is residual flux remaining in the core of the Ca II H and K lines of inactive stars after their photospheric line contribution ($\mathcal{F}_{\rm HK,phot}$) is removed. Mittag et al. (2013) investigated $\mathcal{F}'_{\rm HK}$ values of a very large number of main-sequence, subgiant, and giant stars and measured the "lower" boundary of the $\mathcal{F}'_{\rm HK}$ distribution as a function of $B - V$. Mittag et al. (2013) then reported the empirical scaling between $\mathcal{F}_{\rm HK,basal}$ and $B - V$:

$$\log \mathcal{F}_{\rm HK,basal} = a + b(B - V) + c(B - V)^2, \qquad (17)$$

where coefficients a, b, and c vary depending on $B - V$ and luminosity classes (V, IV, or III), and they are listed in Table 3 of Mittag et al. (2013). By subtracting this basal flux component $\mathcal{F}_{\rm HK,basal}$ from $\mathcal{F}'_{\rm HK}$, we can get new "pure" and
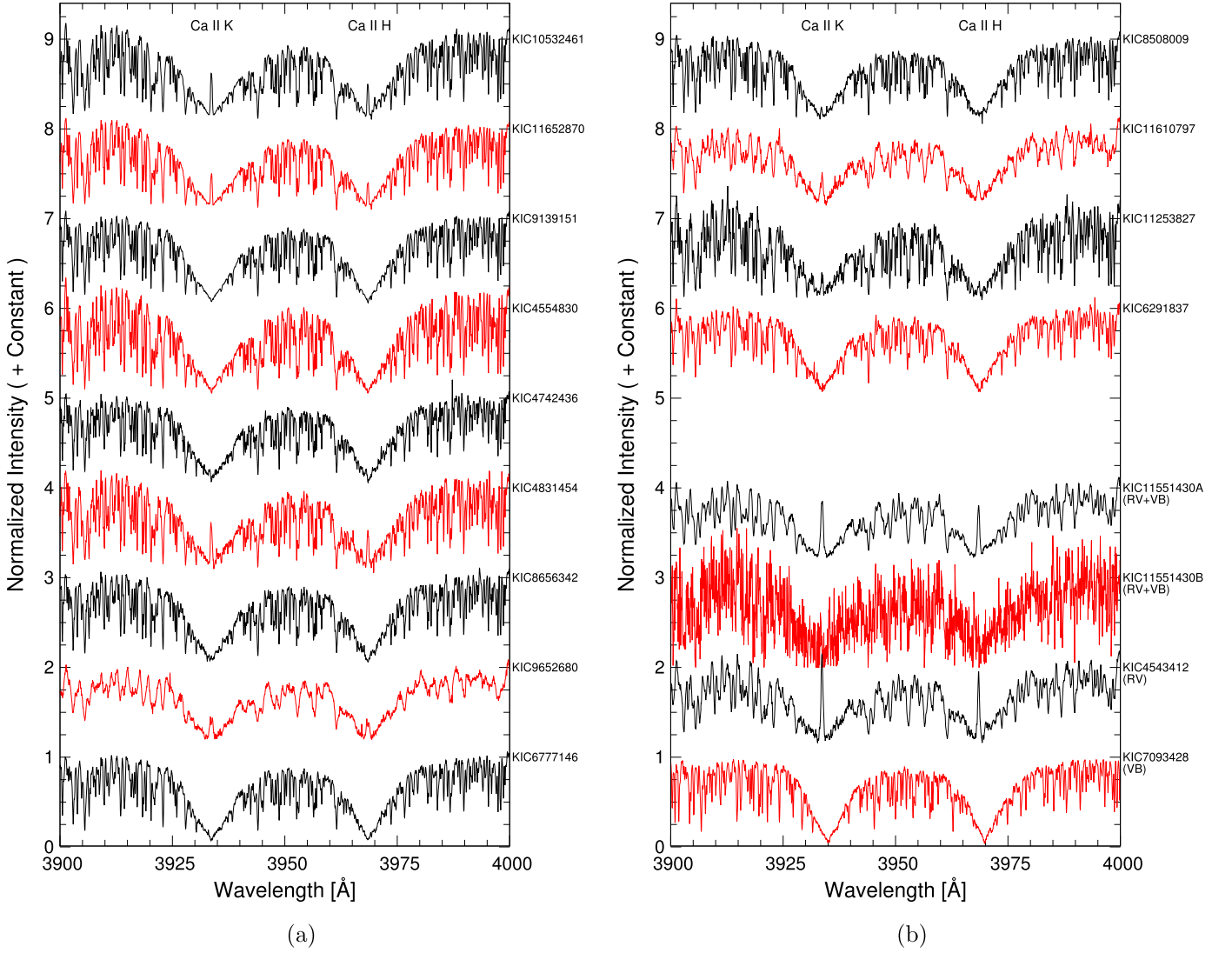
(a)

(b)

Figure 28. Spectra around Ca II H λ3968 and Ca II K λ3934 lines. The wavelength scale of each spectrum is adjusted to the laboratory frame. In panel (a) and the upper part of panel (b), 13 "single" superflare stars that show no evidence of binarity are plotted. Co-added spectra are used here in case the star was observed multiple times (see Table 2). In the bottom of panel (b), the spectra of binary stars that do not show any double-lined profiles are plotted for reference. As for KIC 11551430A and KIC 4543412 among them, which only show RV shifts, the co-added spectra are used. As for the spectra of KIC 6291837 and KIC 11551430B, data points heavily contaminated by cosmic-rays are removed to avoid confusion.
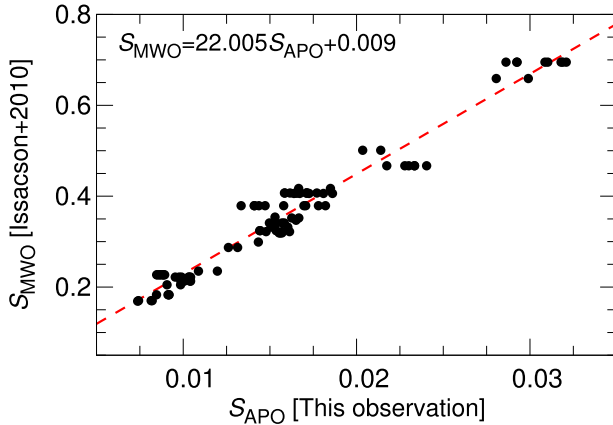
Figure 29. Calibration of S-index values measured from the APO data in this observation (S_{APO}) against the S-index values calibrated to the MWO sample (S_{MWO}). S_{APO} values in this figure are from the spectroscopic data of multiple observations of the 28 bright solar-type comparison stars (Table 3). S_{MWO} values are the values reported in Isaacson & Fischer (2010).

universal activity indicators $\mathcal{F}_{\mathrm{HK}}^{+}$ and $\log \mathcal{R}_{\mathrm{HK}}^{+}$ defined by

$$
\begin{aligned}
\mathcal{R}_{\mathrm{HK}}^{+} &= \frac{\mathcal{F}_{\mathrm{HK}}^{\prime} - \mathcal{F}_{\mathrm{HK,basal}}}{\sigma T_{\mathrm{eff}}^{4}} \\
&= \frac{\mathcal{F}_{\mathrm{HK}} - \mathcal{F}_{\mathrm{HK,phot}} - \mathcal{F}_{\mathrm{HK,basal}}}{\sigma T_{\mathrm{eff}}^{4}} \\
&= \frac{\mathcal{F}_{\mathrm{HK}}^{+}}{\sigma T_{\mathrm{eff}}^{4}}.
\end{aligned}
\tag{18}
$$

This $\log \mathcal{R}_{\mathrm{HK}}^{+}$ index allows comparisons of the activity levels of stars with different luminosity classes and different temperatures on the same scale (Mittag et al. 2013). The resultant values of $\mathcal{F}_{\mathrm{HK}}^{+}$ and $\mathcal{R}_{\mathrm{HK}}^{+}$ of the target superflare stars and the comparison stars are listed in Tables 5 and 3, respectively.

In Figures 30(a)–(c), we compared the resultant values of the Ca II H and K indices (S_{HK} index, $\log \mathcal{F}_{\mathrm{HK}}^{+}$ index, and $\log R_{\mathrm{HK}}^{+}$ index) with those of the $r_0(8542)$ index (normalized intensity at the center of the Ca II λ8542 line). As seen in these figures,

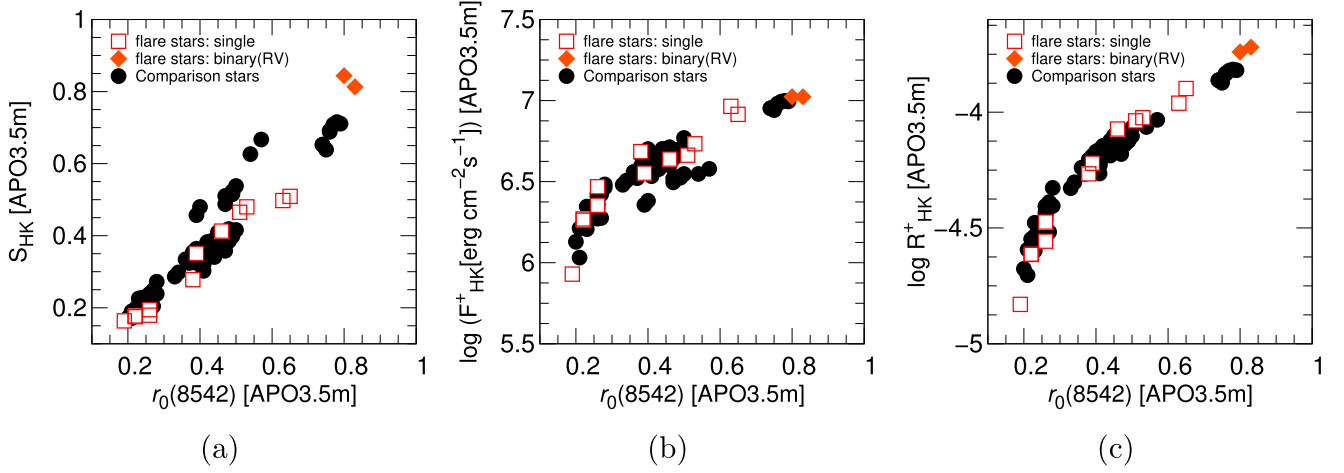**Figure 30.** (a) $r_0(8542)$ vs. S_{HK}; (b) $r_0(8542)$ vs. $\log \mathcal{F}^+_{\mathrm{HK}}$; (c) $r_0(8542)$ vs. $\log \mathcal{R}^+_{\mathrm{HK}}$. The red squares are the target superflare stars classified as single stars in Appendix A.1, and the orange diamonds correspond to the spectra of binary superflare stars that do not show any double-lined profiles (KIC 11551430A and KIC 4543412). Black circles show the values of comparison stars.
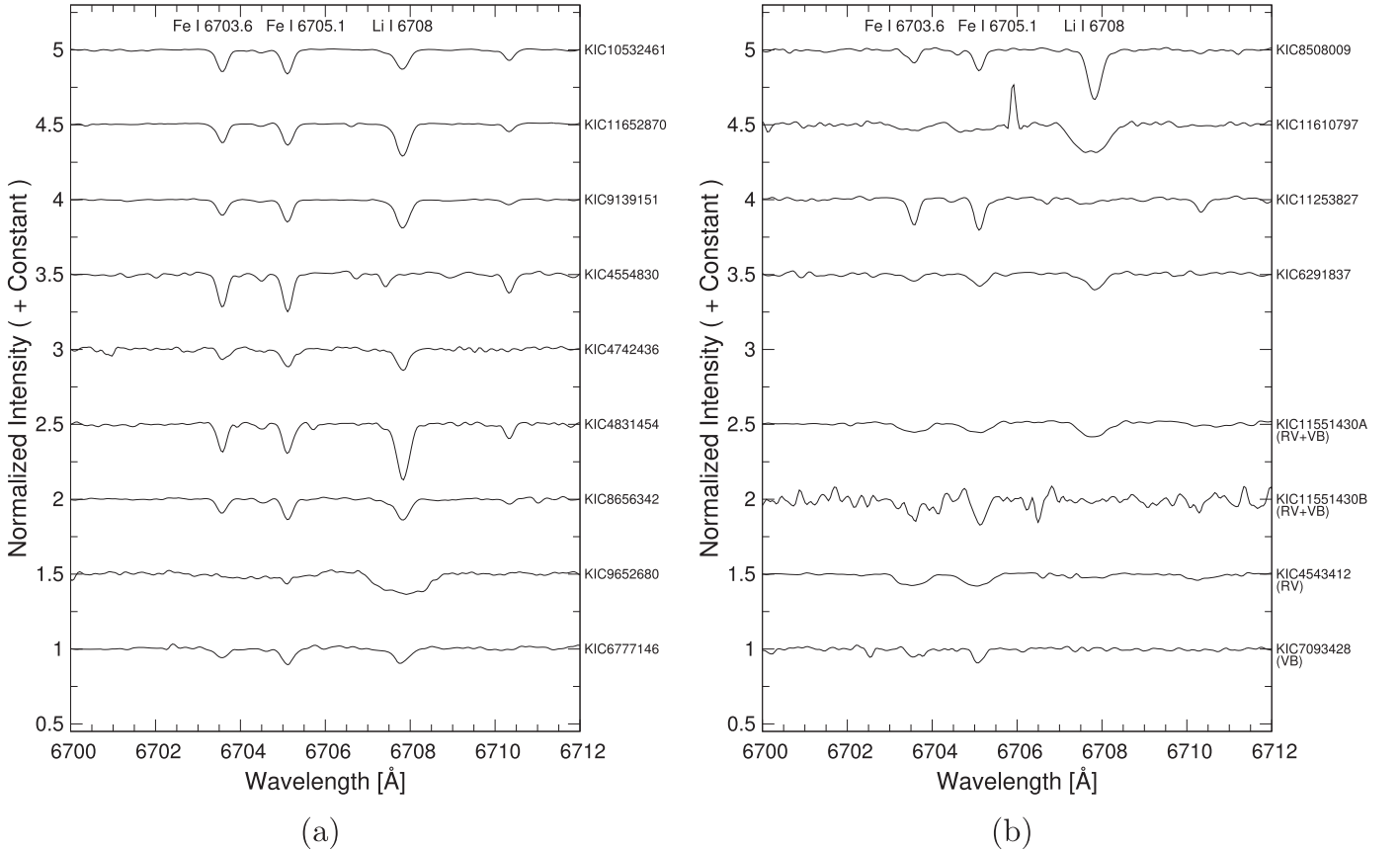

Figure 31. Spectra around the Li I $\lambda 6708$ line. The wavelength scale of each spectrum is adjusted to the laboratory frame. In panel (a) and the upper part of panel (b), 13 "single" superflare stars that show no evidence of binarity are plotted. Co-added spectra are used here in case the star was observed multiple times (see Table 2). In the bottom of panel (b), the spectra of binary stars that do not show any double-lined profiles are plotted for reference. As for KIC 11551430A and KIC 4543412 among them, which only show RV shifts, the co-added spectra are used.

Ca II $\lambda 8542$ index and Ca II H and K indices have good correlations also for *Kepler* solar-type superflare stars, as expected from the previous studies (e.g.,Takeda et al. 2012; Karoff et al. 2016). In particular, the $\log R^+_{\mathrm{HK}}$ index (Figure 30(c)) has the best correlation with the Ca II $\lambda 8542$ index among these three Ca II H and K indices. As for this $\log R^+_{\mathrm{HK}}$ index, stellar temperature (color) dependence and the contribution from photospheric/basal fluxes are removed (Equation (18)). In addition, Figure 30(c) might suggest that the $\log R^+_{\mathrm{HK}}$ index is much more sensitive to the difference in the lower activity level region ($r_0(8542) \lesssim 0.3$), compared with the $r_0(8542)$ index, as also suggested in Takeda et al.

(2012). Thus, we mainly use this $\log R_{\mathrm{HK}}^{+}$ index when we discuss the measurement results of Ca II H and K lines in Section 4.4.

A.8. Li Abundances

The observed spectra of the target superflare stars around the Li I λ6708 line are shown in Figure 31. We measured the Li abundances, A(Li), of the stars using these spectra and the atmospheric parameters estimated in Appendix A.2. We used an automatic profile-fitting method that is basically the same as in our previous studies (Honda et al. 2015; Notsu et al. 2017). This is originally based on the method described in Takeda & Kawanomoto (2005). We summarize the method in the following.

In the process of calculating A(Li), we used the MPFIT program contained in the SPTOOL software package also used above. We assumed local thermodynamic equilibrium (LTE) and derived Li abundances using the synthesis spectrum with interpolated model atmospheres taken from Kurucz (1993). We also assumed ^{6}Li/^{7}Li $= 0$ throughout this study. The line data around the Li I λ6708 region adapted here are the same as those used in Section 2.2 of Takeda & Kawanomoto (2005). The estimated A(Li) values of the target stars are listed in Table 4. For the stars where Li features are absent (e.g., below the detectable limit), we estimated the upper-limit values of A(Li) by applying the method that we described in Honda et al. (2015) and Notsu et al. (2017).

In Honda et al. (2015) and Notsu et al. (2017) we discussed the typical errors of Li abundances by considering errors arising from multiple causes (errors linked to atmospheric parameters, uncertainties arising from profile-fitting errors, and non-LTE effects). Since we conduct basically the same analyses as the above two papers, we here roughly assume that errors of A(Li) are $\sim$0.15 dex, as in Notsu et al. (2017).

Appendix B
Potential Differences between the Results from the *Kepler* Stars and Those from the "Real" Sample of Field Stars

As for Figure 15 in Section 5.4, we should note that there are many "inactive" stars with $A_{\mathrm{spot}} < 10^{-3}$ A$_{1/2\odot}$ ($A_{1/2\odot} \sim 3 \times 10^{22}$ cm^2: solar hemisphere). As shown in

Table 9, approximately 76% ((49,612–11,594)/49,612 = 37,618/49,212) of the solar-type stars are not plotted in Figure 15 since their brightness variation amplitude value is smaller than the detection limit. This also means that these $\sim$76% "inactive" solar-type stars have no P_{rot} values in our sample, and this can cause biases when we discuss the relations of the superflare properties with the rotation period. For example, in Figure 14 (in Section 5.3), flare frequency distribution in each P_{rot} bin is calculated by using the number of solar-type stars in each P_{rot} bin detected in McQuillan et al. (2014) (e.g., $N_P(P_{\mathrm{rot}} < 5$ days), $N_P(P_{\mathrm{rot}} = 5$–10 days), $N_P(P_{\mathrm{rot}} = 10$–20 days), and $N_P(P_{\mathrm{rot}} \geqslant 20$ days) in Table 9). However, it is possible that these N_P values do not show the actual P_{rot} distribution of field ordinary solar-type stars for the following two reasons: (1) The above "inactive" stars with no P_{rot} values are expected to be dominated by old, slowly rotating stars, and the real number fraction of slowly rotating stars to rapidly rotating stars (e.g., the fraction of $N_P(P_{\mathrm{rot}} \geqslant 20$ days) to the other $N_P(P_{\mathrm{rot}} < 5$ days), $N_P(P_{\mathrm{rot}} = 5$–10 days), and $N_P(P_{\mathrm{rot}} = 10$–20 days) values) can become larger than the values used for the calculations in this study (e.g., Figure 14). (2) In a strict sense, it might be possible that P_{rot} and the activity level distribution of *Kepler* stars can be (slightly) different from those of the field ordinary stars, because of the effects from the target selection (e.g., some active variables could be preferred in the Guest Observer programs).

In order to roughly evaluate the potential differences caused by the above points, we then roughly estimate the number fraction of solar-type stars in specific P_{rot} bins, by using the empirical gyrochronology relation (e.g., Mamajek & Hillenbrand 2008), which we have used in Maehara et al. (2017). The number of stars with $P_{\mathrm{rot}} \geqslant P_0$ ($N_{\mathrm{star}}(P_{\mathrm{rot}} \geqslant P_0)$) can be estimated from the duration of the main-sequence phase (τ_{MS}), the gyrochronological age of the star ($t_{\mathrm{gyro}}(P_0)$), and the total number of samples (N_{all}):

$$N_{\mathrm{star}}(P_{\mathrm{rot}} \geqslant P_0) = \left[1 - \frac{t_{\mathrm{gyro}}(P_0)}{\tau_{\mathrm{MS}}} \right] N_{\mathrm{all}}, \qquad (19)$$

assuming that the star formation rate around the *Kepler* field has been roughly constant over τ_{MS}. Using Equations (12)–(14) of Mamajek & Hillenbrand (2008), we roughly estimated the age values (t_{gyro}) of solar-type stars with $T_{\mathrm{eff}} \sim 5800$ and

Table 9
Number of Stars That Have P_{rot} and $\Delta F/F$ Values (N_P) Reported in McQuillan et al. (2014)

$T_{\mathrm{eff,DR25}}$	N_{data} [a]	N_P(all) [b]	$N_P(P_{\mathrm{rot}} < 5$ days) [c]	$N_P(P_{\mathrm{rot}} = 5$–10 days) [c]	$N_P(P_{\mathrm{rot}} = 10$–20 days) [c]	$N_P(P_{\mathrm{rot}} \geqslant 20$ days) [c]
5600–6000 K	28329	5065	314 (6.2%)	786 (15.5%)	2325 (45.9%)	1640 (32.4%)
5100–5600 K	20883	6529	175 (2.7%)	745 (11.4%)	2234 (34.2%)	3375 (51.7%)
5100–6000 K	49212	11594	489 (4.2%)	1531 (13.2%)	4559 (39.3%)	5015 (43.3%)

Notes.
[a] Number of all newly classified solar-type stars among the stars in McQuillan et al. (2014), by using $T_{\mathrm{eff,DR25}}$ and R_{Gaia} values.
[b] Number of stars that have P_{rot} and $\Delta F/F$ values reported in McQuillan et al. (2014).
[c] Subgroups of N_P categorized with P_{rot} values. The numbers in the parentheses are the fractions of $N_P(P_{\mathrm{rot}} < 5$ days), $N_P(P_{\mathrm{rot}} = 5$–10 days), $N_P(P_{\mathrm{rot}} = 10$–20 days), and $N_P(P_{\mathrm{rot}} > 20$ days) to N_P(all), respectively.

Table 10
P_{rot} Distribution of Field Ordinary Solar-type Stars Estimated from the Gyrochronological Relation (See Equation (19))

$T_{\mathrm{eff,DR25}}$	$N_{\mathrm{star}}(P_{\mathrm{rot}} < 5$ days)/N_{all}	$N_{\mathrm{star}}(P_{\mathrm{rot}} = 5$–10 days)/$N_{\mathrm{all}}$	$N_{\mathrm{star}}(P_{\mathrm{rot}} = 10$–20 days)/$N_{\mathrm{all}}$	$N_{\mathrm{star}}(P_{\mathrm{rot}} \geqslant 20$ days)/N_{all}
5800 K	3% (<0.26 Gyr)	6% (0.26–0.89 Gyr)	21% (0.89–3.0 Gyr)	70% (⩾3.0 Gyr)
5350 K	2% (<0.17 Gyr)	4% (0.17–0.59 Gyr)	14% (0.59–2.0 Gyr)	80% (⩾2.0 Gyr)

5350 K ($B - V \sim 0.63$ and 0.78 from Equation (2) of Valenti & Fischer 2005) and $P_{\rm rot} \sim 5$, 10, and 20 days, as listed in the parentheses in Table 10. Using these $t_{\rm gyro}$ values and Equation (19), we estimated the number fraction of stars with $P_{\rm rot} < 5$ days, 5–10 days, 10–20 days, and $\geqslant 20$ days as listed in Table 10. As a result, there are differences between the number fractions of slowly/rapidly rotating stars in the *Kepler* sample from McQuillan et al. (2014) (Table 9) and those estimated from the gyrochronology relation (Table 10). For example, the number fraction of $P_{\rm rot} \geqslant 20$ days among all the sample stars with $T_{\rm eff} = 5600$–6000 K has a roughly factor of two difference: $N_P(P_{\rm rot} \geqslant 20\,{\rm days})/N_P({\rm all}) \sim 32\%$ (Table 9) and $N_{\rm star}(P_{\rm rot} \geqslant 20\,{\rm days})/N_{\rm all} \sim 70\%$ (Table 10). This means that the flare frequency value of $T_{\rm eff} = 5600$–6000 K and $P_{\rm rot} \geqslant 20$ days in Figure 14 can become a factor of two smaller than the real value. We must note these potential errors of our study, and the exact values of the flare frequency estimated from our analyses should be treated with caution. However, the overall dependences (e.g., the results that flare frequency clearly depends on the rotation period) do not change, and the differences are much smaller than one order of magnitude. Moreover, the estimates from the gyrochronology can also include several errors. One example is that the age–rotation relation (gyrochronology relation) of young (e.g., $t \lesssim 0.5$–0.6 Gyr) and old (e.g., $t > 5.0$ Gyr) solar-type stars can have a large scatter (e.g., Soderblom et al. 1993; Ayres 1997; Tu et al. 2015) and breakdown (van Saders et al. 2016; Metcalfe & Egeland 2018), respectively, as we have also mentioned in Section 5.3. We also assumed that the star formation rate around the *Kepler* field has been roughly constant over $\tau_{\rm MS}$ in the above estimation, but this assumption is not necessarily correct. Because of these points, more investigations on the above potential differences (as large as a factor of two or three) between the results from the *Kepler* stars and those from the "real" sample of field stars are beyond the scope of this paper, and we expect future studies using new data (e.g., *TESS* data mentioned in Section 6.3). We note again here that we should keep in mind these potential errors when discussing the relation of superflare frequency with the rotation period (e.g., Figure 14 in Section 5.3 and Figures 16 and 17 in Section 5.5).

ORCID iDs

Yuta Notsu ● https://orcid.org/0000-0002-0412-0849
Hiroyuki Maehara ● https://orcid.org/0000-0003-0332-0811
Suzanne L. Hawley ● https://orcid.org/0000-0002-6629-4182
James R. A. Davenport ● https://orcid.org/0000-0002-0637-835X
Kosuke Namekata ● https://orcid.org/0000-0002-1297-9485
Shota Notsu ● https://orcid.org/0000-0003-2493-912X

References

Aarnio, A. N., Matt, S. P., & Stassun, K. G. 2012, ApJ, 760, 9
Airapetian, V. S., Glocer, A., Gronoff, G., Hébrard, E., & Danchi, W. 2016, NatGe, 9, 452
Alonso, A., Arribas, S., & Martinez-Roger, C. 1996, A&A, 313, 873
Aschwanden, M. J., Tarbell, T. D., Nightingale, R. W., et al. 2000, ApJ, 535, 1047
Atri, D. 2017, MNRAS, 465, L34
Aulanier, G., Démoulin, P., Schrijver, C. J., et al. 2013, A&A, 549, A66
Ayres, T. R. 1997, JGR, 102, 1641
Baliunas, S. L., Donahue, R. A., Soon, W. H., et al. 1995, ApJ, 438, 269
Balona, L. A. 2015, MNRAS, 447, 2714
Bastien, F. A., Stassun, K. G., Basri, G., & Pepper, J. 2016, ApJ, 818, 43
Benomar, O., Bazot, M., Nielsen, M. B., et al. 2018, Sci, 361, 1231
Benz, A. O., & Güdel, M. 2010, ARA&A, 48, 241
Berdyugina, S. V. 2005, LRSP, 2, 8
Berger, T. A., Huber, D., Gaidos, E., & van Saders, J. L. 2018, ApJ, 866, 99
Bogdan, T. J., Gilman, P. A., Lerche, I., & Howard, R. 1988, ApJ, 327, 451
Bressan, A., Marigo, P., Girardi, L., et al. 2012, MNRAS, 427, 127
Brown, T. M., Latham, D. W., Everett, M. E., & Esquerdo, G. A. 2011, AJ, 142, 112
Candelaresi, S., Hillier, A., Maehara, H., Brandenburg, A., & Shibata, K. 2014, ApJ, 792, 67
Chang, H.-Y., Lin, C.-L., Ip, W.-H., et al. 2018, ApJ, 867, 78
Crosby, N. B., Aschwanden, M. J., & Dennis, B. R. 1993, SoPh, 143, 275
Crosley, M. K., & Osten, R. A. 2018, ApJ, 856, 39
Davenport, J. R. A. 2016, ApJ, 829, 23
Doyle, L., Ramsay, G., Doyle, J. G., Wu, K., & Scullion, E. 2018, MNRAS, 480, 2153
Duncan, D. K., Vaughan, A. H., Wilson, O. C., et al. 1991, ApJS, 76, 383
Eastwood, J. P., Biffis, E., & Hapgood, M. A. 2017, Risk Analysis, 37, 2
Emslie, A. G., Dennis, B. R., Shih, A. Y., et al. 2012, ApJ, 759, 71
Gershberg, R. E. 2005, Solar-type Activity in Main-sequence Stars (Springer: Berlin)
Giles, H. A. C., Collier Cameron, A., & Haywood, R. D. 2017, MNRAS, 472, 1618
Gizis, J. E., Burgasser, A. J., Berger, E., et al. 2013, ApJ, 779, 172
Gray, D. F. 2005, The Observation and Analysis of Stellar Photospheres (3rd ed.; Cambridge: Cambridge Univ. Press)
Güdel, M. 2007, LRSP, 4, 3
Hall, J. C. 2008, LRSP, 5, 2
Harra, L. K., Schrijver, C. J., Janvier, M., et al. 2016, SoPh, 291, 1761
Hawley, S. L., Davenport, J. R. A., Kowalski, A. F., et al. 2014, ApJ, 797, 121
Hawley, S. L., Walkowicz, L. M., Allred, J. C., & Valenti, J. A. 2007, PASP, 119, 67
Hayakawa, H., Iwahashi, K., Ebihara, Y., et al. 2017a, ApJL, 850, L31
Hayakawa, H., Tamazawa, H., Uchiyama, Y., et al. 2017b, SoPh, 292, 12
Heinzel, P., & Shibata, K. 2018, ApJ, 859, 143
Hirano, T., Sanchis-Ojeda, R., Takeda, Y., et al. 2012, ApJ, 756, 66
Honda, S., Notsu, Y., Maehara, H., et al. 2015, PASJ, 67, 85
Honda, S., Notsu, Y., Namekata, K., et al. 2018, PASJ, 70, 62
Houdebine, E. R., Foing, B. H., Doyle, J. G., & Rodono, M. 1993, A&A, 274, 245
Huber, D., Silva Aguirre, V., Matthews, J. M., et al. 2014, ApJS, 211, 2
Hudson, H. S. 2015, J. Phys. Conf. Ser., 632, 012058
Isaacson, H., & Fischer, D. 2010, ApJ, 725, 875
Jackman, J. A. G., Wheatley, P. J., Pugh, C. E., et al. 2018, MNRAS, 477, 4655
Karoff, C., Knudsen, M. F., De Cat, P., et al. 2016, NatCo, 7, 11058
Karoff, C., Metcalfe, T. S., Chaplin, W. J., et al. 2013, MNRAS, 433, 3227
Katsova, M. M., Kitchatinov, L. L., Livshits, M. A., et al. 2018, ARep, 62, 72
Koch, D. G., Borucki, W. J., Basri, G., et al. 2010, ApJL, 713, L79
Kowalski, A. F., & Allred, J. C. 2018, ApJ, 852, 61
Kowalski, A. F., Hawley, S. L., Holtzman, J. A., Wisniewski, J. P., & Hilton, E. J. 2010, ApJL, 714, L98
Kurucz, R. L. 1993, Kurucz CD-ROM No. 13, Atlas 9 Stellar Atmosphere Programs and 2km/s Grid (Cambridge, MA: Harvard-Smithsonian Center for Astrophysics), http://kurucz.harvard.edu/programs.html
Leitzinger, M., Odert, P., Greimel, R., et al. 2014, MNRAS, 443, 898
Lingam, M., & Loeb, A. 2017, ApJ, 848, 41
Linsky, J. L., Hunten, D. M., Sowell, R., Glackin, D. L., & Kelch, W. L. 1979a, ApJS, 41, 481
Linsky, J. L., Worden, S. P., McClintock, W., & Robertson, R. M. 1979b, ApJS, 41, 47
Lockwood, G. W., Skiff, B. A., Henry, G. W., et al. 2007, ApJS, 171, 260
Maehara, H., Notsu, Y., Notsu, S., et al. 2017, PASJ, 69, 41
Maehara, H., Shibayama, T., Notsu, S., et al. 2012, Natur, 485, 478
Maehara, H., Shibayama, T., Notsu, Y., et al. 2015, EP&S, 67, 59
Mamajek, E. E., & Hillenbrand, L. A. 2008, ApJ, 687, 1264

Marigo, P., Girardi, L., Bressan, A., et al. 2017, ApJ, 835, 77
Mathur, S., Huber, D., Batalha, N. M., et al. 2017, ApJS, 229, 30
McLaughlin, J. A., Nakariakov, V. M., Dominique, M., Jelínek, P., & Takasao, S. 2018, SSRv, 214, 45
McQuillan, A., Mazeh, T., & Aigrain, S. 2014, ApJS, 211, 24
Metcalfe, T. S., & Egeland, R. 2018, ApJ, 871, 39
Mittag, M., Schmitt, J. H. M. M., & Schröder, K.-P. 2013, A&A, 549, A117
Miyake, F., Masuda, K., & Nakamura, T. 2013, NatCo, 4, 1748
Miyake, F., Nagaya, K., Masuda, K., & Nakamura, T. 2012, Natur, 486, 240
Morris, B. M., Curtis, J. L., Douglas, S. T., et al. 2018, AJ, 156, 203
Morris, B. M., Hawley, S. L., Hebb, L., et al. 2017, ApJ, 848, 58
Moschou, S.-P., Drake, J. J., Cohen, O., Alvarado-Gomez, J. D., & Garraffo, C. 2017, ApJ, 850, 191
Namekata, K., Maehara, H, Notsu, Y., et al. 2019, ApJ, 871, 187
Namekata, K., Sakaue, T., Watanabe, K., et al. 2017, ApJ, 851, 91
Neupert, W. M. 1968, ApJL, 153, L59
Nogami, D., Notsu, Y., Honda, S., et al. 2014, PASJ, 66, L4
Notsu, S., Honda, S., Notsu, Y., et al. 2013a, PASJ, 65, 112
Notsu, Y., Honda, S., Maehara, H., et al. 2015a, PASJ, 67, 32
Notsu, Y., Honda, S., Maehara, H., et al. 2015b, PASJ, 67, 33
Notsu, Y., Honda, S., Maehara, H., et al. 2017, PASJ, 69, 12
Notsu, Y., Shibayama, T., Maehara, H., et al. 2013b, ApJ, 771, 127
Noyes, R. W., Hartmann, L. W., Baliunas, S. L., Duncan, D. K., & Vaughan, A. H. 1984, ApJ, 279, 763
Osten, R. A., Kowalski, A., Drake, S. A., et al. 2016, ApJ, 832, 174
Osten, R. A., & Wolk, S. J. 2015, ApJ, 809, 79
Paudel, R. R., Gizis, J. E., Mullan, D. J., et al. 2018, ApJ, 861, 76
Perryman, M. A. C., Brown, A. G. A., Lebreton, Y., et al. 1998, A&A, 331, 81
Pinsonneault, M. H., An, D., Molenda-Żakowicz, J., et al. 2012, ApJS, 199, 30
Pugh, C. E., Armstrong, D. J., Nakariakov, V. M., & Broomhall, A.-M. 2016, MNRAS, 459, 3659
Pye, J. P., Rosen, S., Fyfe, D., & Schröder, A. C. 2015, A&A, 581, A28
Ramsay, G., & Doyle, J. G. 2015, MNRAS, 449, 3015
Rauer, H., Catala, C., Aerts, C., et al. 2014, ExA, 38, 249
Reid, I. N., & Hawley, S. L. 2005, New Light on Dark Stars: Red Dwarfs, Low-Mass Stars, Brown Stars (Chichester: Praxis Publishing)
Rich, E. A., Wisniewski, J. P., McElwain, M. W., et al. 2017, MNRAS, 472, 1736
Ricker, G. R., Winn, J. N., Vanderspek, R., et al. 2015, JATIS, 1, 014003
Riley, P., Baker, D., Liu, Y. D., et al. 2018, SSRv, 214, 21
Roettenbacher, R. M., & Vida, K. 2018, ApJ, 868, 3
Royal Academy of Engineering 2013, Extreme Space Weather: Impacts on Engineered Systems and Infrastructure (London: Royal Academy of Engineering), https://www.raeng.org.uk/publications/reports/space-weather-full-report
Sammis, I., Tang, F., & Zirin, H. 2000, ApJ, 540, 583
Schaefer, B. E., King, J. R., & Deliyannis, C. P. 2000, ApJ, 529, 1026

Schmieder, B. 2018, JASTP, 180, 46
Schrijver, C. J. 1987, A&A, 172, 111
Schrijver, C. J. 2015, SpWea, 13, 524
Schrijver, C. J., Beer, J., Baltensperger, U., et al. 2012, JGRA, 117, A08103
Schrijver, C. J., Cote, J., Zwaan, C., & Saar, S. H. 1989, ApJ, 337, 964
Segura, A., Walkowicz, L. M., Meadows, V., Kasting, J., & Hawley, S. 2010, AsBio, 10, 751
Shibata, K., Isobe, H., Hillier, A., et al. 2013, PASJ, 65, 49
Shibata, K., & Magara, T. 2011, LRSP, 8, 6
Shibayama, T., Maehara, H., Notsu, S., et al. 2013, ApJS, 209, 5
Shimizu, T. 1995, PASJ, 47, 251
Skumanich, A. 1972, ApJ, 171, 565
Soderblom, D. R., Stauffer, J. R., MacGregor, K. B., & Jones, B. F. 1993, ApJ, 409, 624
Takahashi, T., Mizuno, Y., & Shibata, K. 2016, ApJL, 833, L8
Takeda, Y. 1995, PASJ, 47, 287
Takeda, Y., Honda, S., Kawanomoto, S., Ando, H., & Sakurai, T. 2010, A&A, 515, A93
Takeda, Y., Honda, S., Ohnishi, T., et al. 2013, PASJ, 65, 53
Takeda, Y., & Kawanomoto, S. 2005, PASJ, 57, 45
Takeda, Y., Ohkubo, M., & Sadakane, K. 2002, PASJ, 54, 451
Takeda, Y., Ohkubo, M., Sato, B., Kambe, E., & Sadakane, K. 2005, PASJ, 57, 27
Takeda, Y., Sato, B., & Murata, D. 2008, PASJ, 60, 781
Takeda, Y., Tajitsu, A., Honda, S., et al. 2012, PASJ, 64, 130
Thompson, S. E., Jenkins, J. M., & Caldwell, D. A. 2015, Kepler Data Release 24 Notes, Tech. Rep. KSCI-19064-002, (Moffett Field, CA: NASA Ames Research Center)
Toriumi, S., Schrijver, C. J., Harra, L. K., Hudson, H., & Nagashima, K. 2017, ApJ, 834, 56
Tsurutani, B. T., & Lakhina, G. S. 2014, GeoRL, 41, 287
Tu, L., Johnstone, C. P., Güdel, M., & Lammer, H. 2015, A&A, 577, L3
Usoskin, I. G. 2017, LRSP, 14, 3
Valenti, J. A., & Fischer, D. A. 2005, ApJS, 159, 141
Van Doorsselaere, T., Shariati, H., & Debosscher, J. 2017, ApJS, 232, 26
van Saders, J. L., Ceillier, T., Metcalfe, T. S., et al. 2016, Natur, 529, 181
Vaughan, A. H., Preston, G. W., & Wilson, O. C. 1978, PASP, 90, 267
Vida, K., Kriskovics, L., Oláh, K., et al. 2016, A&A, 590, A11
Walkowicz, L. M., Basri, G., Batalha, N., et al. 2011, AJ, 141, 50
Wang, S.-i., Hildebrand, R. H., Hobbs, L. M., et al. 2003, Proc. SPIE, 4841, 1145
Wichmann, R., Fuhrmeister, B., Wolter, U., & Nagel, E. 2014, A&A, 567, A36
Wilson, O. C. 1978, ApJ, 226, 379
Wright, N. J., Drake, J. J., Mamajek, E. E., & Henry, G. W. 2011, ApJ, 743, 48
Wu, C.-J., Ip, W.-H., & Huang, L.-C. 2015, ApJ, 798, 92
Yang, H., Liu, J., Gao, Q., et al. 2017, ApJ, 849, 36
Ziegler, C., Law, N. M., Baranec, C., et al. 2018, AJ, 155, 161